2016•2017
FACULTEIT INDUSTRIËLE INGENIEURSWETENSCHAPPEN
master in de industriële wetenschappen:
verpakkingstechnologie

Masterproef

Optimisation and characterisation of nano-hydroxyapatite/polylactide composites using Fused Deposition Modelling technology

Promotor :
Prof. dr. ir. Mieke BUNTINX

Promotor :
Prof. ISABELLE VROMAN

Copromotor :
PhD. GEOFFREY GINOUX

Gezamenlijke opleiding Universiteit Hasselt en KU Leuven

Erwin Oris

Scriptie ingediend tot het behalen van de graad van master in de industriële wetenschappen: verpakkingstechnologie

2016•2017

Faculteit Industriële ingenieurswetenschappen

master in de industriële wetenschappen: verpakkingstechnologie

Masterproef

Optimisation and characterisation of nano-hydroxyapatite/ polylactide composites using Fused Deposition Modelling technology

Promotor :
Prof. dr. ir. Mieke BUNTINX

Promotor :
Prof. ISABELLE VROMAN

Copromotor :
PhD. GEOFFREY GINOUX

Erwin Oris

Scriptie ingediend tot het behalen van de graad van master in de industriële wetenschappen: verpakkingstechnologie

universiteit hasselt | KU LEUVEN

Acknowledgements

I would like to thank Prof. dr. ir. Mieke Buntinx, Prof. Isabelle Vroman and Mr. Geoffrey Ginoux for their work as supervisors and their continued support throughout this thesis. Without their guidance, the completion of this thesis would have been much harder.

Additionally, I would also like to thank the people of ESIReims, in particular Prof. Damien Erre, Mr. Philippe Dony and Ms. Nathalie Choiselle, for their guidance throughout this thesis and their aid during the sample preparation and sample analysis. Of course, I would also like to thank the people of the IFTS for their help and guidance, especially Dr. Sébastien Alix and Ms. Laurine Renaux. I cannot forget the people of VerpakkingsCentrum IMO-IMOMEC, especially ing. Dimitri Adons, without their swift work and quick responses to my questions, this thesis would not have been possible. I would also like to thank the University of Haute-Alsace for the TEM analysis they executed for this thesis. I would like to thank Catherine Lacoste and the people of the international office of the University of Reims Champagne-Ardenne for helping me integrate with local and Erasmus students.

I would like to thank my friends and family for their support throughout this thesis.

Finally, I would like to thank the Erasmus+ programme of the European Union for allowing me to participate in the Erasmus exchange programme. Thanks to this programme I was able to conduct my thesis abroad while experiencing a new culture. *"The European Commission support for the production of this publication does not constitute an endorsement of the contents which reflects the views only of the authors, and the Commission cannot be held responsible for any use which may be made of the information contained therein."* This thesis was also part of «PolyFabAdd». *«PolyFabAdd» is co-funded by the European Union. Europe invests in Champagne-Ardenne with the European Regional Development Fund.*

Co-funded by the
Erasmus+ Programme
of the European Union

Laboratoire d'Ingénierie
et Sciences des Matériaux

UNIVERSITÉ
DE REIMS
CHAMPAGNE-ARDENNE

Table of Contents

List of tables

Table of figures

Nomenclature

3DP = Three Dimensional Printing

ABS = Acrylonitrile Butadiene Styrene

AM = Additive Manufacturing

ANOVA = Analysis of Variance

BTE = Bone Tissue Engineering

c = concentration

CAD = Computer Aided Design

CTAB = Cetyltrimethylammonium Bromide

CW = Contour Width

D = Diffusion

DMA = Dynamic mechanical analysis

DSC = Differential Scanning Calorimetry

ERDF = European Regional Development Fund

FDM = Fused Deposition Modelling

FFF = Fused Filament Fabrication

FTIR = Fourrier Transformed Infrared spectroscopy

G' = Storage modulus

G" = Loss modulus

HA = Hydroxyapatite

IFTS = Institute of Higher Technical Training

J = the permeation flux

LA = Lactic Acid

LISM = Laboratory of Engineering and Materials Science

nHA = nanohydroxyapatite

NPs = Nanoparticles

OCP = Octacalcium Phosphate

OTR = Oxygen Transmission Rate

P = Permeation

p = pressure

PC = Polycarbonate

PCL = Polycaprolactone

PDLLA = Poly-DL-Lactide

PE = Polyethene

PET = Polyethylene Terephthalate

PGA = Polyglycolide

PLA = polylactide / polylactic acid

PLGA = poly(lactide-co-glycolide)

PLLA = Poly-LL-Lactide

PP = Polypropylene

PP = Polypropylene

PPSU = polyphenylenesulfone

PS = Polystyrene

PVC = Polyvinyl chloride

R&D = Research and Development

R^2 = Coefficient of Determination

RA = Raster Angle

RH = the relative humidity

RRAG = Raster to Raster Air Gap

RW = Raster Width

S = Solubility

SCENHIR = European Commission Scientific Committee on Emerging and Newly Identified Health Risks

SLA = Stereolithography

SLS = Selective Laster Sintering

SSE = Single-screw Extruder

T = Temperature

T_c = Crystallisation Temperature

T_{cc} = Cold Crystallisation temperature

TCP = Tricalcium Phosphate

TetTCP = Tetracalcium Phosphate

T_g = Glass transition Temperature

TGA = Thermogravimetric Analysis

T_m = Melting temperature

TSE = Twin-screw Extruder

WAXD-P = Wide Angle X-ray Diffraction on Powder

WVTR = Water Vapour Transmission Rate

X_c = the crystallinity

$\Delta H°_m$ = Theoretical melt enthalpy for enantiopure PLA with 100% crystallinity

ΔH_m = Melt enthalpy

η = the viscosity

η_0 = the viscosity at zero shear

τ = the mean particle size of the crystal

Abstract

In this study, polylactide/nanohydroxyapatite (PLA/nHA) composites were produced for fused deposition modelling (FDM), which is an additive manufacturing technology commonly used for prototyping and production applications. First, PLA/nHA composites (0.5%, 1%, 3%, 5 wt.%) were compounded using a twin-screw extruder, subsequently, these were shaped into filaments with a single-screw extruder. Thirdly, specimens for dynamic mechanical analysis (DMA) and tensile testing were FDM printed. Doehlert response surface methodology was applied to optimise the tensile properties of each formulation. A comparison of the mechanical properties of the printed tensile test specimens with injection moulded specimens showed a lower Young's modulus and ultimate strength and a higher storage modulus for the printed samples. Additionally, the same ultimate strength decreased with higher HA content. HA induced nucleation of PLA, but also a reduction of the degradation temperature, as shown by differential scanning calorimetry and thermogravimetric analysis respectively. Oscillatory rheological analysis showed the presence of a Newtonian plateau, followed by a shear thinning behaviour. The first HA addition resulted in a thickening effect, decreasing upon addition of HA, up to a thinning effect at 5 wt.%. In conclusion, this study proves successful printing of PLA/nHA nanocomposites using FDM, which might be promising e.g. for bone tissue engineering.

Abstract in Dutch

In deze studie werden polylactide/nanohydroxyapatiet (PLA/nHA) composieten geproduceerd voor fused deposition modelling (FDM). Eerst werden PLA/nHA composieten (0.5%, 1%, 3%, 5 wt.%) gemaakt met een twin-screw extruder, deze werden dan omgevormd tot filamenten met een single-screw extruder. Ten slotte werden de filamenten omgevormd tot dynamische mechanische analyse (DMA) en trekproefmonsters via een FDM proces. Doehlert response surface methodologie werd gebruikt om de trekeigenschappen te optimaliseren voor elk composiet. Een vergelijking van de mechanische eigenschappen van de geprinte trekproefstukken met de gespuitgiete monsters gaf aan dat de Young modulus en treksterkte hoger waren en de storage modulus lager was voor de geprinte proefstukken. Bovendien daalde de treksterkte met toenemende HA inhoud. Uit de differentiële scanning calorimetrie en de thermogravimetrische analyse volgde dat HA een nucleatie veroorzaakte in PLA en een daling van de degradatietemperatuur te weeg bracht. Oscillerende rheologische analyse toonde de aanwezigheid van een Newtonisch plateau, gevolgd door shearthinning. De eerste toevoeging van HA resulteerde in een verdikkingseffect, waarna bijkomende HA-inhoud resulteerde in een daling van het verdikkingseffect en zelfs een verdunningseffect bij toevoeging van 5 wt.% HA. In conclusie, PLA/nHA nanocomposieten werden succesvol geprint met FDM in deze studie, dit kan veelbelovend zijn voor bv. bone tissue engineering.

1 Introduction

This thesis was conducted within the innovative materials branch of the Laboratory of Engineering and Materials Science (LISM) at Reims, French research group EA 4695. “The LISM was established in January 2012 and gathers researchers who focus on developing, formatting and analysing materials and their properties” [1]. The LISM has multiple sites, but this thesis was executed on the sites of the Engineering school of Reims (ESIReims) and the Institute of Higher Technical Training (IFTS) at Charleville-Mézières, both situated in France.

The thesis is a part of the PhD study of Mr. Geoffrey Ginoux, which is funded by the European Regional Development Fund (ERDF). The topic of the PhD is PolyFabAdd (Charged Polymers in Additive Manufacturing). PolyFabAdd focuses on the utilisation of charged polymers within additive manufacturing (AM) processes. The scientific and technological objectives of the PhD project are (i) a better understanding of the relationship between the rheological behaviour of polymer systems and their ability to shaping by additive manufacturing technologies (FDM® in particular), (ii) the development of polymer-based formulations from biological resources adapted to these technologies and providing multi-functionality [2]. Examples of this multi-functionality are the use of nanostructured polylactic acid (PLA) materials for packaging and tissue engineering as discussed by [3].

Additive manufacturing consists of multiple technologies, one of these technologies is Fused Deposition Modelling® (FDM®) [4] [5]. Fused deposition modelling®, often wrongly referred to as three-dimensional printing, is traditionally used for rapid prototyping. The main reasons behind this trend are the short time between the design phase and the building phase, the fast build time and the cheap printing materials. However, despite its rise in popularity, full scale application of the technology has not gained much emphasis. This due to a lack of compatibility of available materials [6]. Sood et al. identify two approaches to overcome this limitation: The development of new materials with superior characteristics than conventional materials and the adjustment of the process parameters during the fabrication stage to improve properties [6].

1.1 Research question

In FDM processes, neither the materials nor the process have been studied in a systematic manner towards functional components production, with adjusted mechanical properties, or with the objective of getting competitive production time/cost (for small/medium production series), respectively [7]. This results in a lack of accuracy when creating small series with FDM, an effect of the lack of accuracy is sample porosity, which lowers the mechanical properties of the samples. Due to the poorly characterised impact of process parameters on the sample quality and the low amount of available printing materials (Mainly Acrylonitrile butadiene styrene (ABS), Polycaprolactone (PCL), PLA and Polypropylene (PP)), the expansion of the technique is limited [7] [8] [9] [10] [11].

The lack of standardisation in articles, when characterising different materials for FDM, makes it hard to compare different test results with each other. In recent years, there has been an improvement with regards to the characterisation as more mathematical approaches are being used, yet most

studies do not consider the printing speed and printing temperature as important parameters [12] [13] [14] [15].

By researching charged polymers, new potential materials and charges can be proposed for the FDM printing process. Thus, leading to the expansion of the available materials for FDM and AM in general. With the addition of the charges and their specific properties, the potential applications of FDM in the future can increase. Nano charges are preferred over micro charges, since they do not cause clogging of the FDM printing nozzle [16]. One should keep in mind that materials react differently on changing process parameters. In this thesis, the properties of PLA and PLA charged with hydroxyapatite, chosen for its application in bone tissue engineering (BTE), are determined throughout the production chain "From formulation to finished parts" and for varying FDM printing parameters [17] [18] [19] [20] [21]. With the characterisation of PLA/nHA, the amount of available materials can potentially go up as polymers charged with nanoparticles can be considered for the FDM printing process.

PLA is a biodegradable polymer created from bio resources [22]. Its biodegradability in combination with its bio origin, has led to an increased industrial interest in recent years. However, a decrease of the permeability of PLA can increase its use for packaging applications [23]. The addition of hydroxyapatite to the PLA matrix might increase its crystallinity fraction, which in turn could lead to a reduced permeability [13] [24]. PLA can also be used in FDM for the creation of small series of packaging.

1.2 Objectives

As mentioned above, there is a limited number of available materials and a lack of knowledge with regards to the effect of process parameters on the properties of FDM printed workpieces. A better understanding can be achieved by tracking the properties throughout the production chain. Following Carneiro et al., the printed test samples will be compared with injection moulded test samples made from the same pellets. Additionally, the relation between different process steps and the properties of the tested materials was determined. After which the FDM process was optimised, according to the rheological behaviour. Special attention should be given to the filaments, a homogenic filament results in more easily controlled process parameters and thus improved properties [7].

In summary, this thesis aims at achieving the following objectives:

(i) Formulate nano-charged materials of PLA/nHA;
(ii) Apply these materials in FDM and injection moulding;
(iii) Characterise the materials;
(iv) Compare the impact of the FDM process and the injection moulding on the mechanical behaviour of the tensile test specimens;
(v) Determine the dispersion state of the nano-charges in the polymer matrix;
(vi) Create PLA/nHA films from the charged pellets;
(vii) Test the permeability of the PLA/nHA films.

2 Literature study

2.1 Polylactic acid

Polylactic acid (PLA) is a biodegradable polymer [25] [26]. Some of the biggest producers of PLA in the world are NatureWorks® LLC (Oyobo), Dai Nippon Printing Co., Mitsui Chemicals, Shimadzu, NEC, Toyota (Japan), PURAC Biomaterials, Hycail (The Netherlands), Galactic (Belgium), Cereplast (U.S.A.), FkuR, Biomer, Stanelco, Inventa-Fischer (Germany), and Snamprogetti (China) [27] [28] [29]. While the cost of some biodegradable polymers is high compared with conventional polymers, PLA has a relatively low production cost [28]. PLA has the following processing possibilities: Injection moulding, extrusion, cast film extrusion, blow moulding, fibre spinning and thermoforming [29]. Thermoforming of trays and containers for food packaging and foodservice applications is the main market application of PLA [28]. The usage of PLA in other areas such as films and labels, injection stretch blow moulded bottles and jars, specialty cards and fibres is being developed [28].

2.1.1 Lactic acid

Lactic acid (2-hydroxy propanoic acid), produced via fermentation or chemical synthesis, is the single monomer of PLA [29] [30] [31]. LA synthesis can result in the L or the D stereoisomer or a racemic mixture depending on the used synthesis route [30] [31]. The synthesis via fermentation, the chemical breakdown of a substance by bacteria, yeasts, or other microorganisms, of a renewable agricultural source corn can result in the L or D stereoisomers depending on the microorganisms used. *Lactobacilli amylophilus*, *Lactobacilli bavaricus*, *Lactobacilli casei*, *Lactobacilli maltaromicus*, *and Lactobacilli salivarius* predominantly yield the L isomer, while strains such as *Lactobacilli delbrueckii*, *Lactobacilli jensenii*, or *Lactobacilliacidophilus* yield the d-isomer or mixtures of both [31]. Chemical synthesis results in a racemic mixture of D- and L-lactic acid [30] [31]. Fermentation is advantageous compared to chemical synthesis, as it allows the production of optically pure L- or D-lactic acid, has a low substrate cost, a low production temperature and a low energy consumption [31].

2.1.2 Polylactic acid synthesis

The synthesis of PLA consists of the polymerisation of LA. There are three polymerisation routes: Direct condensation polymerisation; direct poly-condensation in an azeotropic solution; and ring opening polymerisation after lactide formation [29] [32]. Figure 1Figure 1 shows the different steps in the polymerisation process for each technique. For direct condensation polymerisation, chain coupling agents and adjuvants are needed to obtain a solvent-free high molecular weight PLA [32]. The removal of the solvent; and the chain coupling agents result in additional costs and complexity [32]. Azeotropic dehydrative condensation eliminates the need for chain extenders and adjuvants, by reducing the distillation pressure and increasing the temperature [32]. Although azeotropic poly-condensation leads directly to high molecular weight polylactic acid, it is not the most used technique. Ring opening polymerisation is the most common way to obtain high molecular weight polylactic acid [30] [31] [32].

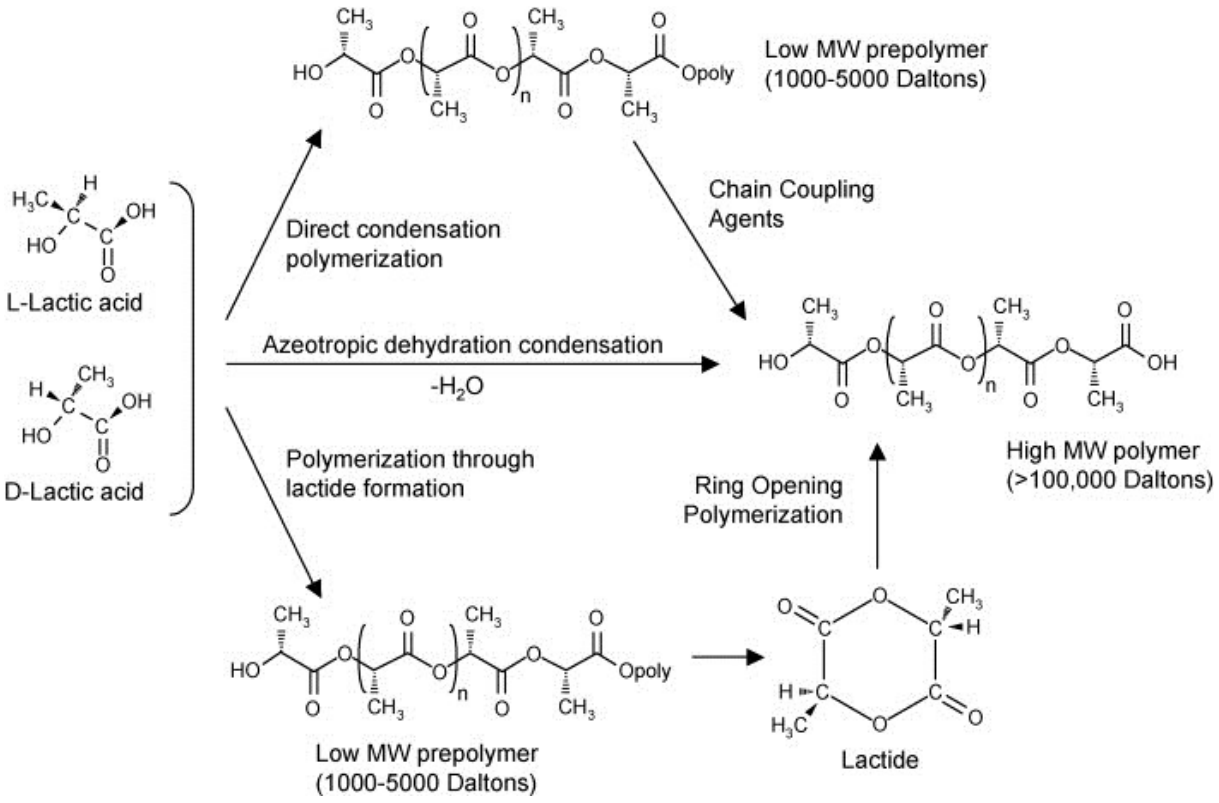

Figure 1 Synthesis of PLA from l- and d-lactic acids [33].

Before ring opening polymerisation can take place, a cyclic lactide dimer has to be formed [31]. Lactides are formed in two steps. The first step consists of evaporating the condensation product, water, during the oligomerisation of the L-lactic acid, D-lactic acid or a mixture of both stereoisomers [30] [31] [34]. The resulting low molecular weight polylactic acid oligomers are then catalytically depolymerised through internal transesterification, by 'back-biting' reaction to lactide during the second step [30] [31] [34]. There are three possible stereoforms of the resulting lactide as shown in figure 2: L-lactide, D-lactide and meso-lactide [30] [31]. Once the lactides are purified, the lactide monomers can be converted into high molecular weight polyesters by catalytic ring-opening polymerisation [30] [31] [34]. The use of costly and environmentally unfriendly solvents can be eliminated by using an organo-tin-catalyst during the ring opening polymerisation of the lactide in the melt [30]. Additionally, residual lactide monomer can be removed and recycled within the process [30]. Madhavan et al. indicate that alcohol and carboxylic acid can influence the production rate of PLA, while alcohol increases the PLA production, it also decreases the molecular weight [31]. Carboxylic acid on the other hand, decreases the PLA production but has no effect on the molecular weight [31]. An important factor during the production of PLA, is the usage of specific lactide stereoforms. The degree of crystallinity and hence many important properties is controlled by the ratio of D to L enantiomers, this ratio can be changed by using stereospecific catalysts [31]. The polymerisation of a racemic mixture of L- and D- lactides usually leads to the synthesis of poly-DL-lactide (PDLLA), which is amorphous [31]. Murariu et al. mention the difference in susceptibility between the different lactides, the meso-lactide is said to be up to two times more susceptible to ROP reactions than the other lactides [30]. A higher susceptibility to polymerisation can result in a reduced catalyst usage, lower processing temperatures, or both [30].

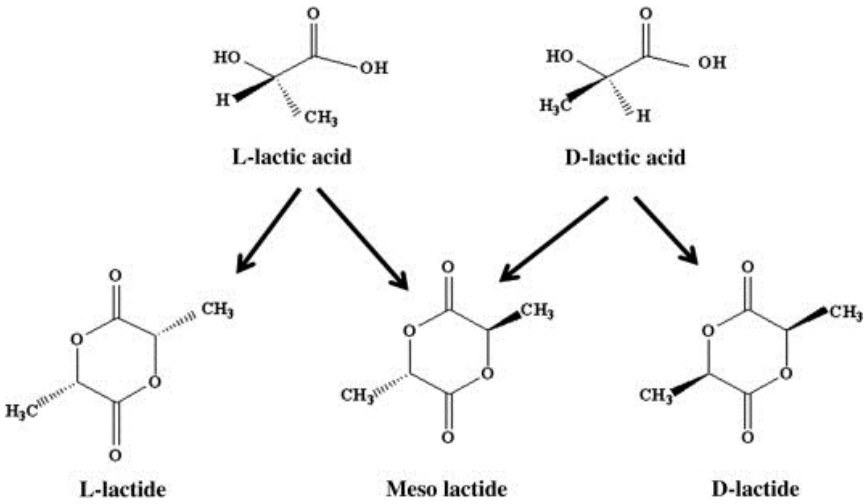

Figure 2 Stereoforms of lactides [31].

2.1.3 Properties

2.1.3.1 Crystallinity & thermal, mechanical and rheological properties

As mentioned above, the stereoforms of the lactides used for the PLA production influence the resulting PLA properties. Besides the stereochemistry, the processing temperature, the annealing time and the molar mass also affect the properties of PLA [35] [36]. The crystallinity of a polymer, which is an indication of the amount of crystalline region in the polymer with respect to the amorphous region, is directly influenced by the stereochemistry, molar mass and the thermal history [29] [35] [36] [37]. Additionally, the crystallinity influences the hardness, modulus, tensile strength, stiffness, crease and melting points of polymers [29] [36].

There are three different PLA crystals, depending on the structural positions in which the crystals grow: α, β and γ [36] [38]. Each of the crystals is characterised by different helix conformations and cell symmetries, which are the result of different thermal and/or mechanical treatments [36] [38]. The α form grows upon melt or cold crystallisation, and from solution-spinning processes at low drawing temperatures and/or low hot-draw ratios [36] [38]. When the α form undergoes mechanical stretching, the β form is formed [36] [38]. Additionally, the β form can also be formed from solution-spinning processes conducted at high temperatures and/or high hot-draw ratios [38] [39]. The last form, the γ form, has been reported to develop on hexamethylbenzene substrates by epitaxial crystallisation at a crystallisation temperature (T_c) around 140°C [38] [40]. The α form is more stable and has a melting temperature (T_m) of 185°C compared to the β form, which has a T_m of 175°C [32].

Controlling the resulting crystal structure is very important as the optical purity influences the thermal and mechanical properties. One proposed way of controlling the crystallinity, is the use of special catalysts that control the ratio and sequence of the D- and L-lactic acid units in the final polymer [36] [41]. Fully amorphous materials can be made by the inclusion of a relatively high D content (>20%), whereas highly crystalline material is obtained when the D content is low (<2%) [41] [42] [43] [44]. Alternatively, a highly crystalline material can also be obtained by introducing a low amount of L-lactic acid units in D-lactic acid. The crystallinity can also be promoted with nucleating agents in certain processes such as injection moulding with relatively short moulding cycles [32]. PLA has a rather slow

crystallisation rate when compared to many other thermoplastics [30]. Anderson et al. show that the crystallisation rate can be increased with the addition of 3%wt poly(D-lactic acid) (PDLA), this resulted in faster crystallisation rates than common nucleating agents such as talk [45]. The L-lactic acid units also influence the T_m and the glass transition temperature (T_g).

Besides the optical purity, the thermal history and the molar mass also influence the T_g and the T_m [37]. T_g and T_m decrease with decreasing poly(L-lactic acid) (PLLA) content [32] [36] [46] [47]. The T_g influences physical characteristics such as density, heat capacity and mechanical and rheological properties of PLA [36]. For amorphous PLA, important changes in polymer chain mobility take place at and above the T_g. Both T_g and T_m are important physical parameters to predict PLA behaviour for semi crystalline PLA [36]. Farah et al. found the most referred value of the estimated melt enthalpy ($\Delta H°_m$) for enantiopure PLA with 100% crystallinity to be 93 J/g [36]. The density depends greatly on the stereoforms of the lactide used, for amorphous PLLA a density of 1.248g/cm³ has been reported and for crystalline PLLA a density of 1.290g/cm³ [33]. While the density of solid polylactide has been reported as 1.36g/cm³ for L-lactide, 1.33g/cm³ for meso-lactide, 1.36g/cm³ for crystalline polylactide and 1.25g/cm³ for amorphous polylactide [33].

In the literature, the thermogravimetric analysis of PLA shows a sigmodal curve with the degradation starting around 300°C and ending before 400°C [48] [49] [50]. Mróz et al. found the highest PLA decomposition rate at 352.3°C for a heating rate of 10 °C/min and under argon atmosphere [50]. The differential scanning calorimetry of PLA results in curves with a T_g, a T_{cc} and a T_m. Ozkoc and Kemaloglu found a T_g of 59.9°C, a T_{cc} of 106.1°C and a Tm of 152.6°C for neat PLA [51]. Additionally, they found a ΔH_m of 19.9 J/g, which corresponded to a calculated crystallinity of 21.4% [51]. The crystallinity was calculated with the enthalpy for enantiopure PLA with 100% crystallinity being the previously reported 93 J/g. Kulinski and Piorkowska determined the T_g from the E" and tangent δ peaks of dynamic mechanical analysis and found E" peaks of 58°C and 60°C for amorphous and semicrystalline PLA respectively; and a tangent δ peak of 65°C for both amorphous and semicrystalline PLA [52]. Ozkoc and Kemaloglu found a maximum strength of 33.58 MPa and a Young's modulus of 1406 MPa for neat PLA after tensile tests [51]. Liu et al. discuss the rheological properties of PLA/HA, they show that the complex viscosity decreases as the angular frequency increases, which they attribute to a pseudoplastic behaviour [53]. The Newtonian plateau of PLA/HA was found at almost 6000 Pa.s, with the HA in nanoform [53].

2.1.3.2 Degradability

PLA is very susceptible to degradation; its stability is vital for many applications. It is thus key to understand the degradation processes and how they can be controlled and/or prevented. Above 200°C PLA undergoes thermal degradation by hydrolysis, lactide reformation, oxidative main chain scission and inter- or intramolecular transesterification reactions [36] [37] [54]. Time, temperature, low molecular weight impurities and catalyst concentration impact the degradation of PLA [36] [54]. The degradation temperature decreases while the degradation rate increases with the addition of catalyst and oligomers, in addition they can also cause viscosity and rheological changes, fuming during processing and poor mechanical properties [54]. Given the above-mentioned T_m of 185°C for α crystals, the processing temperatures of PLA have to be in excess of this temperature. In the literature, the

required processing temperatures are in excess of 185-190°C [36] [54]. Unzipping and chain scission reaction leading to thermal degradation and loss of molecular weight are known to occur at these temperatures [36] [54]. The most common way to prevent degradation is the inclusion of lactide enantiomers with the opposite configuration, this results in PDLLA and a significant decrease in crystallinity and crystallisation rates [36] [54]. Carrasco et al. found that injection and extrusion processes resulted in a lower viscosity, which was linked to a decrease in molecular weight due to degradation [48]. They also found that thermal decomposition occurred within the temperature range of 325-375°C for processed material, while raw material had a slightly higher thermal stability [48]. Farah et al. mention a molecular weight reduction ranging from 21.85% to 41.00% when PDLLA was injection moulded and extruded respectively [36]. Thermal degradation was found to be due to chain splitting and not hydrolysis [36] [55].

Although the thermal degradation of PLA starts at temperatures lower than the T_m, the degradation rate can be limited by reducing the time at which PLA is held at temperatures above its T_m since the degradation rate rapidly increases above T_m [29] [36]. Additionally, the degradation rate can also be limited by reducing the moisture content [29] [56] [57]. Other factors that influence the degradation rate are: particle size and shape of the polymer; crystallinity, % D-isomer, residual lactic acid concentration, molecular weight distribution, water diffusion, and metal impurities from the catalyst [29]. Hyon et al. found that residual monomer enhanced hydrolytic degradation of the polymer, this due to the creation of a porous structure which enhances water diffusion [58]. They also studied the impact of the molecular weight and found that a higher molecular weight resulted in a longer retention of the initial properties such as molecular weight and tensile strength [58]. Crystallinity and % D-isomer both play a role in preventing hydrolytic degradation. Amorphous material allows for easier hydrolytic degradation, while crystalline material hinders water diffusion. Mathematical models have been proposed to describe the molecular weight changes caused by degradation [59].

2.1.3.3 Biodegradability

Bio-based polymers are derived in whole or in part of biological products issued from the biomass [60]. Despite their name, bio-based polymers are not always environmentally friendly, biocompatible or biodegradable, a lot depends on the polymer structure [60]. Environmentally friendly or eco-compatible polymers have a minimal deleterious impact on the environment, as determined by a life cycle assessment [60]. Eco-compatibility complements biocompatibility, which indicates that a polymer will not produce an adverse effect when put into contact with a living system [60]. Biodegradable polymers have macromolecules that are susceptible to degradation by biological activity, resulting in a molar mass reduction [60]. Table 1 classifies polymers into four categories based on their biodegradability and raw materials, as proposed by Iwata et al. [25]. Not all bio-based polymers are biodegradable while some fossil based polymers are biodegradable.

Table 1 Classification of plastics [25].

	Bio-based plastics (renewable resources)	Oil-based plastics (fossil resources)
Biodegradable plastics	poly(lactic acid) (PLA) polyhydroxyalkanoate (PHA) polysaccharide derivatives (low DS)[a] poly(amino acid)	poly(ε-caprolactone) (PCL) poly(butylene succinate/adipate) (PBS/A) poly(butylene adipate-co-terephthalate) (PBA/T)
Non-biodegradable plastics	polysaccharide derivatives (high DS)[a] polyol–polyurethane bio-polyethylene (bio-PE) bio-poly(ethylene terephthalate) (bio-PET)	polyethylene (PE) polypropylene (PP) polystyrene (PS) poly(ethylene terephthalate) (PET) poly(ethylene terephthalate) (PET)

[a] DS=degree of substitution.

Biodegradation is a degradation catalysed by microorganisms, ultimately leading to the formation of carbon dioxide, water and new biomass [61]. The degree of biodegradation and the impact of the polymer bioproducts are important when defining biodegradability [61] [62]. For the complete biodegradation or mineralisation, the original product is completely converted into gaseous products and salts by bacteria, fungi, yeasts and their enzymes [61] [63]. There are four environments in which biodegradation occurs: Aerobic aquatic, aerobic solid, anaerobic aquatic, and anaerobic solid environments [61]. Equations (1) and (2) show which chemical process occurs based on the presence of oxygen.

$$C_{polymer} + O_2 \rightarrow CO_2 + H_2O + C_{residu} + C_{Biomass} + salts \quad (1)\ [61]$$

$$C_{polymer} \rightarrow CO_2 + CH_4 + H_2O + C_{residu} + C_{Biomass} + salts \quad (2)\ [61]$$

Grima et al. identify two stages in complete biodegradation: the depolymerisation/molecular weight reduction of the plastic, and the mineralisation [61]. The first stage consists of the depolymerisation of the macromolecules into shorter chains. This stage usually takes place outside of the organism due to the size of the polymer chain and the insoluble nature of many polymers and is the result of extra-cellular enzymes and abiotic reactions [64]. Degradation caused by enzymes can be observed in both biotic and abiotic conditions, but only degradation due to cell bioactivity can be called biodegradation [60]. In the next stage, these shorter polymer chains are absorbed and undergo aerobic or anaerobic microbial degradation [61]. Important for biodegradation is the existence of microorganisms capable of producing enzymes that can initiate the depolymerisation process and capable of mineralising the formed oligomers and monomers [61] [63]. Additionally, the environment is also important, the microorganisms need certain environmental conditions and the presence of certain elements to construct the enzymes [61]. Finally, the polymer structure also influences the biodegradation process; the water solubility, the molecular weight distribution, the chemical bonding, the branching, the degree of polymerisation and the crystallinity will influence the availability of the polymer for the microorganisms [61] [63] [64]. The crystallinity is a very important factor, as the amorphous phases are more accessible for the enzymes and thus more easily degraded [63].

Aliphatic polyesters such as PLA are readily degraded by microorganisms present in the environment, this unlike conventional plastics such as polyethene (PE), polypropylene (PP), polystyrene (PS), and polyvincyl chloride (PVC) which are resistant to microbial attacks [29]. In the human body, PLA is initially degraded by hydrolysis and then the soluble oligomers are metabolised by cells [29]. Biodegradation of PLA in the environment under ambient conditions is more difficult since it is largely resistant to attacks of microorganisms in soil or sewage [29] [46] [47]. In addition, PLA degrading microorganisms are not widely distributed in the natural environment, reducing PLA's susceptibility to

microbial attacks [65]. An initial hydrolysis step at elevated temperatures is needed to reduce the molecular weight and facilitate the biodegradation. Kale et al. studied the degradation of PLA bottles in real composting conditions and found that the bottles were completely degraded after 30 days [66]. Microbial and enzymatic degradations are interesting since they do not require high temperatures [29]. Enzymes that have been found to degrade PLA in different scales are proteinase K, alkaline protease, serine proteases, cutinase-like enzyme, lipase and PLLA depolymerase [29] [67] [68] [69]. Biodegradation of PLA follows the previously discussed steps, first there is a molecular weight reduction after which the mineralisation step will take place.

2.1.3.4 Recyclability

There are two methods for PLA recycling, hydrolysis or solvolysis to L-lactic acid or L-lactic acid based compounds and depolymerisation to the cyclic dimer, L-lactide [70] [71]. Both methods have the problem of a low yield of monomers in a short period and require the removal of catalysts and additives for hydrolysis, solvolysis, or depolymerisation [70]. Additionally, crystalline residues, resulting from selective hydrolysis in amorphous regions, will prolong the hydrolysis due to permeability problems and will decrease the yield of L-lactic acid when the hydrolysis period is short [70]. This problem can be overcome by carrying out the hydrolysis at temperatures above the T_m, an additional advantage of the higher temperature is the fact that no catalyst is needed [70]. The recycling of PLA did raise some concerns as PLA and polyethylene terephthalate (PET) are hard to distinguish and the PLA recycle stream is relatively low [29]. Contamination of the PET recycle stream would result in chemical and property differences. However, studies showed the capability of the current equipment to distinguish PET and PLA with an effectiveness of up to 93% [29]. Additionally, new processing techniques are being proposed. Carné et al. propose a stepwise process to both recycle and separate PLA and PET mixed waste [72]. This process, shown in figure 3, takes advantage of the different reactivity to alcoholysis of the two plastics, resulting in a selective depolymerisation process [72].

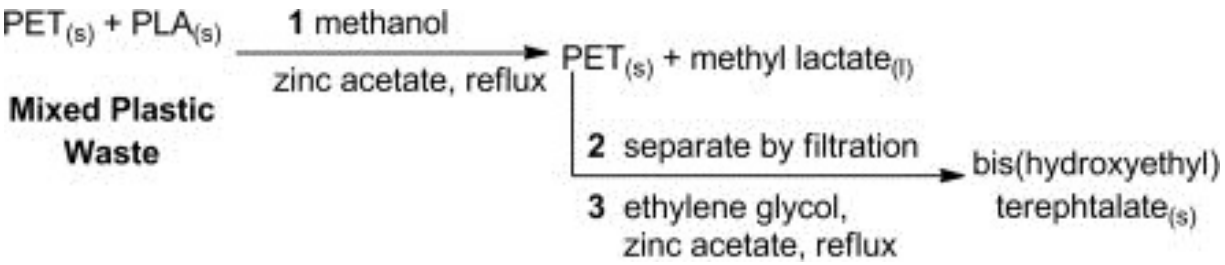

Figure 3 Stepwise process to both recycle and separate PLA and PET mixed waste [72].

2.2 Hydroxyapatite

Apatites (biominerals) are calcium phosphates with generic formula $Ca_5(PO_4)_3(F, Cl, OH)$, they are characterised by phosphorus tetrahedrons which share oxygen with nine-coordinated calcium sites and singly charged anion lattice sites hosting F, Cl or OH that are surrounded by a planar arrangement of three calcium atoms, as shown in figure 4 [73]. Based on the present anion, the apatites can be divided into chlorapatite (chlorine-rich variety); Dahllite (carbonate-bearing hydroxyapatite); fluorapatite (fluorine-rich variety); francolite (carbonate-rich variety); and hydroxyapatite (hydroxyl-rich variety) [73]. Calcium phosphates are major components of natural bone and have bioactive and

biocompatible properties [74]. Hydroxyapatite ($Ca_{10}(PO_4)_6(OH)_2$, HA), dicalcium phosphate dihydrate (CaHPO4·2H2O, DCPD), tricalcium phosphate (Ca3(PO4)2, TCP), tetracalcium phosphate (Ca4P2O9, TetTCP) and octacalcium phosphate (Ca8H2(PO4)6, OCP) are all calcium phosphates that have been studied for application in medical fields [74].

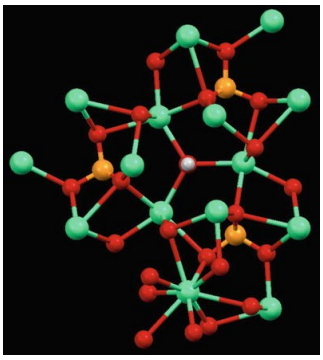

Figure 4 Apatite structure viewed along the c-crystallographic axis: green = calcium, red = oxygen, orange = phosphorus, white = fluorine, chlorine, or hydroxyl [73].

HA is, at 65 wt%, a major bone component, providing most of the stiffness and strength of the bone [75] [76]. Additionally, the morphology and dimensions of HA crystals in bone affects its mechanical properties [75]. Su et al. found that HA crystals in the body can be nano-sized, with the average sizes of mature human bone crystals being ~50 nm in length and ~25 nm in width [77]. Maas et al. found that the HA powders used for ceramics consist of characteristic needle-like HA nanocrystals with a length varying from 25-50 nm and a diameter around 5 nm [78]. Figure 5 shows the transmission electron micrograph of a typical HA nanopowder. Montjovent et al. found a specific surface of 62.53 m^2/g for nano HA powders [79]. Ramakrishna et al. found a modulus of 95 GPa and a tensile strength of 50 MPa for hydroxyapatite [80]. The theoretical density of HA corresponds to 3.16 g/cm^3, which is much higher than that of human bones (1.89 g/cm^3) [81] [82] [83]. Figueiredo et al. found that calcined samples exhibited skeletal densities near to 3 g/cm^3, which is close to the theoretical density of HA [81].

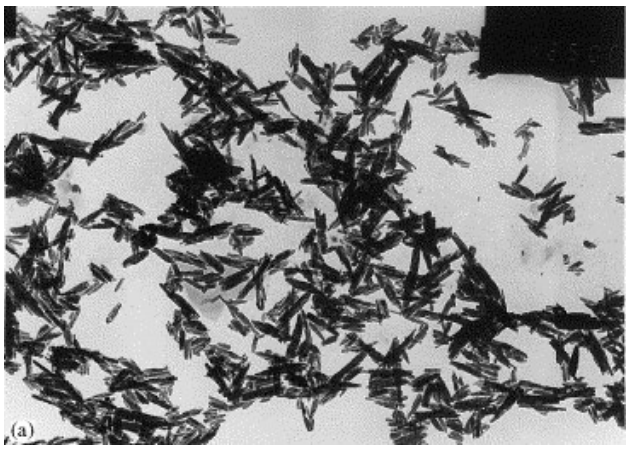

Figure 5 TEM of HA for P120 (original magnification ×23 000) [84].

2.2.1 Nanoparticles

Nanoparticles (NPs) are particles with at least one dimension between 1 and 100 nm [85]. Based on the number of dimensions under 100 nm, NPs can be divided into isodimensional NPs (3 dimensions), nanotubes or nanowhiskers (2 dimensions) and nanosheets (1 dimension) [86]. Due to their small size,

they have unique chemical and physical characteristics, leading to advanced magnetic, electrical, optical, mechanical and structural properties compared to the original bulk substance [85]. This can be linked to their higher surface to volume ratio, potentially increasing interaction when they are incorporated in materials [85]. The surface to volume ratio or specific surface area can vary a lot. Peigny et al. calculated the theoretical specific surface area of carbon nanotubes and found that the specific surface area range over a very broad scale, from 50 to 1315 m^2/g [87]. The use of NPs is not without controversy, as they may pose a risk for humans and the environment [88] [89] [90]. The European Commission Scientific Committee on Emerging and Newly Identified Health Risks (SCENHIR) concluded that there is not yet a generally applicable paradigm for nanomaterial hazard identification, a case by case approach for the risk assessment of nanomaterials is thus warranted [91]. Additionally, the committee also indicated that the methodology for both exposure estimations and hazard identification needs to be further developed, validated and standardised [91].

2.2.2 Synthesis

Multiple techniques exist to create nano HA: a wet chemical precipitation technique, followed by hydrothermal treatment (nanorods); a cationic surfactant method (nanorods); a precipitation with cetyltrimethylammonium bromide (CTAB) as surfactant (Needle-shaped); precipitation with and without utilizing F127 as surfactant (Plate-shaped and spherical respectively) [74] [92] [93] [94] [95] [96] [97]. Swain and Sarkar used a coprecipitation method with multiple starting precursors and reaction media and found that sphere particles were developed in basic medium, and rods in weak acidic medium [92]. Albano et al. obtained HA nanocrystals with a needle shape morphology and average dimensions of 74±21 nm in length and 22±7 nm in width using a precipitation method [98].

2.3 PLA/nHA nanocomposites

Polymer composites are the result of an inclusion of one or more filler materials in the polymer matrix. Usually a composite is created when a chosen polymer lacks mechanical strength or specific properties such as electric conductivity, thermal resistance, etc. Depending on the lacking property, one or more appropriate fillers can then be added to the polymer matrix. Multiple charges can add the same property to a polymer matrix, however, the compatibility, efficiency and cost of the charges will determine the suitable candidate. Additionally, the application can impose requirements on the charges, such is the case for medical applications, for which strict rules exist with regards to the used materials.

The creation of PLA/nHA nanocomposites and the usage of the composites in fused deposition modelling in this study is potentially interesting for bone tissue engineering. HA cannot be used as a bone repair material on its own, given the low mechanical flexural strength and fracture toughness, therefor it is included in a polymer matrix [74] [99]. Multiple polymer matrices have already been used for HA composites, but biodegradable polymers like poly(a-esters) such as poly(hydroxyalkanoates), poly(a-hydroxyacids) and poly(lactones) have attracted much interest due to their good biocompatibility, specific biodegradability, and good mechanical properties [100]. The biodegradability of the polymer matrix is of interest in bone tissue engineering, as it avoids a secondary operation to remove the scaffold and with it comes a reduction of the chance of nosocomial diseases, given that the patient spends less time in the hospital and has to undergo fewer operations. Additionally, PLA,

polyglycolide (PGA) and poly(lactide-co-glycolide) (PLGA) are the poly(a-hydroxyacids) most extensively investigated, due to easy processing and adjustment of mechanical properties and degradation features by copolymerisation [99] [101]. Zhang et al. found that the compressive strength and the young modulus increased monotonously from 53 MPa to 155 MPa and from 1.2 GPa to 3.6 GPa respectively when the HA content increased from 0-20% in PLLA [102]. Nejati et al. show that PLA/HA microcomposites (50 wt% HA) and PLA/HA nanocomposites (50 wt% HA) have significantly higher average elastic moduli and compressive strengths, at 13.68 MPa and 4.61 MPa respectively for the microcomposite and at 14.9 MPa and 8.67 MPa respectively for the nanocomposite, compared to the 1.79 MPa and 2.4 MPa respectively for the pure PLLA [19]. This also shows that the higher specific surface of the nanocomposites results in a more efficient improvement of the mechanical properties when compared to the microcomposites [19]. Nejati et al. also deduced from Fourrier Transformed Infrared spectroscopy (FTIR) analysis that there are some molecular interactions and chemical bonding between both nano and micro HA, and PLA, affecting the interfacial behaviour and mechanical properties of the composites [19]. The lower carbonyl peak of PLA and lower hydrogen peak of micro and nano HA, indicate that the interaction in the composite is in fact a hydrogen interaction [19]. The interaction between the polymer matrix and the filler leads to improved mechanical properties.

Several methods exist to formulate PLA/nHA composites: solvent-casting, injection, gas foaming, co-grinding, additive manufacturing, etc. [79] [103] [104] [105]. Zhang et al. used a modified in situ precipitation method to prepare PLLA/nHA composites [102]. Nejati et al. obtained PLLA/nHA composites by using a thermally induced phase separation method [19]. Peng et al. used electrospinning to incorporate needle shaped nano-sized HA particles into PLLA nanofibers [106]. Bianco et al. also used electrospinning, but they used calcium deficient nHA [107]. Seyedjafari et al. used a similar technique, but they plasma-treated the surface of electrospun PLLA nanofibers, before coating them with nanohydroxyapatite [108]. Aydin et al. [109] grafted HA nanorods on PLLA before mixing grafted PLLA, PLLA and nHA in a chloroform solution; after drying they extruded the obtained chips. Wei and Ma used a phase separation technique to formulate PLLA/nHA composite scaffolds [18]. Liu et al. synthetised PLA/nHA composites with a reactive extrusion [53].

Most methods start with a mixing process in which the PLA and nHA are first mixed using a high speed mixer [110], the stirring of solutions [111] etc. For some of these methods the mixing is also the last step of the method. In others, the mixing is followed by a second step, often an extrusion [110] and in some cases, solvent evaporation [111]. Occasionally there is also a grafting process to increase interactions between the nHA and the polymer matrix [110]. Although PLA/HA nanocomposites haven been formulated and shaped using multiple methods, there has not yet been an extensive rheological study of PLA/nHA [78]. Additionally, fused deposition modelling (FDM) for the creation of PLA/HA composites has also not yet been studied extensively [112]. The lack of rheological information and information regarding the FDM process of PLA is important with regards to this study, given that a thickening effect of PLA during the fused deposition modelling could result in nozzle clogging issues, which would disrupt the FDM process.

2.4 Fused deposition modelling

2.4.1 Additive manufacturing

The first successful additive manufacturing (AM) process was patented in 1972 by Ciraud, it consisted of a powder deposition method with an energy beam [113]. Bourell et al. consider the layerwise creation of parts is an essential part of AM processes [113]. Over the years multiple AM processes have been patented, driven by the creation of parts with complex forms, impossible to create with traditional techniques, or by the creation of parts at a lower cost. Multiple AM processes exist: stereolitography (SLA), fused deposition modelling® (FDM®), selective laser sintering (SLS), three dimensional printing, etc. [4] [5] [113] [114] [115]. Table 2 summarises the additive manufacturing techniques.

Table 2 Summary AM processes [116].

State of starting material	Process	Material preparation	Layer creation technique	Phase change	Typical materials	Applications
Liquid	SLA	Liquid resin in a vat	Laser scanning/ light projection	Photopoly-merization	UV curable resin, ceramic suspension	Prototypes, casting patterns, soft tooling
	MJM	Liquid polymer in jet	Ink-jet printing	Cooling & photopoly-merization	UV curable acrylic plastic, wax	Prototypes, casting patterns
	RFP	Liquid droplet in nozzle	On-demand droplet deposition	Solidification by freezing	Water	Prototypes, casting patterns
Filament/ Paste	FDM	Filament melted in nozzle	Continuous extrusion and deposition	Solidification by cooling	Thermoplastics, waxes	Prototypes, casting patterns
	Robocasting	Paste in nozzle	Continuous extrusion	–	Ceramic paste	Functional parts
	FEF	Paste in nozzle	Continuous extrusion	Solidification by freezing	Ceramic paste	Functional parts
Powder	SLS	Powder in bed	Laser scanning	Partial melting	Thermoplastics, waxes, metal powder, ceramic powder	Prototypes, casting patterns, metal and ceramic preforms (to be sintered and infiltrated)
	SLM	Powder in bed	Laser scanning	Full melting	Metal	Tooling, functional parts
	EBM	Powder in bed	Electron beam scanning	Full melting	Metal	Tooling, functional parts
	LMD	Powder injection through nozzle	On-demand powder injection and melted by laser	Full melting	Metal	Tooling, metal part repair, functional parts
	3DP	Powder in bed	Drop-on-demand binder printing	–	Polymer, Metal, ceramic, other powders	Prototypes, casting shells, tooling
Solid sheet	LOM	Laser cutting	Feeding and binding of sheets with adhesives	–	Paper, plastic, metal	Prototypes, casting models

Stereolitography uses the spatially controlled solidification of a liquid resin by photo-polymerisation, using a computer-controlled laser beam or a digital light project with a computer-driven building stage [114]. A pattern is illuminated on the surface of the resin, solidifying the lit areas to a predefined depth, after which the support platform is lowered, recoating the surface of the solidified areas in liquid, to prepare the next layer [114]. The main limitation of stereolitography is the limited number of commercially available resins for processing [114]. A resin has to be a liquid that rapidly solidifies upon illumination with light [114]. Figure 6 visualises the stereolitography process.

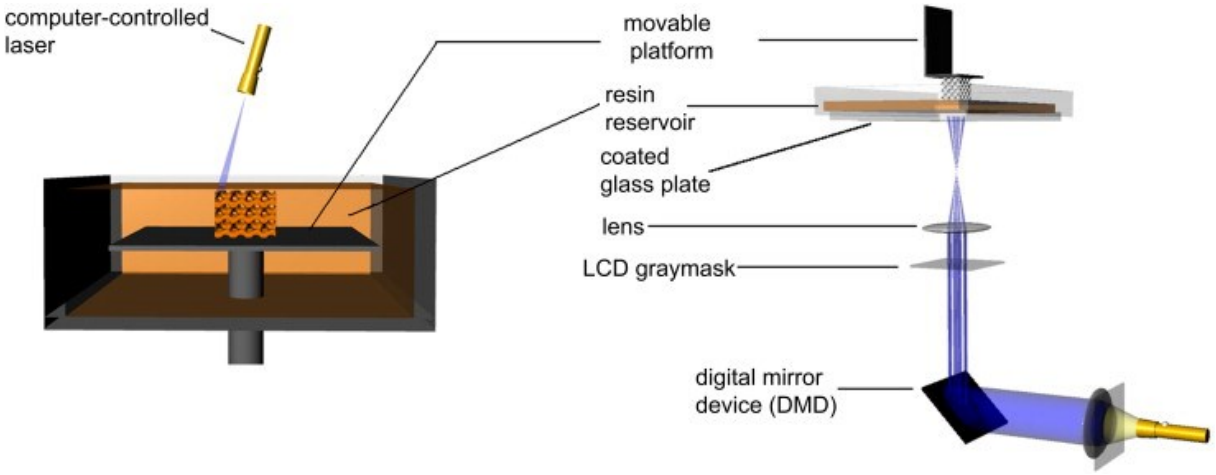

Figure 6 Schemes of two types of stereolithography setups. Left: a bottom-up system with scanning laser. Right: a top-down setup with digital light projection [114].

Unlike stereolithography, which uses a liquid, SLS uses a powder. In SLS, complex three dimensional parts are generated by consolidating successive layers of powder material on top of each other [117]. The consolidation is obtained by processing the selected areas using the thermal energy supplied by a focused laser beam, which is guided using a beam deflection system [117]. A powder deposition system is used for the deposition of successive powder layers [117]. Figure 7 shows the SLS process.

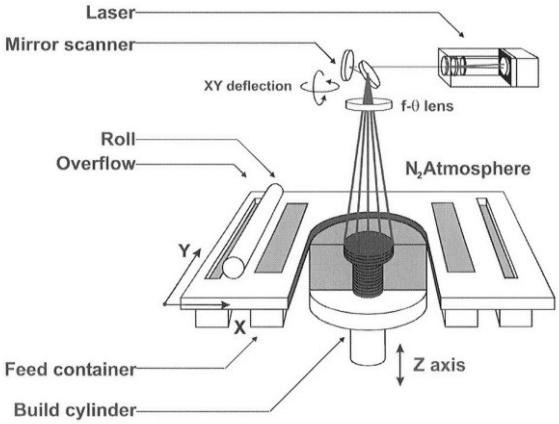

Figure 7 A typical SLS machine layout [117].

Three-dimensional printing (3DP) fabricates three dimensional structures by printing liquid binder solution onto a powder bed with an inkjet [118]. As with the other additive manufacturing processes, 3DP is also a layerwise process. The unbound powder is removed at the end of the manufacturing process. Additionally, the local composition can be manipulated by specifying the appropriate printhead and the appropriate binder (printing parameters alter the local microstructure) [118]. Figure 8 visualises the 3DP process.

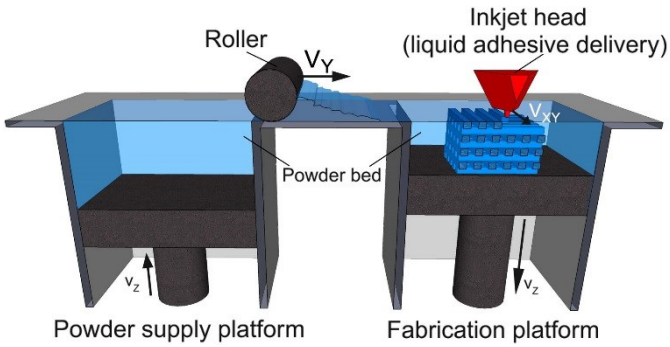

Figure 8 Schematic representation of a typical 3DP™ setup. A roller spreads a thin layer of polymer powder over the previously formed layer, and is subsequently solidified by the spatially controlled delivery of a liquid binder [119].

In general, additive manufacturing techniques use models created by computer assisted design (CAD) to create parts layer by layer [118]. It is this layer by layer approach that allows for the creation of complex geometrical structures, which are impossible to create with traditional subtractive fabrication techniques. Another advantage of additive manufacturing processes is the fast creation of small series without the need to create complicated moulds. Saving time and money as the creation of moulds is an expensive time-consuming step. Hence why AM is usually used for the creation of prototypes to test products before making moulds for large scale production. A disadvantage of AM processes is the potentially low mechanical properties of the workpieces. The low mechanical properties result in prototypes that are not representative for the finished products and often also prevent the usage of AM processes for the creation of finished products. Another problem associated with AM processes is the low repeatability of the fabricated workpieces. Recently there has been a lot of research towards the creation of functional products with AM processes. However, more R&D is needed in terms of designs, materials, novel processes and machines, process modelling and control, biomedical applications, and energy and sustainability applications to broaden the applications of AM technology and elevate it to a mainstream technology [23].

In this paragraph, the pros and cons of each previously discussed technique and fused deposition modelling, which will be discussed more in depth in the next section, will be discussed. Kim and Oh found a strong dependence of the tensile and impact strength on the building direction, with the strength decreasing significantly in the vertical building direction for FDM [120]. They also found that SLA is the most accurate technique followed by SLS, FDM and 3DP [120]. Additionally, the surface roughness was found to decrease with increasing incline for all techniques apart from 3DP, for which it increased instead [120]. Finally, they also compared the cost and manufacturing speed, and found that 3DP was the most advantageous, while SLS showed a better manufacturing speed, but worse material cost compared to the others, as SLS had a high material consumption rate [120]. FDM was found to be cost effective, but the unit cost was relatively high [120]. Vimal et al. compared SLA, SLS and 3DP, and designed a selection process based on the results shown in table 3 [121].

Table 3 Process parameters [121].

Parameters	SLA (SLA3500)	SLS (Sinterstation 2500+)	3DP	LENS (LENS 750)
Reliability	Less	Good, thermal distortion	Less thermal, distortion	High
Strength, density, durability and toughness	Green–fragile, brittle and translucent	100% density, material is cheaper than used in SLA, thermal distortion may occur while post processing, moderate strength	Good strength, 99% density, fragile and porous	Superior strength and ductility
Material	Photosensitive monomer resin (limited choice of resin)	Wide range (nylon, metal, polycarbonate, sand, ABS and wax)	Limited binders and material, (ceramic powder and colloidal silica of polymeric binders)	Stainless steel; iron-nickel alloys; tool steels; Inconel; titanium alloys; tungsten and non-weldable materials
Scanning speed	2.54 m/s (more than one part may be built at once)	5 m/s	Insufficient data	Insufficient data
Layer thickness	0.05-0.1 mm	0.1 mm and wall thickness 0.5-0.7 mm	177 μm	Insufficient data
Build up speed	35 s to recoat and 78 s to solidify 50 × 50	12-25 mm/h	18-25 mm/h	Insufficient data
Accuracy and repeatability	±0.005 mm	±51 μm	±178 μm, stair stepping effect in build direction	± 127 μm, poor finish
Maximum part size	250 × 250 × 250 mm; 56 kg	330 × 380 × 425 mm	355 × 457 × 355 mm	300 × 300 × 300 mm
Material utilization	High	High	Medium as hard to remove excess powder from cavities	High
Manufacturing time	Reasonably fast but several hours for post processing	12 h approximately	5 h approximately	Fast as post processing is not required
Heat source	UV laser wave length (325–354.7 nm); power (6–800 mW)	50 W CO_2 laser	Final firing at a temp of 900 c for 2 h	750 W Nd:YAG laser
Lifetime of machine	Insufficient data	Insufficient data	Insufficient data	Insufficient data
Support	Required	Not required	Not required	Not required
Setup time	less	Less	Less	Less
Post processing	UV oven to post cure up to 6 h, cleaning and finishing	Cleaning and finishing	Dipped in binder and fired to improve strength, removal of powder	No further heat treating or cooling is required; cleaning and finishing
Recyclability	No and uncured resin can be reused	No, powder can be reused after sieving to eliminate globules	No	No
Carbon footprint	Insufficient data	Insufficient data	Insufficient data	Insufficient data
Disposal	Incineration recommended/ landfill (Luo *et al.*, 1999)	Incineration recommended	Land fill or incineration	Incineration recommended
Water	No	No	High	No
Effluents	No	No	Yes	No
Toxicity	High and smelly	Nontoxic and safe	High because of binders	Non-toxic
Radiation	High	High	No	Very high
Airborne	No (may be while finishing)	Yes	High and possibility of emission during heating	Yes
Energy	3 kW	6 kW	High	High
Resources	Medium	Medium, nitrogen is required (atmosphere)	High	Medium

Source: Pham and Dimov (2001), Pham and Gault (1997), Luo *et al.* (1997), Yan and Gu (1995), Levy *et al.* (2003), Kumar and Kruth (2010), Yan *et al.* (2009), Kruth *et al.* (1998)

2.4.2 Fused deposition modelling process

Fused deposition modelling® (FDM®), developed in the late 1980s, is a part of additive manufacturing (AM) [23]. The terms “Fused deposition modelling” and “FDM” are trademarked by Stratasys Inc. (USA), the company which first patented the technology (Crump, 1992), in the United States. Today Stratsys Inc. (USA) is still the major manufacturer of FDM systems [23]. FDM is sometimes referred to as Fused Filament Fabrication (FFF) to avoid the commercial name. In FDM, a plastic filament is heated slightly above its melting point and the resulting molten material is then extruded through a nozzle as a filament to a substrate and cooled down until it solidifies and forms a layer [23]. Figure 9 and 10 show examples of FDM printers. As with the other AM processes, FDM is a layer wise process. Usually the layers consist of an outline and an interior, with the creation of the outline preceding the filling of the interior. The molten filament is deposited in a predetermined pattern, which can be selected during the design process. Recent advances have resulted in the usage of two heads during the FDM process [23]. The second head is often used to deposit breakaway material that supports the workpiece during the process, but is removed once the FDM process is completed (using a solvent,

simply breaking away the supporting material, etc.) [122]. The commercially available materials for this process include acrylonitrile butadiene styrene (ABS), polycarbonate (PC), polyphenylenesulfone (PPSU) and a PC/ABS-blend, provided as filaments (diameter of 1.75 ± 0.05 mm) in several standard colours [123]. Roberson et al. suggested an expansion of FDM applicability through materials development, which isn't surprising given the low amount of commercially available materials [124].

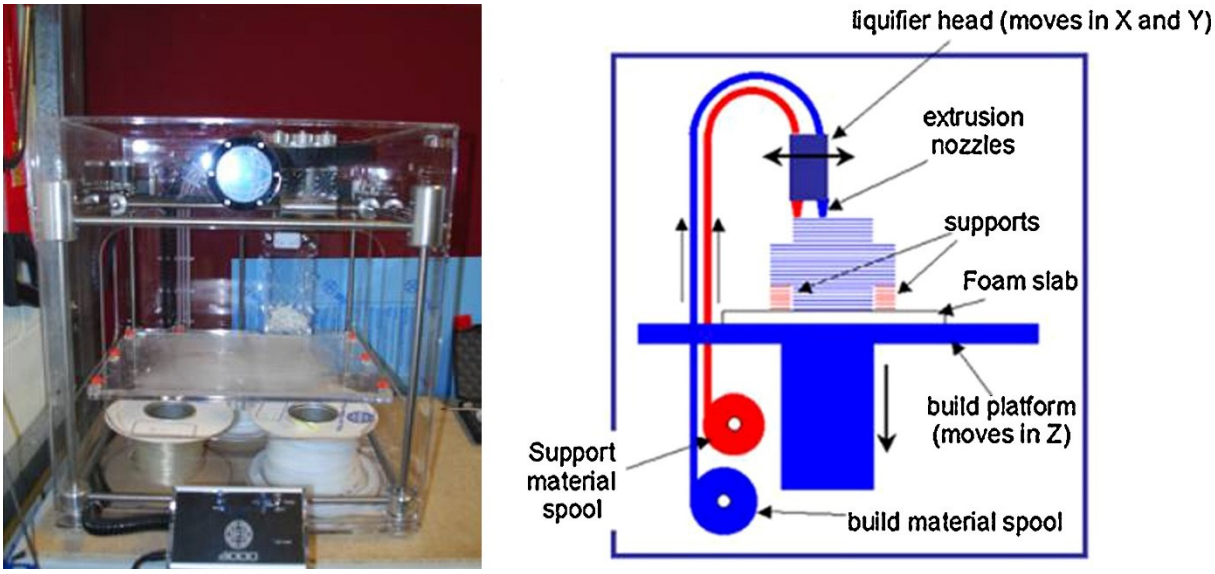

Figure 9 Fused filament fabrication apparatus and schematic [125].

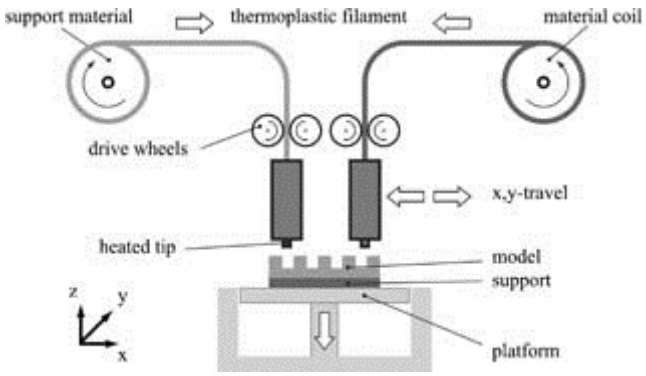

Figure 10 Procedure for fused deposition modelling [123].

The FDM processing parameters include build orientation, raster angle (RA), contour width (CW), number of contours, raster width (RW), raster to contour air gap, raster to raster air gap (RRAG) and slice height (Figure 11) [122]. However, ISO/ASTM52921-13 Standard Terminology for Additive Manufacturing-Coordinate Systems and Test Methodologies should be considered [126]. The build orientation is the orientation of the part with respect to the build platform, while the RA is the angle created by the raster and the positive X direction of the build platform (Figure 12) [122]. CW and RW is the width of the contour and the raster respectively and RRAG is the distance between the edges of two adjacent rasters, negative RRAG results in overlap between adjacent rasters [122]. A negative RRAG can be achieved by changing the speed of deposition, which will result in a different filling. Additionally, defects in the workpiece are possible if the filament diameter varies during the FDM process, resulting in underfill (diameter decreases) or overfill (diameter increases). If the diameter surpasses the limits specified by the manufacturer, the filament will no longer be fed into the printerhead of the FDM process. When the diameter is too big, the filament will not be able to enter the liquefier and if the diameter is too small, the pinch roller mechanism will slip and/or the filament

will bend in between the pinch roller mechanism and the liquefier. The bending of the filament results in the removal of the pressure on the liquefied polymer material and no material will exit the printerhead. Multiple parameters have to be taken into account when creating a workpiece with FDM, to reduce the number of defects within the workpiece: the workpiece geometry; the number of contours; the orientation of the deposition of the molten filament; the speed at which the filament is deposited; the temperature of the material; the flux of the material; the height of the deposited filament; etc. [122] [127] [128] [129]. Each of these parameters can be carefully controlled during the FDM process and is selected during the design phase. If defects do happen, they can be separated into surface defects and internal defects [129]. Two common surface defects are the staircase effect, which is caused by the slice method of manufacturing and can be treated by varying the thickness of the slice or by intermediate processing, and the chordal effect, which originates from the "stl" formate files and is thus software related [129]. Other surface defects include the support structure burrs, start/end errors and the ridged top surface due to the deposition of the arc shaped roads [129]. Internal defects arise due to a mixture of hardware and software limitations and materials characteristics [129]. Sub-perimeter voids are caused by the incomplete filling of the area inside the perimeter of the FDM part, at the point where the path of the FDM printer head approaches the perimeter and are caused by an insufficient material flow to fill the volume at these intersections [129]. Sub-perimeter voids can be avoided by optimising the FDM process. Inner-road voids and road thickness variation defects are caused by inconsistent material flow due to both slipping in the filament feed mechanism and variations in the filament diameter, increasing the grip and controlling the diameter of the filament eliminates these defects [129]. Other defects that may occur are inter-road voids, inter-road delaminations, inter-road errors (discontinuous fill patterns), core voids, etc. [129]. The solution to most defects is careful control and optimisation of the FDM process parameters, additionally, this may also result in better mechanical properties [130].

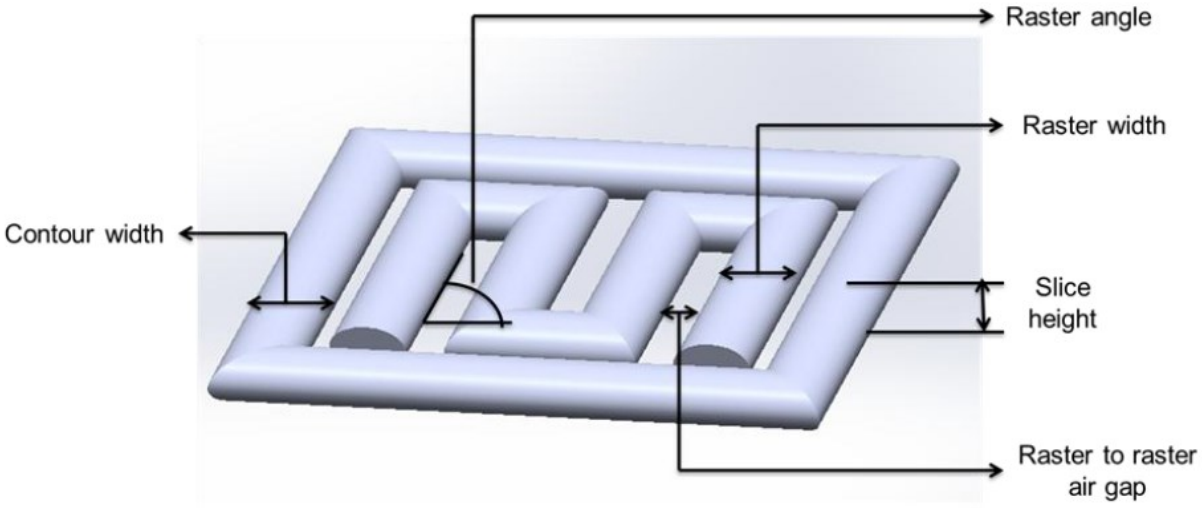

Figure 11 FDM Build Parameters [122].

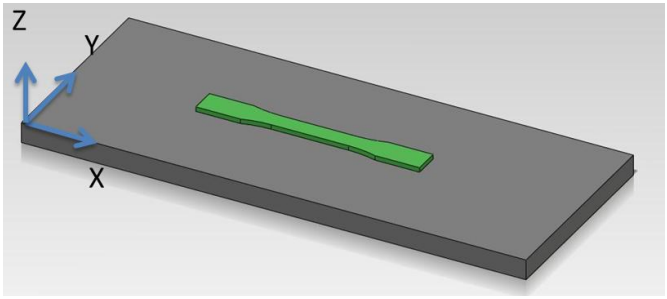

Figure 12 XYZ build orientation based on ASTM F2921-1, which has been replaced by ISO/ASTM52921-13 [122] [126] [131].

Another disadvantage of FDM produced parts compared to injection moulded parts is the reduced mechanical properties of the FDM produced parts. Wendel et al. found that the mechanical properties and the thermal conductivity of a polyamide composite material were at 60% and 70-80% respectively when comparing FDM and injection moulding [123]. Similar results were found for polypropylene by Carneiro et al., as they found a 20-30% reduction of the mechanical properties for the FDM produced parts, when compared to the injection moulded [7]. Wendel et al. also suggested that the optimisation of process parameters will greatly reduce the differences in mechanical properties of parts by FDM and injection moulding in the future [123]. Of course, lowering the difference between injection moulding and FDM, would make the FDM process a lot more interesting and would expand the potential applications. Another thing to keep in mind is the use of composite materials to increase the properties of polymers. FDM parts could have the same mechanical properties as injection moulded parts, by using composites instead of pure polymers during the FDM process. Another important aspect of the FDM process, is the adhesion between and within layers, which is a direct result of the diffusion of the polymer at temperatures above its glass transition temperature. Bellehumeur et al. proposed a model for the bridging between filaments for ABS, but their model did not succeed in characterising all thermal phenomena [132]. In figure 13, the different levels at which the bonding between filaments occur are visualised. Figure 14 shows the bond formation process. At first only the surfaces of two filaments will be in contact, after which a neck growth will occur, followed by diffusion at the interface and finally a randomisation will occur when sufficient diffusion has occurred [132]. One way of speeding up the bonding process, is increasing the polymer infeed, which results in a larger contact surface at the beginning (larger neck) and thus faster diffusion and randomisation.

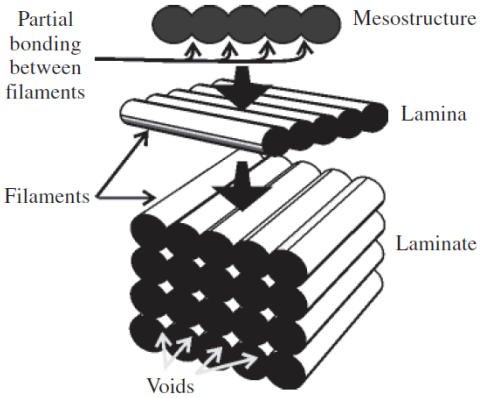

Figure 13 Levels of Analysis for FDM Prototypes [132].

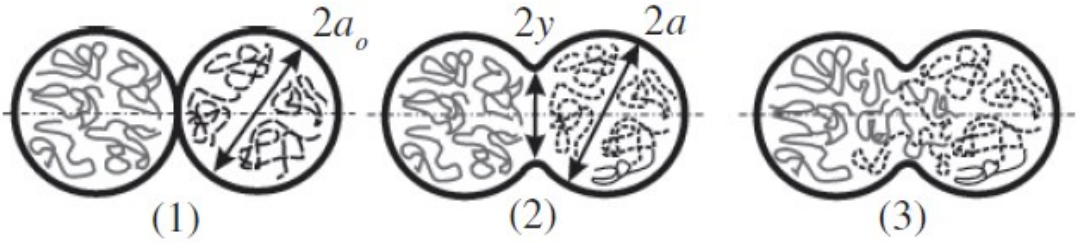

Figure 14 Bond Formation Process Between Two Filaments: (1) surface contacting, (2) neck growth, (3) diffusion at interface, (4) randomization [132].

Carneiro et al. studied the effect of the varying FDM parameters on the mechanical properties of polypropylene (PP) and found that the adhesion between adjacent filaments was independent on the printing orientation; the samples are stiffer in the filament direction; the thickness of the layers has little influence on the mechanical performance of samples; the infill degree effects the mechanical properties linearly; the use of fibres as reinforcement is also effective in 3D printing; and when comparing the FDM samples with compressed samples, the FDM samples showed a mechanical performance loss of 20-30% [7]. De Ciurana et al. studied the influence of the angle of deposition, the slenderness and the distance between filaments during the FDM (RepRap) process on the mechanical properties of PLA and found a higher young modulus for their « crossed » (±45°) model for PLA [130]. They also showed that a greater thickness in combination with a lower inter-filament distance resulted in a higher young modulus [130]. This can be achieved by increasing the height of the deposited filament, decreasing the speed of deposition, increasing the material flux, or a combination of all. Shofner et al. found lower mechanical properties when the raster angle between layers was 10° and 90° compared to a raster angle of 0° [133]. It is becoming apparent that parts created with FDM are anisotropic and the orientation of the filaments is thus an important parameter. Too et al. were able to predict the effect of the raster gap size on the porosity of the structure using an equation, and found that a higher raster gap size resulted in a higher porosity and a lower compressive strength [134]. Ebel and Sinnemann researched the mechanical properties of PLA and ABS FDM parts, printed with multiple printers and found better mechanical properties for the PLA FDM parts, additionally they also found a significant difference between the different printers for PLA and ABS respectively [135]. This indicates that the printer used for the FDM process also affects the resulting mechanical properties.

2.4.3 Nanocomposite materials for FDM

Traditionally, AM has been the subject of studies creating composites with fibres [116]. Ivanova et al and Campbell et al. report agglomeration problems of the nanoparticles during the AM process, accumulation of nanoparticles in the printing nozzle, etc. [16] [136]. Very few publications treat the usage of nanocomposites in the FDM process. Recently the FDM process of polycaprolactone (PCL) and ABS nanocomposites with minerals (montmorillonite and HA) has been studied [137] [138]. Zhang et al. used FDM to print electrical circuits with PLA/Graphene oxide nanocomposites [139]. They found that only 2-8% graphene oxide was needed to highlight the conductive properties of the composite, additionally the orientation of the nanoparticles increased the conductive character of the nanomaterial [139]. Other studies have incorporated carbon micro- and nanofibers in ABS for FDM application [133] [140]. Kumar et al. discuss the processability of nanoparticles in FDM, they indicate that the usage in low quantities does not change the viscosity of the material in the molten state while potentially increasing thermomechanical properties [141].

2.5 Bone tissue engineering

Bone plays multiple roles in the human body, it is integral for the locomotion as it ensures the skeleton has adequate load-bearing capacity and protects the internal organs of the body [142]. Additionally, bone also regulates the Ca and P ions concentration in the blood and remodels throughout the lifetime of an individual [142]. Bone tissue engineering is a complex and dynamic process that initiates with migration and recruitment of osteoprogenitor cells followed by their proliferation, differentiation and matrix formation along with remodelling of the bone [143]. The American Academy of Orthopaedic Surgeons estimates 6.3 million fractures annually in the United States, with over 500,000 bone graft procedures being performed in the U.S., of which 90% were either autograft or allograft bone tissues, and mounting to an estimated cost of $2.5 billion [144]. Autograft (taken from patients own bone tissue), allograft (human donor bone tissue) and xenograft (nonhuman donor bone tissue) bone tissues have disadvantages, there's only a limited amount of autograft material available; allograft and xenograft require a donor, which comes with potential compatibility issues and disease transmission; and all are viable to contamination [144]. Synthetic or alloplastic bone grafts are osteoconductive materials that are abundantly available and eliminate the risk of disease transfer and procurement morbidity [145]. Ideally, the synthetic bone graft material should mimic bone in both mechanical and osteogenic properties, which leads to the following four characteristics that an ideal bone graft material should possess [145]:

- Osteointegration, the ability to chemically bond to the surface of bone without an intervening layer of fibrous tissue.
- Osteoconduction, the ability to support the growth of bone over its surface.
- Osteoinduction, the ability to induce differentiation of pluripontential stem cells from surrounding tissue to an osteoplastic phenotype.

These characteristics can be linked to the following key properties that an implant should possess as identified by authors in the literature [144] [146] [147] [148] [149]:

- Biocompatibility: An implant cannot be rejected by the organism; nor can it be toxic, mutagenic, antigenic or carcinogenic.
- A structure similar to the naturally occurring extracellular structure, to promote cell proliferation and cell-specific matrix production and to avoid stress shielding (Chemical modification is an option [116]).
- An open-pore geometry with a highly porous surface and microstructure with interconnected porous networks, that allows cell in-growth and reorganization in vitro and provides the necessary space for neovascularization from surrounding tissues in vivo (50-90% porosity; macropores of 200-400 μm and micropores of 20-125 μm).
- Mechanical properties similar to bone,
- Sterilisable,
- Controlled degradation that allows for the reconstruction of bone, which gradually takes the place of the implant. Additionally, the implant should retain some of its mechanical properties during the degradation.

The degradation of the implant results in space for bone growth, which makes a second operation to remove the implant unnecessary [148] [150]. By reducing the number of operations, the usage of

degradable implants indirectly results in freeing operating theaters and reducing the probability of nosocomial disease for a patient. A degradable implant has to be degradable by either hydrolysis or enzymatic activity, in a slow enough fashion to allow for the bone to regenerate.

2.5.1 Hydroxyapatite composites

Synthetic HA is a calcium phosphate bioceramic with chemical composition (Ca/P ¼ 1.67) and structure similar to the main inorganic constituent of natural bone; it has bioactive, biocompatible, biodegradable and osteoconductive properties [94] [95] [99]. HA has been intensively investigated as bone repair material, but a low mechanical flexural strength and fracture toughness (high brittleness) restrict its application in regeneration and repairing of new bone tissue at load-bearing sites [74] [99]. One way of overcoming this weakness, is the combination with polymers. The HA will act as a reinforcing material to improve the mechanical properties of the polymer and can improve the osteoconductivity of the polymer [94]. The advantage of the polymer lies within its matrix being though and flexible, improving the toughness of the whole system [99]. PLA, PGA and PLGA have been widely reviewed and considered as polymer matrices in HA based composites for applications in medical devices, and scaffolds for bone tissue engineering [99] [151] [152] [153]. Nejati et al. showed the interest of PLA, given the interaction between the hydroxyl group of HA and carbonyl group of PLA as mentioned before [19].

2.5.2 Fused deposition modelling for bone tissue engineering

FDM allows for the rapid manufacturing of custom implants within hours of the patient's arrival in the hospital. Additionally, due to the computer aided design (CAD) employed during the creation of the implant for the FDM process, the pore network and pore size can be controlled. This could result in better cell in-growth and reorganization and provide the necessary space for neovascularization from surrounding tissues. The materials utilisable are restricted to those available, but among the available materials there is PLA. PLA is a biodegradable material that also degrades in the human body, as discussed earlier. The degradation products are also produced by the body, reducing the toxicity of the implant, but inflammation of surrounding tissue can still be problematic. Due to the fact PLA degrades by hydrolysis in the human body, the control of the porosity, pore network and molar mass also results in the control of the degradation speed, the higher the contact surface the faster the degradation. So far the usage of PLA nanocomposites has not yet been studied extensively for the FDM process. However, PLA/HA nanocomposites could prove to be very interesting for the creation of implants with FDM.

2.6 Application of nanocomposites in packaging materials

The addition of nanoparticles to improve material properties, has been the interest of scientists for a few decades [99]. Specific types of nanofillers can enhance several properties of a neat polymer in a synergetic manner; broadening the field of application of the nanoparticles [99]. Organoclays, hydroxyapatite and carbon nanotubes have been widely used in polymer nanocomposites [99].

2.6.1 Barrier properties

Barrier materials restrict the passage of gases, vapours and organic liquids through their boundaries, polymers dominate the packaging industry but are also used in other industries [154]. An absolute barrier does not exist; barrier properties depend mainly on the used polymer structure and should be adapted for each application [155]. Permeation through polymer materials is the result of two processes: diffusion (kinetic quantity) and solubility (thermodynamic quantity) [156].

$$P = D * S \qquad (3)\ [156]$$

Solubility can be linked to the chemical relationship between the permeant molecule and the polymer [154]. The diffusion rate is dependent upon the size of the permeant molecule and the amorphous configuration of the polymer [154]. Diffusion is a flow of matter resulting from a chemical potential difference of migrant material in different locations of the system [155]. The permeability of a certain permeant is the amount of permeant that passes through a sample surface within a certain time and under a certain pressure. The permeation flux (J) is defined as the quantity of matter that passes through the material; the permeation flux follows Fick's first law, which establishes the proportion between J and the concentration gradient of the permeant normal to the cross-section of the sample [157] [158].

$$J = -D\frac{\partial C}{\partial x} \qquad (4)\ [157]\ [158]$$

The diffusion and solubility coefficients are considered independent of the permeant concentration; therefore, the steady-state flux can be related to the permeability and the pressure difference by permeating through the membrane by the following relationship [155]:

$$J = D * S * \frac{\Delta p}{e} = P * \frac{\Delta p}{e} \qquad (5)\ [155]$$

$$P = J * \frac{e}{\Delta p} = \frac{Q*e}{S*t*\Delta p} \qquad (6)\ [155]$$

With Q = the quantity of permeant traversing the sample,
S = the sample surface,
e = the sample thickness,
t = the time,
Δp = the pressure difference between the two sides of the sample.

It is important to know that the permeability coefficient measures relative permeation behaviour and is used to compare the permeability of different polymers [154]. Permeability is the proportionality constant in the general equation for mass transport of a penetrant across a barrier, as seen in equation 7 [154].

$$\frac{\Delta m_{penetrant}}{\Delta t} = P\ \frac{A\,\Delta p}{l} \qquad (7)\ [154]$$

P = the permeability of the barrier material,
$\Delta m_{penetrant}/\Delta t$ = the transmission rate,
A = the surface area of the barrier,
Δp = the partial pressure difference across the barrier,
l = the thickness of the barrier.

The permeant (gas or vapour) will undergo three stages during permeability tests: in the first stage the permeant is absorbed in the polymer material; in the second stage the permeant will diffuse through

the polymer matrix under the influence of a concentration gradient; and in the third and final stage the permeant undergoes desorption through the polymer wall and is evaporated from the polymer surface [154]. When measuring the permeability, there will be a transition from a pseudo steady-state to a steady-state, as the polymer will slowly become saturated with the permeant. Once saturated, the permeability remains constant. Unless if the permeant affects the polymer matrix, in which case the permeability might increase or decrease over time depending on the effect of the permeant on the polymer matrix. Factors influencing the permeability through a polymeric film can be divided into three categories: external; due to the permeant; and due to the polymer [156] [159] [160]. External factors such as temperature (T), pressure (p), concentration (c), humidity (RH), etc. are often kept constant or carefully controlled throughout the permeability measurements. The influence of the permeant is a direct result of its solubility, molecular shape, weight, etc. Shogren et al. found that the values of the water vapour transmission rate (WVTR) were positively correlated with higher polymer solubility parameters, lower crystallinities, and higher free volumes [161]. Poley et al. found that the permeability decreased when the size of the molecules increased [162]. They also showed that for certain permeants, the dependence of the permeability coefficients on the temperature can be defined by an Arrhenius equation [162]:

$$P = P_0 \exp\left(-\frac{E_p}{RT}\right) \qquad (8)\ [162]$$

Tsuji et al. show that changes of the molecular average weight from $9*10^4$-$5*10^5$ g/mol and D-lactide content of PLA films in the range of 0-50% have insignificant effects on their WVTR [163], while the WVTR decreased monotonically with increasing crystallinity from 0 to 20% and levelled off from crystallinities exceeding 30%. Song et al. showed that the incorporation of hydrophobic-modified nano-cellulose fibres into the PLA matrix resulted in a lower WVTR [164]. Dong et al. compared the barrier behaviour of both stretched and annealed PLA films with regular PLA films, they found an increase in oxygen and water vapour barrier for annealed and stretched PLA films compared to undrawn PLA at middle draw ratio (Further stretching reduced the barrier properties) [165]. Dong et al. found the annealed PLA film to have higher barrier ability than that of the stretched PLA film, additionally, they also found an increasing oxygen transmission rate (OTR) with increasing temperature, while the WVTR reduced slightly; and both OTR and WVTR were insensitive to the humidity [165]. Ducruet et al. studied the effect of the crystallinity of PLA samples plasticised with acetyl butyl citrate on the barrier properties against ethyl acetate and oxygen and found increased barrier properties against ethyl acetate, but no effect of the crystallinity on the OTR of PLA [166]. Colomines et al. found similar results for normal PLA films and concluded that the crystallinity does not influence the OTR of PLA [167]. Chowdhury et al. reported a decreasing permeability with the inclusion of layered nano-silicates in the PLA matrix, which they linked to the creation of a tortuous path, linked to the shape of the platelets (Platelets were considered parallel) [168]. Others have also turned to nanocomposites to reduce the OTR & WTVTR of polymers, relying on the creation of a tortuous path [160] [169] [170] [171].

OTR is usually reported in cubic centimetres of gas that pass through a square meter of film in 24h when the gas pressure differential on one side of the film, at a specified temperature, is one atmosphere greater than that on the other side (Normalised units: $cm^3*mm/m^2*day*atm$) [154]. WVTR is reported as grams of water which will pass through a given area of material in a specified time, the usual units are grams per 1 square meter per 24 h at a specified temperature and humidity differential (Normalised units: $g*mm/m^2*day$) [154]. Different methods exist to determine the gas

permeability (OTR & carbon dioxide transmission rate) and the water vapour permeability of polymer films. OTR methods can be divided into isobaric methods, variable pressure methods, differential methods and a fluorescence-based oxygen sensor method [155] [172] [173]. WVTR methods can be divided into gravimetric methods, electrolytic sensor detection method, infrared detection sensor method, humidity detection sensor method [174]. The methods used in practise to determine the permeability, mostly correspond to the ones described in the norms. Norms differ from country to country, but also within companies.

Gravimetric detection WVTR:

- ISO/FDIS 2528: Sheet materials, determination of water vapour transmission rate Gravimetric (dish) method [175].
- ASTM E96/E96M-16: Standard Test Methods for Water Vapor Transmission of Materials [176].
- ASTM D1653-13: Standard Test Methods for Water Vapor Transmission of Organic Coating Films [177].

Electrolytic detection WVTR:

- ISO 15106-3:2003: Plastics, film and sheeting, determination of water vapour transmission rate (Part 3) [178].

Infrared detection WVTR:

- ISO 15106-2:2003: Plastics, film and sheeting, determination of water vapour transmission rate (Part 2) [179].
- ASTM F1249-13: Standard Test Method for Water Vapor Transmission Rate Through Plastic Film and Sheeting Using a Modulated Infrared Sensor [180].
- TAPPI T557: Water vapor transmission rate through plastic films and sheeting using a modulated infrared sensor [181].

Humidity sensor for WVTR detection:

- ISO 15106-1:2003: Plastics, film and sheeting, determination of water vapour transmission rate (Part 1) [182].
- ASTM E398-13: Standard Test Method for Water Vapor Transmission Rate of Sheet Materials Using Dynamic Relative Humidity Measurement [183].
- TAPPI T523: Dynamic Measurement of Water Vapor Transfer Through Sheet Materials [184].

OTR methods:

- ASTM D3985- 05(2010)e1: Standard Test Method for Oxygen Gas Transmission Rate Through Plastic Film and Sheeting Using a Coulometric Sensor [185].
- ASTM F1307-14: Standard Test Method for Oxygen Transmission Rate Through Dry Packages Using a Coulometric Sensor [186].

- ASTM F2622-8: Standard Test Method for Oxygen Gas Transmission Rate Through Plastic Film and Sheeting Using Various Sensors [187].
- ASTM F1927-14: Standard Test Method for Determination of Oxygen Gas Transmission Rate, Permeability and Permeance at Controlled Relative Humidity Through Barrier Materials Using a Coulometric Detector [188].

2.7 Research strategy

In this study, the PLA and HA will be melt-mixed using a twin-screw extruder (TSE), similar to the process described by Öner and İlhan for the creation of poly(3-hydroxybutyrate-co-3-hydroxyvalerate) hydroxyapatite nanocomposites [189]. The characterisation of the materials will be done with the following techniques: thermogravimetric analysis, differential scanning calorimetry, oscillatory rheology, tensile tests, dynamic mechanical analysis, wide-angle x-ray diffraction analysis, transmission electron microscopy and permeability test [53] [97] [99] [127] [163] [166] [190]. The thermogravimetric analysis helps determine the start of the degradation of the PLA composites, with this information it is possible to determine the maximum printing temperatures of the FDM process. Additionally, the thermogravimetric analysis also helps determine the HA content in the composites. Differential scanning calorimetry analysis help determine the fusion temperature of the obtained PLA composites for different process steps. Especially the fusion temperature of the filaments is important, as this is the minimum printing temperature during the FDM process. The differential scanning calorimetry also aids in the determination of the crystallinity of the composites for different process steps, which might explain certain phenomena. Oscillatory rheology helps predict nozzle clogging during the FDM process, as it shows potential thickening effects and thus helps assure the continuity of the FDM process. Tensile tests will be used to compare the mechanical properties of composites with different HA content. Doehlert response surface methodology is used to determine the maximum mechanical properties of each composite for the comparison. Additionally, the FDM printed tensile samples will be compared with injection moulded samples to determine the influence of the FDM process on the mechanical properties of the composites. The dynamic mechanical analysis, will help verify the glass transition temperature of the composites. Results of the dynamic mechanical analysis will also be used to compare the mechanical properties of the composites. The influence of the FDM process will be determined by comparing the printed samples with compression moulded samples. Following Carneiro et al., who used compression moulding as a reference process due to its simplicity and the low degree of resulting anisotropy, the injection moulding and compression moulding are reference processes for the FDM process [7]. Additionally, they also help verify whether the addition of filler resulted in a recovery of the mechanical properties, potentially lost by the FDM process. The interest of the wide-angle x-ray diffraction analysis lies in the determination of the inter crystal distance, which is an indication for the size of the HA particles, which in turn will be verified with transmission electron microscopy. Finally, the permeability of the composites is determined by creating composite films and consecutive permeability tests. These tests help determine the porosity of the composites and the results could be interesting for bone tissue engineering applications.

3 Materials and methods

3.1 Materials

An nHA aqueous paste (30 ± 3 wt.%) was bought from Fluidinova (Reference: nanoXIM•HAp103). The nano-hydroxyapatite particles are suspended in pure water and have a rod-like shape. Typically, their particle size is below 50 nm (30-40 nm in length and 5-10 nm in width). Fluidinova also indicates that the specific surface area is greater than 80 m^2/g.

The PLA was supplied by NaturePlast, it was an extrusion graded PLA and had NaturePlast PLE 005 as sales name. PLE 005 is a thermoplastic PLA resin from non-genetically modified renewable plant resources. Additionally, it is recyclable and industrially compostable following norm NF EN 13432:2000 [191].

3.2 Methods

3.2.1 Shaping process

3.2.1.1 Twin-screw extrusion

The goal of the twin-screw extrusions is to obtain a PLA/nHA composite material starting from polylacticacid (PLA) and a nano hydroxyapatite (nHA) aqueous paste with an nHA content of 30 wt.%. Given the state of the materials and as to not lose too much HA paste, it was more convenient to first extrude a masterbatch, followed by a dilution in the extruder after a HA content analysis with a thermogravimetric analysis. The solvent casting process was not considered, since traces of toxic solvent would prevent the usage of the composites for bone tissue engineering.

For the extrusion of the masterbatch, both the PLA and nHA aqueous paste were mixed in a twin-screw extruder, the target concentrations of nHA for the masterbatch was 10 %wt. After the verification of the HA content in the masterbatch, the masterbatch was diluted to obtain PLA/nHA composites with HA concentrations of 0; 0.5; 1; 3 and 5 wt.%. Before the extrusions the PLA pellets were dried for a week at a temperature of 60°C and the night before the extrusion at a temperature of 80°C. In both cases the drying took place in the presence of aqua scavenging silica crystals. After each extrusion, the PLA pellets were put back in the oven at a temperature of 60°C in the presence of the silica crystals. The hydroxyapatite paste on the other hand was shaken and put into syringes the day of the first extrusion. During the extrusion, the syringes were used to add the nHA paste with a 10 g/min feed rate.

A Clextral BC21 co-rotating twin-screw extruder (ESIReims, France) was used for the extrusion. On the extruder, there were 8 heating zones (1-8) with individual temperature settings and one zone with no heating (zone 0). It is important to note that the temperatures are only guidelines for the extruder and thus not constant throughout the extrusion process. Additionally, the measured temperatures are not material temperatures. The screw profile used during the experiment is illustrated in table 4 and figure 15. Screws can be divided into screws, which have a direct path; screws with an inverse path and screws with a neutral path. A direct path indicates that a screw pushes the material forward, while an inverse path is a screw which pushes the material in the opposite direction due to its threads.

Table 4 Screw profile.

N°	Screw type	Thread length per period (mm)	Screw length (mm)	Path	Thread type	Angle
1	conveying	33	50	direct	U	
2	conveying	33	50	direct	U	
22	conveying	25	50	direct	V	
6	conveying	16	50	direct	V	
27	conveying	25	25	inverse	Grooved V	
18	mixer	16	25	direct	V	
50	mixer	25	50			90
45	conveying	25	50	direct	V	
15	conveying	25	25	direct	V	
16	conveying	25	25	direct	V	
24	conveying	16	50	direct	V	
19	conveying	16	25	direct	V	
53	conveying	25	12,5	inverse	V	
56	conveying	25	12,5	inverse	V	
48	conveying	33	50	direct	V	
21	conveying	33	50	direct	V	
47	conveying	33	50	direct	V	
17	conveying	25	25	direct	V	
41	conveying	25	25	direct	V	
51	conveying	16	50	direct	V	
7	mixer	25	25	inverse		- 45
44	mixer	25	25	inverse		- 45
46	conveying	25	25	direct	V	
5	conveying	25	25	direct	V	
25	conveying	16	25	direct	V	
26	conveying	16	25	direct	V	

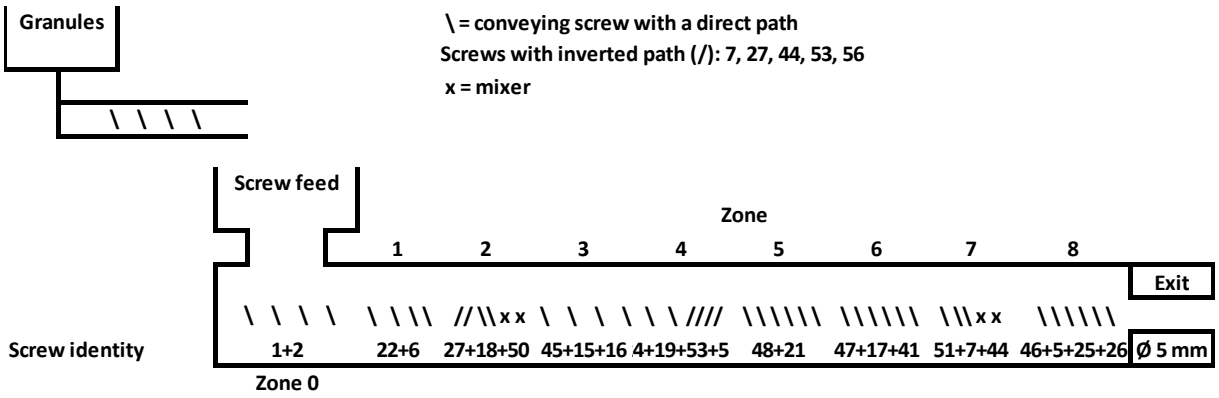

Figure 15 Screw profile extrusion.

During the extrusion process polymer pellets were put into the granules section of the extruder. At the bottom of this section there was a feed screw with adjustable speed. This screw controlled the polymer feed and thus the output flow of the extruder. When the screw turned, polymer pellets dropped into zone 0, the feed zone of the co-rotating screws. From here they were transported through the 8 heating zones towards the exit of the extruder. In zone 3 the hydroxyapatite paste was added to the

polymer material after which the polymer material and the hydroxyapatite paste turned into one supposed homogenous flow of material.

Once the material left the extruder, it passed through a water bath leading up to a rolling carpet, which pulled the polymer filament towards the Scamia granulator 960001 GR (ESIReims, France). The final step of the extrusion consisted of the collection of the newly formed polymer pellets at the bottom of the granulator.

3.2.1.2 Single-screw extrusion

An AXON BX 10 single-screw extruder (IFTS, Charleville-Mézières, France) with a constant extrusion speed, at 20% of its maximum speed, was used to convert the PLA/HA composite pellets into filaments. The infeed of the pellets into the extruder was done with a simple gravity system. The extruder had 3 heating zones, the temperature of each zone could be adjusted separately. Directly after the extruder there was a water bath to cool down the polymer material. In this case, it was a hot water bath as the water circulation was turned off to avoid filament distortion by making the quenching step less abrupt. After the bath, a pinch roller mechanism of a Haake PP1 granulator (IFTS, Charleville-Mézières, France) was used to pull the filament with a constant speed. This to obtain a constant diameter, which was important for the FDM process, which only worked with filament diameters of 1.5-1.6 mm. The final step consisted of the winding of the filaments on coils.

3.2.1.3 Fused deposition modelling and Doehlert methodology

3.2.1.3.1 Fused deposition modelling

FDM was done with a Makerbot Replicator 2 (IFTS, Charleville-Mézières, France) and the printed samples were conforming with 5A-type tensile test specimen from ISO 527-2 [192]. In FDM an electric motor-controlled pinch roller mechanism is used to supply a filament to a heated liquefier. The filament supplied to the liquefier has two states, in the first state the filament is still solid and will exert pressure on polymer material that is already in the liquefier. The second state consists of melted filament, that is pushed through a print nozzle by filament in the first state. The combination of the liquefier and the print nozzle will be called the “printer head”, although an alternative name could be the “extruder head” as the process is very similar to an extrusion albeit without screw. Note that the diameter of the liquefier (1.8 mm) is significantly larger than the diameter of the opening in the print nozzle (0.4 mm). As material is pushed through the print nozzle, the printer head moves across a platform, on which the polymer material is deposited. The printer head only moves in the horizontal plane, while the platform is lowered after the completion of each layer.

The speed of the printer head can be varied depending on the section of the printed object. In this case, the speed was kept constant throughout the entire printing process. A printed object consists of multiple layers; each layer consists of a contour and a raster filling. Within each layer, the orientation in which the material is deposited can vary. In this case, the print orientation was rotated 90° after each layer. Additionally, the contour consisted of two lines that followed the shape of the printed object and the raster filling was 100%, indicating that theoretically there were no air gaps between neighbouring raster lines. Besides the orientation of the material, the height of the deposited polymer material could also be adjusted, however the height was kept constant at 0.2 mm. This height is a compromise between the printing resolution, the manufacturing time and the ability to deposit the

melted filament. A high resolution leads to a high manufacturing time, which is not practical. On the other hand, a too low manufacturing time results in substandard mechanical properties. If the height of the deposited filament increases, the chances of filament distortion increase, which can result in bad contact between layers and thus in lower mechanical properties. Finally, the temperature of the liquefier and the printing speed could also be adjusted. Bellehumeur et al. and rheological analysis showed that the shear rate and temperature impact the bonding quality non-linearly [132]. This leads to the hypothesis that the printing speed and temperature have a non-linear effect on the mechanical properties of the printed samples.

3.2.1.3.2 Doehlert methodology

The goal of this study was to determine the evolution of the tensile properties in function of the printing speed and temperature. Multiple techniques exist to determine this evolution. In this case a Doehlert matrix (design of experiments) was used to determine the theoretical response of the tensile properties on changing printing temperature and speed, based on measurement points [193]. The temperature was fixed at three levels and the printing speed at five levels, resulting in 7 measurement points. In accordance with the Doehlert method, the 7 points formed a hexagon with the distance between neighbouring points being the same [193] [194]. This is due to the principle of uniform space-filling, which uses simplex, which for two factors is an equilateral triangle [193] [194]. For each measurement point, 5 tensile test samples were printed per nanocomposite. One week after the printing process, the tensile test samples of each nanocomposite were tested and based on the results, the optimal settings were used for the FDM printing of dynamic mechanical analysis samples for each nanocomposite. Figure 16 schematically shows the different measurement points of the Doehlert matrix in code-unit according to the Yates notation, useful for matrix calculations. Table 5 gives the printing speed-temperature coordinates of the different points of the Doehlert matrix. The Doehlert matrix can be used to model the response of the mechanical properties on the changing printing speed and temperature.

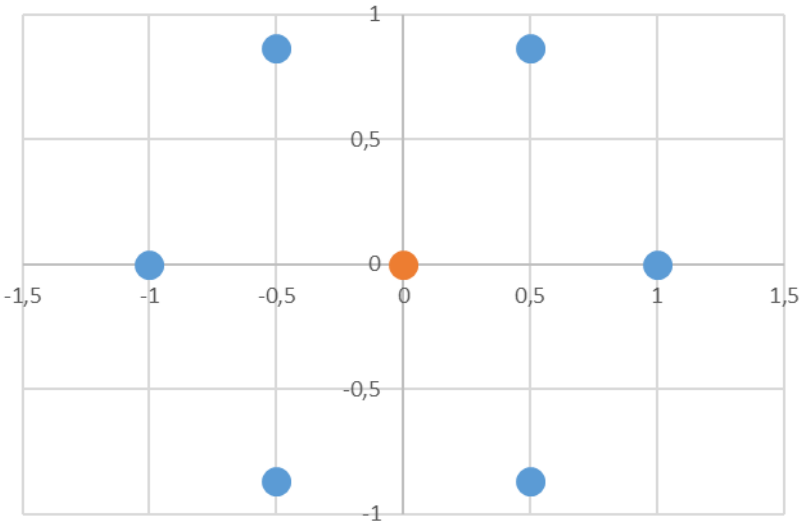

Figure 16 Schematic representation Doehlert matrix.

Table 5 Measurement points corresponding to the Doehlert matrix.

Point	Coded Speed	Coded Temperature	Printing speed (mm/s)	Printing temperature (°C)
1	1	0	105	225
2	0,5	0,866	90	240
3	-0,5	0,866	60	240
4	-1	0	45	225
5	-0,5	-0,866	60	210
6	0,5	-0,866	90	210
7	0	0	75	225

The theoretical Doehlert model is given by the following equation:

$$y_{th} = a_0 + a_1.x_1 + a_2.x_2 + a_{12}.x_1.x_2 + a_{11}.x_1^2 + a_{22}.x_2^2 + \varepsilon \qquad (9)\ [193]$$

With y_{th} the theoretical response (Young's modulus) of a chosen configuration,
a_i, a_{ii} and a_{ij} the coefficients of the mathematical model,
x_i the level of factor I,
ε the residue.

The coefficient a_0 corresponds to the central point in the Doehlert matrix. If the effects of the first order and the interaction between the variables are not dominant, a_{11} and a_{22} give information with regards to the presence of a minimum when both their values are positive and the presence of a maximum when both their values are negative, in the studied domain. When the signs of a_{11} and a_{22} are opposite, there will be nor a minimum nor a maximum. Instead, the response surface will be shaped like a horse saddle. The interaction coefficient a_{12} will shape the diagonal curve, a positive value indicates that the response will increase when the values of the two factors have identical signs and will decrease when the values have opposite signs. When the absolute value of a_{12} increases, the curving of the response surface will start to look more like a horse saddle, making it impossible to obtain an optimum. A_1 and a_2 indicate a shift of the potential optimum towards one of the borders of the studied domain. Hence why the optimum is only present when the effects of the second order are dominant and their coefficients have identical signs. Finally, ε (the residue) is the lack-of-fit and is the same for each experimental point apart from the central one, in accordance with the property of iso-variance of the Doehlert matrix.

The Doehlert model was verified using the coefficient of determination (R^2), which was calculated with the following formula.

$$R^2 = 1 - \frac{\sum_{i=1}^{n}(y_i - y_{th,i})^2}{\sum_{i=1}^{n}(y_i - y_m)^2} \qquad (10)$$

With R^2 the coefficient of determination,
y_i the measured response,
$y_{th,i}$ the value calculated by the model,
y_m the average of the measured values.

Note that the coefficient of determination is directly dependant on the residue as it uses the difference between the experimentally measured values and the values calculated by the model. When the residue is high in value, the determination coefficient will be low. Both the residue and the determination coefficient give an indication of how close the model is to the reality. However, it is important to compare them to the standard deviation of each response. When the standard deviation

of each experimental point is higher than the residue in value, the interpretation of the model becomes impossible. This since the fit of the model, indicated by R^2, could be a coincidence.

Tensile tests were carried out on the printed ISO 527-2 5A tensile test samples of each formulation, to determine the mechanical properties [192]. A pairwise analysis of variance (ANOVA) test was carried out between different points of the Doehlert matrix of the same formulation. The results of the ANOVA test indicated whether the two mean values were different or whether it was impossible to conclude about a possible difference. For all mixtures, the theoretical models were temporarily accepted when the determination coefficient was bigger than 0.8 and if the inter formulation ANOVA tests resulted in at least one pair of coordinates that differed from each other. If this was the case, the p-value was calculated for each coefficient of the theoretical model of the respective formulation and when the p-values of each coefficient were smaller than 0.1, the models were accepted. However, the p-value of a coefficients only gives an indication about the low probability that the respective coefficient is zero. As mentioned before, if the standard deviation is high, then a perfect fit could potentially be a coincidence. Hence why the ANOVA tests are important, the obtained ANOVA p-values between experimental points had to be low and in combination with a high R^2 value. Where the low ANOVA p-values between experimental points validate the experimentations, allowing for an impact caused by changing parameter values. The high R^2 value, validates the model.

3.2.1.4 Injection moulding

The injection moulding of tensile test samples was done with a Babyplast 6/10P (INRA, Reims, France). Before the injection moulding, PLA pellets of each nanocomposite and pure PLA were dried for a week at a temperature of 60°C and in the night before the injection moulding at 80°C. The Babyplast was equipped with a preheated and humidity controlled pellet container (Moullo X Dry air). Polymer material was inserted into this preheated container from which it was fed into the Babyplast. Inside the Babyplast, an Ø 18 mm screw passed the polymer material through the three heating zones before being injected into the mould. In this case the Babyplast was equipped with an ISO 527-2 5A tensile test sample mould [192]. During the injection, the polymer material was injected into the mould in two cycles. The pressure during the cycles was not the same, during the second cycle the pressure was much lower. Additionally, the mould was water cooled as the Babyplast was equipped with a fridge for the cooling of the mould after injection. Once the cooling process was done, the mould would open and the tensile test sample was automatically ejected.

3.2.1.5 Heated hydraulic press

The compression moulding of dynamic mechanical analysis and oscillatory rheology samples was done with a Carver press (ESIReims, France). Dynamical mechanical analysis samples consisted of 60x13x2 mm beams, while the oscillatory rheology samples were discs with a 25 mm diameter and a 2 mm height. PLA/HA pellets of each formulation and PLE 005 were dried at 60°C under vacuum for an hour, followed by continuous storage under vacuum at ambient temperature. Right before the pressing, 10 g of each formulation was divided over 4 moulds each for the dynamic mechanical analysis. For the oscillatory rheology samples, 21 g of each formulation was divided over 3 moulds. The moulds consisted of an upper plate, a bottom plate and a middle plate which held the forms and canals to help surplus material leave. All the plates were separated from each other with Teflon sheets, which

facilitated the separation of the plates after pressing. The Carver press was preheated at 210°C and set to compress at 490.5 kPA. The following pressing procedure was used:

- The press was preheated at 210°C.
- The mould filled with polymer material was brought into contact with the preheated press for 30 minutes.
- After 30 minutes, the pressure was increased to 490.5 kPA and kept there for 15 minutes.
- After the additional 15 minutes of pressing (total time: 45 minutes), the mould was removed from the press and left to cool down at room temperature.
- Once the mould was cool, the test samples were removed and stored under vacuum to prevent moisture absorption.

A Specac Atlas press (ESIReims, France) was used to create films for permeability tests. The films had an average thickness of 90 µm and a diameter of 5 cm. An aluminium mould was created using two thin sheets of aluminium and a 100 µm sheet with a 9 cm Ø hole, the thin sheets had to be replaced after each session, while the thick sheet was reusable. Films were created for each of the formulations following the same procedure. First the press was preheated at 210°C, after which, 0.4 g of granules, in an aluminium mould, were inserted in the press. The first 5 minutes, the press was only put into contact with the mould to allow the granules to melt. After that, the pressure was increased to 1 ton for 30 seconds. Once the 30 seconds had past, the pressure was removed, but the mould was kept in the press for an additional 30 seconds. Finally, the aluminium mould was exited from the press. When the mould was at room temperature, the aluminium mould was opened and the resulting films were removed from the mould.

3.2.2 Characterisations

3.2.2.1 Thermogravimetric analysis

A Netzsch TG 209 F3 (ESIReims, France) was used for the thermogravimetric analysis (TGA) of the PLA as well as the extruded PLA/nHA (0%; 0,5%; 1%; 3% and 5%) composite granules, filaments and FDM printed samples. Every thermogravimetric analysis took place under oxidising conditions and each formulation was tested at least 3 times to ensure repeatability.

Before the thermogravimetric analysis polymer pellets of each mixture were dried under vacuum at 60°C for one hour, followed by continuous storage under vacuum at ambient temperature for a week. A portion of the pellets was then stored in smaller containers, without controlled atmosphere. This resulted in a minimum recovery of moisture from the atmosphere, but reduced the mass gain during the weight measuring process, making it more stable. Each measurement was preceded by the cleaning of the crucible.

First the balance was tared, after which the crucible was weighted, after which a second tare was executed, followed by the weighting of the sample. Finally, a last tare was executed before starting the test. During the test the temperature profile illustrated in table 6 was used. After the weighting of the crucible, this was removed from the machine to be filled with polymer material. For each mixture, at

least 3 measurements were carried out, with a mass varying between 30 mg and 60 mg. This mass corresponded to 3 pellets in the crucible for most measurements.

Table 6 Temperature profile TGA.

	Mode	Temperature (°C)	Heating/cooling rate (K/min)	Time (h:mm)
1	Isothermal	20	/	0:05
2	Dynamic	800	10 (+)	1:18
3	Isothermal	800	/	0:10
4	Dynamic	25	20 (-)	0:38

Table 6 shows that the thermogravimetric analyser waits till the temperature in the heating chamber is 20°C, the machine starts when it's 5°C away from its temperature guide during the initiation phase. Once the machine starts there is a 5-minute isothermal phase to let the temperature stabilise within the heating chamber. This is then followed by a dynamic heating at a rate of 10 K/min until the temperature inside the heating chamber reaches 800°C. After which the analyser keeps this temperature during 10 minutes, to degrade a maximum of remaining matter. Finally, there is a dynamic cooling phase in which the temperature in the chamber is brought back down, close to the ambient temperature.

After the analysis, the remaining mass was calculated. This calculation took into consideration that the actual mass of PLA/HA at the start of the experiment was not the one measured by weighting. To obtain the actual mass of PLA/HA at the start of the experiment, the mass of the volatile components ("mass loss 1") has to be corrected from the total mass loss ("mass loss 2"). In this case equation 2 was used to determine the remaining mass (%). It is important to note that the remaining mass includes both the remaining mass of pure PLA and the remaining HA.

$$Equation\ 1: mass\ loss_{Calculated} = \frac{mass\ loss\ 2\ (\%)}{1 - mass\ loss\ 1\ (\%)} \quad (11)$$

$$Equation\ 2:\ m_{Remaining}\ (\%) = 1\ -\ mass\ loss_{Calculated} \quad (12)$$

To find the percentage of HA, the remaining mass of PLA extruded has to be subtracted from the remaining masses of all the PLA/HA mixtures.

3.2.2.2 Differential scanning calorimetry

The differential scanning calorimetry (DSC) was carried out with a Netzsch DSC 204 F1 (ESIReims, France), calibrated with Indium for a 10 K/min ramp speed and took place under atmospheric conditions. The PLE 005 as well as the extruded PLA/nHA (0%; 0,5%; 1%; 3% and 5%) composite granules, filaments and FDM printed samples were tested. The analysis consisted of two heating/cooling cycles from 25°C to 210°C with ramps of 10K/min to erase the thermal history. Sample preparation was the same as for the TGA measurements. After the preparation, a single polymer pellet was selected from the prepared batch for each measurement. The weight of this polymer pellet was around 15 mg for each measurement. For each sample an aluminium DSC pan and lid were prepared, the lid was carefully pierced with a needle. Before the DSC pan and pierced lid were sealed, their weight was measured after which a polymer pellet with a previously determined mass was inserted into the pan. In addition to the prepared DSC containers, a reference (empty) and an empty container

were also present in the carrousel used for the DSC analysis. These were used for the correction of the DSC analysis, to eliminate noise and drift in the measurement.

Table 7 summarises the temperature profile of the DSC analysis. The procedure was repeated until all samples were analysed. The first heating cycle consisted of erasing the temperature history of the sample. Data was only taken from the first cooling cycle and the second heating cycle and analysed with NETZSCH Proteus Thermal Analysis software.

Table 7 Temperature profile DSC analysis.

	Mode	Temperature (°C)	Heating/cooling rate (K/min)	Time (h:mm)
1	Isothermal	20	/	0:04
2	Dynamic	210	10 (+)	0:19
3	Isothermal	210	/	0:08
4	Dynamic	25	10 (-)	0:18
5	Isothermal	25	/	0:04
6	Dynamic	210	10 (+)	0:18
7	Isothermal	210	/	0:04
8	Dynamic	20	10 (-)	0:19
9	Isothermal	20	/	0:04

Following Fowlks and Narayan, the crystallinity of PLE 005 and the composites at different processing stages was determined with the following equation [195]:

$$X_c = \frac{\Delta H_m}{\Delta H_m^0 * \Phi_{PLA}} \qquad (13)\ [195]$$

With X_c the crystallinity, ΔH_m the melt enthalpy, ΔH_m^0 the theoretical melt enthalpy of 100% crystalline PLA (93 J/g) and Φ_{PLA} is the weight fraction of PLA in the composite. The weight fraction of PLA will be calculated with the theoretical values of HA.

3.2.2.3 Oscillatory rheology

Plate-plate oscillatory rheology tests were carried out with a TA instruments AR 2000 EX (ESIReims, France). Only the extruded PLA/nHA (0%; 0,5%; 1%; 3% and 5%) composite granules were tested. All tests were carried out under atmospheric conditions. During the tests, the storage modulus (G') and the loss modulus (G") were measured, from which the complex viscosity was then calculated. The test samples were discs previously created with the heated hydraulic press. Gerard and Budtova showed the importance of a drying prior to testing [196]. With the appearance of a bubble effect at low frequencies in non-dried samples. This bubble effect can be linked to the degassing of water which results in a lower complex viscosity. In dried samples this bubble effect did not appear as most of the water had already been removed from the sample during the drying process. Hence why before testing the discs with the rheometer, they were heated to 70°C in a desiccator apparatus and kept there for at least 15 minutes. During this time the rheometer was preheated to 175°C. When the rheometer was at the desired temperature, the gap between the two plates was set to zero with the build in "Gap Zero" command. After this the distance between the two plates was increased to 3 mm to allow the discs to be inserted between the two plates of the rheometer. With the insertion of the discs between the plates, a timer was started. Immediately after insertion, the distance between the plates was

decreased to 2 mm. Two minutes later the surplus material that had built up around the edges of the plate due to the reduced height was removed. Three minutes after the insertion, the distance between the plates was further reduced to 1.8 mm, followed by the removal of the excess material. Six minutes after the insertion the rheological tests were started. The timing of the different steps was important because the time sweeps showed a slight decrease. Thus, to compare the results, the measurements have to be launched at the same time and after undergoing the same procedure.

Two different tests were carried out with the plate-plate oscillatory rheometer. The first test consisted of a time sweep, which measured the moduli (G' and G") at a constant frequency during a specified amount of time, this to determine whether the material would last long enough under the test conditions without degrading. The second test was a frequency sweep, during which the complex viscosity was measured at multiple frequencies to determine the rheological behaviour of the tested material. For the time sweep, the time was set to 1 hour at a strain percentage of 1%, a frequency of 1 Hz and a temperature of 175°C. The frequency sweep was carried out at a temperature of 175°C and a strain percentage of 1% with a frequency that decreased from 100 to 0.1 Hz. No strain sweep was carried out to find the maximum strain before materials leave elastic behaviour, since this measure was already carried out by several authors and former PhD students.

After the tests the results were analysed with TA Universal Analysis software. Additionally, a Carreau-Yasuda model was used to model the viscosity of the PLA/HA at different shear rates [190]. The Carreau-Yassuda model could only be used after applying the Cox-Merz rule, which gives the equivalence between the shear rate and the frequency of the Rheometer [190] [197]. This was necessary, since the results from the rheometer were in function of the frequency and the Carreau-Yasuda model uses the shear rate [190]. The Carreau-Yasuda model is given by the following equation [190].

$$\eta(\dot{\gamma}) = \eta_0[1 + (\lambda\dot{\gamma})^a]^{\frac{n-1}{a}} \qquad (14)\ [190]$$

With η the viscosity in Pa.s, η_0 the viscosity at zero shear in Pa.s, λ the relaxation time in s (corresponding to the onset of the fluidification), a the Yasuda index (which determines the curve of the fluidification transition) and n the index of the power law. Le Marec et al. Analysed the impact of the molecular mass on the viscosity of PLA and found that at lower molecular masses the viscosity decreases [198]. They used a power law and the Carreay-Yasuda model to characterize the viscosity [190] [198]. The following equation contains the power law [198].

$$\eta = K.|\dot{\gamma}|^{n-1} \quad (15)\ [198]$$

With η the viscosity in Pa.s,
K the consistency in Pa.s^n
and n the index of the power law.

3.2.2.4 Tensile tests

The Young modulus and the ultimate strength of FDM printed and injection moulded 5A-type tensile test specimen from ISO 527-2 were determined using an Instron 33R4204 (ESIReims, France) [192]. The tensile test conditions used were: a cross head speed of 5 mm/s and a 1 kN charge. All tests were

carried out under ambient conditions. For each nanocomposite, there were 7 different conditions of FDM printed tensile specimen and one type of injection moulded specimen. A minimum of 5 measurements was carried out for each type of tensile specimen to ensure repeatability. The injection moulded tensile specimens received a thermal pre-treatment. The specimens were crystallised by keeping them at 70°C for 24 hours prior to testing.

3.2.2.5 Dynamic mechanical analysis

Dynamic mechanical analysis was carried out with a TA instruments Q800 (ESIReims, France), the temperature varied from 30 to 140°C, with a 3 K/min heating ramp. The strain was kept constant at 0.1% and the frequency was kept constant at 1Hz. Test samples for the dynamic mechanical analysis were created using two methods. A first batch of samples was created with fused deposition modelling (FDM) and a second batch of samples was created with compression moulding. For the FDM printing process, the previously extruded PLA/nHA composite filaments were used. For each composite, the printing temperature was set to 215°C and the printing speed to 75 mm/s with a 90°/0° alternating printing angle; 5 test samples were printed for each composite. The printed test samples were stored in ambient conditions for a week, after which the samples were tested. Unlike the printed samples, the compressed samples were stored under vacuum to prevent moisture absorption and before testing the pressed samples were annealed at 70°C for 15 minutes.

A minimum of three tests was carried out for the printed and compressed samples. Each of the three tests took place on the same day, this to reduce the influence of the ambient conditions on the repeatability of the test results. The DMA took place in a non-climatized room, making it susceptible to the changing environmental conditions (humidity and temperature). After testing, the results were analysed with TA Universal software.

3.2.2.1 Wide angle X-ray diffraction on powder analysis

The wide angle X-ray diffraction on powder (WAXD-P) analysis were carried out with a D8 Advance Bruker AXS (LISM, Reims, France), at room temperature and under Bragg conditions. The analysis took place in the 2°-60° interval, with steps of 0.06° (2 seconds per step) and a Cu K-α X-ray source was used at 40 mA and 40 kV. Powders were required for the analysis, therefore a Retsch ZM1000 (ESIReims, France) was used to turn extruded PLA, PLA/HA 1% (granules and FDM specimens) and PLA/HA 5% (granules and FDM specimens) into usable powders. The aqueous hydroxyapatite paste (30 wt.%) was air dried to obtain a powder.

After the analysis, the Bragg and Scherrer formulas were used to determine the interplanar distance and the mean particle size of hydroxyapatite and PLA crystals respectively [199] [200].

$$\text{Bragg: } n\,\lambda = 2\,d\,\sin\theta \qquad (16)$$

With n (1), a positive integer that denotes the order of the diffraction band;
λ (nm), the X-ray wavelength;
d_{hkl} (nm), the interplanar distance;
and ϑ (°), the Bragg angle.

$$\text{Scherrer: } \tau = \frac{K\,\lambda}{\beta\,\cos\theta} \qquad (17)$$

With τ (nm), the mean particle size of the crystals;
K (0.9), the dimensionless shape factor;
λ (nm), the X-ray wavelength;
β (rad), the width of the maximum intensity peak at half of its intensity;
and ϑ (°), the Bragg angle.

3.2.2.7 Transmission electron microscopy

Transmission electron microscopy (TEM) tests were conducted with a Philips CM200 (University of Haute-Alsace, Haute-Alsace) with an acceleration voltage of 200 kV. The TEM samples were prepared by ultramicrotomy with a Leica EM UC7 (University of Haute-Alsace, Haute-Alsace) at room temperature and each sample had a thickness of approximately 90 nm. Per sample, 5 different zones were observed, each zone was observed with 5 different magnitudes for a total of 25 photos per sample.

3.2.2.8 Permeability tests

WVTR tests were conducted with a Mocon Permatron-W Model 3/31 water vapour permeability (ESIReims, France). OTR tests were conducted with a Mocon Ox-Tran SH1 (VerpakkingsCentrum, Belgium). The tests were conducted at a temperature of 23°C and a RH of 50%. All tests were carried out in duplicate, before testing, the samples were conditioned at 23°C and 50% RH. The thickness of the samples was measured with an Electronic Digital Micrometer and a MTS Adamel Lhomargie Mi20.

4 Results and discussion

4.1 Sample preparation

4.1.1 Twin-screw extrusion

4.1.1.1 Extrusion Masterbatch

The extrusion consisted of the preparation of the PLA/HA (10%) master batch, which would be used to prepare all other mixtures. During the extrusion, the granules feed, screw speed was set to 6%, which corresponded to a PLA flow of 1,5 kg/h. In addition, the co-rotating screws were rotating at 300 rpm, with a couple that fluctuated between 49% and 51% (~50%) and a pressure fluctuating between 13 bar and 17 bar (~15 bar). The following table contains the temperature setting of each zone during the extrusion process. Note that these are still only guidelines and not actual material temperatures.

Table 8 Temperature profile extruder.

Temperature profile								
Zone	1	2	3	4	5	6	7	8
Temperature (°C)	180	175	170	165	165	170	180	180

PLA was put into the granules section of the extruder. Once the extrusion process stabilised, Hydroxyapatite paste was added. HA paste was added in heating zone 3 of the extruder, which was left open during this extrusion. Every 30 seconds approximately 5 g of HA paste was added (one fifth of a syringe), this resulted in an increased output flow (1,68 kg/h). Due to the temperature of heating zone 3, most of the water in the paste evaporated immediately. To remove a maximum of water during the extrusion process, heating zone 6 was also left open. However, because zone 3 and zone 6 were left open, the temperature fluctuated greatly in these and neighbouring zones.

With the addition of the HA paste, the properties of the filament changed. Visually the filament changed from transparent to opaque and displayed a milky white colour. An important change was the increase of the Barus effect, the filament expansion upon exiting the extruder increased dramatically, making it impossible to obtain a filament that could be transported to the granulator. Therefor the material was collected at the end of the extruder, which resulted in huge lumps of material. In total 3 kg of material was collected.

After extrusion 1 the obtained lumps of PLA/HA (10%) master batch were dried at 60°C in the presence of silica crystals during a week before being crushed with a CMB Type ML 16 crusher to obtain small enough chunks. This was necessary, because bigger pieces of material cannot pass through the extruder. However, at the end of the process one of the knives in the crusher detached from its support, resulting in the destruction of the machine and pieces of metal mixed in with the crushed material. Before the usage of the obtained material, it was necessary to remove the metal knife fragments. This was achieved by washing the crushed material in water, followed by a passing with multiple magnets. Once the water was drained the pellets were spread out in thin layers and a magnet was rolled over the material to remove any remaining knife fragments. Finally, the obtained pellets were dried at 60°C in the presence of silica crystals until the next extrusions.

4.1.1.2 Extrusion nHA/PLA mixtures

The extrusion consisted of the preparation of the mixtures used for the creation of all the test specimen. PLA and PLA/HA (10%) pellets were mixed before the extrusion to obtain PLA/HA 0%; 0,5%; 1%; 3% and 5%. For each mixture, a total of 3 kg was prepared for extrusion. During the extrusions, the screw speed was fluctuating around 300 rpm. The temperature profile (Setting and Measured) of each extrusion and the couple and the pressure during each extrusion are given in table 9. It is important to note that zone 3 and 6 were closed during these extrusions, resulting in a much more stable temperature profile.

Table 9 Parameters extrusion mixtures.

nHA (%)	Temperature (°C) | Zones	1	2	3	4	5	6	7	8	Couple (%)	Pressure (bar)
0%	Setting	180	175	170	170	170	147	162	170	~51%	19-20
	Measured	180	176	170	170	170	142	175	170		
0,50%	Setting	180	175	170	170	170	130	162	170	~56%	~20
	Measured	180	175	170	170	170	143	178	171		
1%	Setting	180	175	170	170	170	150	162	170	~55%	17-19
	Measured	180	174	170	169	169	142	170	169		
3%	Setting	180	175	170	170	170	130	162	165	~52%	19-23
	Measured	180	175	170	169	170	123	172	165		
5%	Setting	180	175	170	170	170	130	162	165	~46%	~21
	Measured	180	175	170	170	170	130	173	165		

The temperature settings during each extrusion vary for zone 6 and 8. Adjustments were made to the settings at the beginning of the extrusion, this to facilitate the transport of the filament. Once the filament was stable, the temperature settings were kept the same. The varying temperature profile at which the filament was stable can be explained by the varying circumstances in the production hall. Temperature and humidity were not controlled during the extrusion, this directly affected the state of the pellets at the beginning of the extruder as well as the cooling rate at the end of the extruder. Another explanation for the varying temperature profile can be found in the variation of the formulation, which can modify the viscosity. To readjust the viscosity, a temperature variation is needed. Besides the varying conditions in the hall and the variations in viscosity, there are other parameters which can influence the temperature profile of the extrusion, such as the morphology of the material. There was also a slight difference between the temperature settings and the measured temperatures. However, this difference was caused by the extruder's captors which recorded the temperature. Based on the reading of the captors, the heaters or the water based cooling system would be working. The temperature variation was less important during the extrusions of the mixtures since zones 3 and 6 were closed.

Another thing that can be noted when looking at table 9 is the change in couple. The couple appears to increase between the 0% and the 0,5% mixture and then decrease for all the following mixtures. During the extrusion of the mixtures the granules feed screw speed was set to 7%. A measurement of the input and output flow was conducted during the first extrusion of the mixtures. The input flow was found to be 1,881 kg/h whereas the output flow was 1,9413 kg/h. The small difference between the input and the output flow was contributed to the irregular shape of the pellets resulting in a varying input flow. However, during the last extrusion (5%), the input flow was measured again and it was found to be 1,440 kg/h, which is much lower than the input flow measured during the first extrusion. An explanation for the reduced flow can be found in the irregularity of the masterbatch pellets, these pellets were mixed in with more regular PLA pellets in increasing ratios, maxing out at 50/50 for the 5% mixture. The decrease in viscosity can thus be explained by the decrease of the flow, but a decrease

of the viscosity when adding nano hydroxyapatite to PLA can also be a contributing factor. Rheological analysis of the obtained mixtures will show the evolution of the viscosity in function of the percentage of nano hydroxyapatite and could thus confirm whether the nHA rods have a thinning effect. The final column of table 9 shows the pressure in the extruder during each extrusion. This pressure varied during the extrusions and seems to increase and decrease at random for increasing percentages of HA.

Unlike during the extrusion of the masterbatch, there were no problems with the filament during the extrusion of the mixtures and the filament could be transported through the water bath past the rolling carpet into the Scamia 960001 GR granulator. The obtained mass of each mixture is shown in table 10. There were no problems during the extrusion of the following mixtures: 0%; 0,5%; 3% and 5%. However, the extrusion of the 1% mixture had to be stopped halfway through, due to the rolling carpet detaching from its support. A temporary repair was carried out and the extrusion was continued, the carpet speed varied greatly afterwards, resulting in a very irregular filament diameter. Eventually the temporary repair broke and only 2,136 kg of PLA/HA (1%) was obtained after the extrusion. Regardless of the problems encountered during the different extrusions, enough material of each mixture was obtained for the analysis and the fused deposition modelling.

Table 10 Obtained mass mixtures after each extrusion.

PLA/HA	Obtained material (kg)
0%	2,334
0,5%	2,642
1%	2,136
3%	2,740
5%	2,602

4.1.2 Single-screw extrusion

Table 11 shows the temperature settings of the extruder. The extrusion temperatures of the three zones were the same for the PLA/HA nanocomposites. The pure PLA was extruded at lower temperatures, this to avoid degradation. For the composites, the temperature was increased to ensure the granules melted correctly. Due to the short extruder, it was presumed that there was not enough time to correctly melt the granules at lower temperatures, since a higher crystallinity was suspected for the granules.

Table 11 Temperatures single-screw extrusion mixtures.

Extrusion (20Hz)	Entrance (°C)	Middle (°C)	Exit (°C)
PLA extruded	185	175	175
PLA/HA 0,5%	195	185	180
PLA/HA 1%	195	185	180
PLA/HA 3%	195	185	180
PLA/HA 5%	195	185	180

In table 12 the diameter of the obtained filament, the total extruded mass, the total extrusion time, the pulling speed and the mass flow are shown. The output of the extruder varied across the different extrusions. Each extrusion had the same screw speed, yet the addition of 0.5% of HA resulted in the

highest output flow, while an addition of 3% HA resulted in a very low output flow. This could indicate that HA has a thinning effect when added in small quantities, something that was already suggested after the twin-screw extrusions. However, it seems like there is an upper concentration limit after which the thinning effect disappears, given the lower output flows for 1%, 3% and 5%. The evolution of this thinning effect could be verified with a rheological analysis. Every filament apart from PLA/HA 3% had an average diameter of 1.6 mm, however, there is a lot of variation on this diameter, while PLA/HA 3% had a rather stable diameter of 1.5 mm. This diameter variation was due to the fact that the environmental parameters of the extrusion were non-controllable. For the PLA/HA 5% the pulling speed had to be lowered significantly to obtain a stable diameter within the acceptable interval, which can also be linked to the non-controllable environmental parameters.

Table 12 Results single-screw extrusion.

Extrusion (20Hz)	Diameter (mm)	Time (min)	Mass (g)	Mass flow (g/min)
PLA extruded	1,6 ± 0,10	45	300	6,7
PLA/HA 0,5%	1,6 ± 0,10	60	500	8,3
PLA/HA 1%	1,6 ± 0,10	60	430	7,2
PLA/HA 3%	1,5 ± 0,02	80	425	5,3
PLA/HA 5%	1,6 ± 0,10	45	350	7,8

4.1.3 Fused deposition modelling

The temperature levels of the Doehlert matrix were changed to allow inter nanocomposite comparison. Initially the lowest temperature was 190°C, however, it was found that at 190°C the printing process was impossible for nanocomposites with a HA concentration of 1% due to a lack of composite material exiting from the print nozzle. Therefore, the temperature levels were changed accordingly and the lowest temperature was increased from 190°C to 210°C. The highest level did not change, since at higher temperatures the risk of degradation was too high, while the intermediate level was adjusted from 215°C to 225°C to ensure the principle of uniform space-filling.

The FDM process resulted in varying finishes depending on the points (conditions) of the Doehlert matrix. Additionally, the finish at different conditions was dependent on the percentage of HA added to PLA. The best quality was found in condition 5 for PLA pure, in condition 7 for PLA/nHA 0.5%, in condition 4 for PLA/nHA 1%, in condition 7 for PLA/nHA 3%, and in condition 4 for PLA/nHA 5%. With each of the conditions referring to the printing speed and printing temperature coordinates discussed earlier. The quality of the printed tensile test specimen was determined by examining the surface roughness, the contours and the filaments in the interior of the sample. A recurring problem was the increased roughness of the test section of the tensile test samples. This was due to the reduced width of the samples at this point, which resulted in a rapid side to side movement when printing in the direction of the width. The rapid side to side movement resulted in the displacement of filaments in the layer underneath, which resulted in badly positioned filaments which in turn would lead to the displacement of all the filaments deposited on top of them and thus in surface roughness. The problem became more pronounced when the printing speed increased, as this would lead to a more violent side to side motion in the tensile section. High speeds also resulted in less accurate contours, something that was especially visible in the transition from the clamping section to the tensile test section. In this transition, the width gradually reduced, leading to partial detachment of the contours

at high speeds for some composites. Despite the effect of high speeds being more visible, it was also visible in the other sections, usually in the form of a wave-like pattern. Lastly, the surface roughness and the contour accuracy was sometimes found to be very good while the filaments on the interior of the sample had clearly been displaced. This was easier to determine for the pure PLA and composites with low percentages of HA, due to the increasingly more prominent milky white colour of the composites with the addition of more HA. The following pictures illustrate the surface roughness, the lack of accuracy of the contours and the filaments on the interior.

4.1.4 Injection moulding

Multiple parameters were adjustable during the injection moulding: the injection time, the pressure, the pressure during the second pressing cycle, the material infeed, the mould temperature, etc. For each formulation, the parameters were changed to obtain the samples with minimum shrink upon cooling. Table 13 gives the heating temperatures of the heating zones and the pressure used for injection of the different formulations.

Table 13 Temperature and pressure settings injection moulding process.

	Temperature (°C)			Pressure (Bar)	
Injection Moulding	Zone 1	Zone 2	Zone 3	1	2
PLA	190	190	190	99	20
PLA/nHA 0,5%	195	195	195	99	20
PLA/nHA 1%	200	200	200	99	20
PLA/nHA 3%	195	195	195	99	20
PLA/nHA 5%	195	195	195	99	20

4.1.5 Heated hydraulic press

4.1.5.1 Carver press

The DMA and oscillatory rheology samples created with the carver press both showed similar faults. The usage of pellets for the filling of the moulds sometimes resulted in airgaps when the filled moulds were put into the press. In turn these airgaps would sometimes result in bubbles or badly formed areas in the test samples. Additionally, the compression moulded samples were also susceptible to shrinking. Before the usage of the samples in DMA and rheology tests, they were checked for internal bubbles and any missing material or excessive shrinking. Samples containing any of these defects were not used and if necessary additional samples were prepared.

4.1.5.2 Samples permeability tests

The films created for the permeability tests did not have a constant thickness. Instead, the thickness would decrease in one direction. The cause of this decrease was linked to the press, which did not have levelled pressing plates. In turn this would result in an evolution of the thickness after pressing, since the plates would come into contact earlier on once side. Effectively forcing the polymer material to move towards one side. The surface of the films was very dependent on the thin aluminium sheets on the outside of the mall, as the polymer films would copy each crease and indent and would absorb all impurities. Finally, due to the usage of pellets, the films sometimes contained air bubbles. During the permeability tests, a test surface without air bubbles was chosen.

4.2 Thermogravimetric analysis

4.2.1 Introduction

The goal of the thermogravimetric analysis is firstly to verify the remaining mass after the degradation of PLA, secondly to verify the concentration of HA in the nanocomposites, and thirdly to compare the degradations of each analysed material. Additionally, the results of the TGA will be used to help determine the maximum printing temperature of the FDM process.

4.2.2 Results

4.2.2.1 Granules

The results of the thermogravimetric analysis of the granules will be discussed in this section. First each mixture will be discussed separately, then the averages of each mixture will be compared with each other. The following data was obtained from each analysis: The mass change between the room temperature and 200°C; The mass change between 200°C and 700°C; The onset and the end of the degradation between 200°C and 700°C; and the degradation peak along with its mass loss (%/min). The mass change between the starting temperature and 200°C corresponds to the removal of water and the partial removal of other volatile components such as the lactic acid monomer. Feng et al. found that the temperature interval, in which the lactic acid monomer is removed from PLLA for samples dried under vacuum at 70°C for 12 hours, is 100-250°C [201]. The mass change between 200°C and 700°C corresponds to the main degradation of material during the analysis and the removal of the remaining volatile compounds. The degradation peak temperature is the temperature corresponding to the peak of the first derivative of the curve. An example of all these results is given in figure 17.

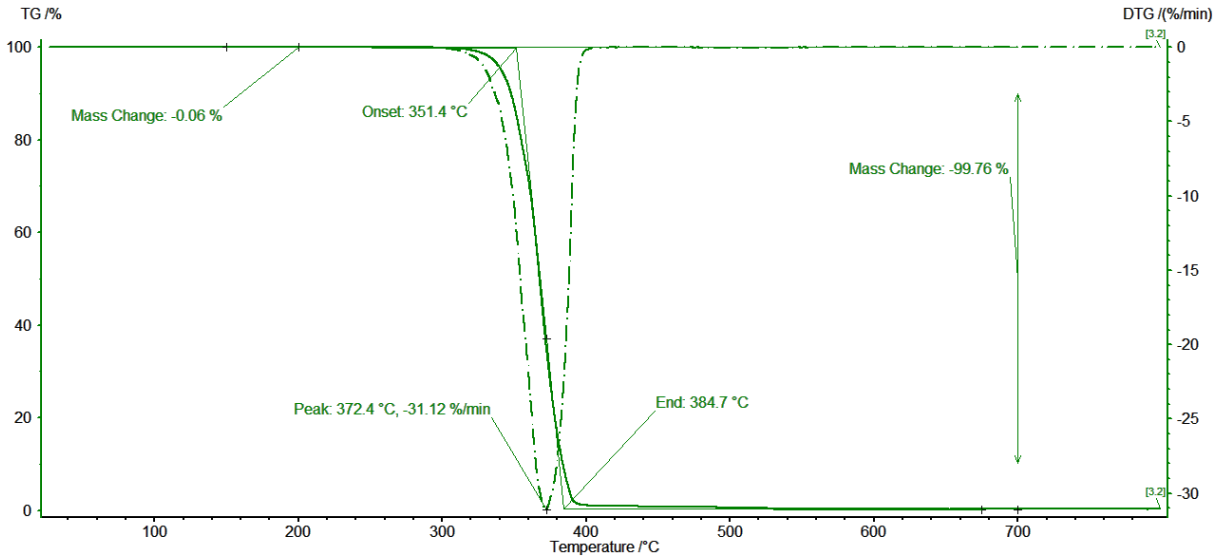

Figure 17 Thermogravimetric analysis PLE 005.

In table 14, the results of the thermogravimetric analysis of PLE 005 are given, the standard deviation of the remaining mass is very high. An explanation for the high standard deviation can be found in the amount of mass used. The starting mass of the sample is between 30 mg and 60 mg, which results in a remaining mass in the µg range and thus near the limit of the sensitivity of the used balance. Hence why minor variations caused by a too large time interval between consecutive mass measurements at the start of the experiment, result in large deviations of the remaining mass. Prime examples of the effect on the remaining mass are measurement 4 and 6. Measurement 4 has a negative remaining mass, which is impossible; and measurement 6 has a too high remaining mass. However, table 14

shows that the degradation profile of the PLE 005 is very similar for each measurement, indicating that the degradation profile is very repeatable.

Table 14 Thermogravimetric analysis PLE 005.

	Mass loss				Mass loss per minute (%/min)	T (°C)			Temperature range
PLE 005	1	2	Calculated	Remaining mass	Peak	Onset	Peak	Endset	Degradation (°C)
4	0,09%	100,15%	100,24%	-0,24%	31,96	351,7	372,2	384,8	33,1
5	0,02%	99,82%	99,84%	0,16%	31,01	351,6	372,3	385,3	33,7
6	0,03%	99,02%	99,05%	0,95%	31,00	351,5	373,7	385,1	33,6
7	0,04%	99,82%	99,86%	0,14%	31,15	351,4	372,2	385,0	33,6
Average (4-7)	0,05%	99,70%	99,75%	0,25%	31,28	351,6	372,6	385,1	33,5
STDEV	0,03%	0,48%	0,50%	0,50%	0,46	0,1	0,7	0,2	0,3

For the extruded PLA, the same problem occurred and the measurements were repeated. The first measurements resulted in a remaining mass of 0.10±0.25%, which is an improvement compared to the standard deviations found for PLE, but still a rather high standard deviation compared to the value of the average. The results of the repetition are shown in table 15. For the extruded PLA, the additional testing, with reduced time between consecutive weighting steps, resulted in a much smaller standard deviation. The average remaining mass was found to be 0.17%, this result will be used to calculate the hydroxyapatite content for all the mixtures. As with the PLE 005, the degradation profile of the extruded PLA was very repeatable, given that all the standard deviations are small.

Table 15 Thermogravimetric analysis PLA extruded (Continued).

	Mass loss				Mass loss per minute (%/min)	T (°C)			Temperature range
PLA extruded	1	2	Calculated	Remaining mass	Peak	Onset	Peak	Endset	Degradation (°C)
4	0,02%	99,82%	99,84%	0,16%	30,93	349,3	372,8	383,7	34,4
5	0,04%	99,78%	99,82%	0,18%	30,97	349,6	372,3	383,8	34,2
6	0,00%	99,84%	99,84%	0,16%	30,75	349,9	372,0	383,6	33,7
7	0,00%	99,84%	99,84%	0,16%	30,91	349,6	372,7	383,5	33,9
Average (4-7)	0,02%	99,82%	99,83%	0,17%	30,89	349,6	372,5	383,7	34,1
STDEV	0,02%	0,03%	0,01%	0,01%	0,11	0,2	0,4	0,2	0,3

Table 16 shows the results of the thermogravimetric analysis of PLA/HA 0.5%. As with PLE 005 and the extruded PLA, this measurement was also executed with too much time between the measurement of the crucible and the sample weight. However, the standard deviation is low enough. Additionally, the average remaining mass was found to be 0.62%. By subtracting 0.17%, the average remaining mass of the extruded PLA, from the average remaining mass, the hydroxyapatite content was found to be 0.45%.

Table 16 Thermogravimetric analysis PLA/HA 0.5%.

	Mass loss				Mass loss per minute (%/min)	T (°C)			Temperature range
PLA/HA 0,5%	1	2	Calculated	Remaining mass	Peak	Onset	Peak	Endset	Degradation (°C)
1	0,01%	99,38%	99,39%	0,61%	30,69	348,1	373,7	386,8	38,7
2	0,05%	99,37%	99,42%	0,58%	32,51	349,4	370,8	383,9	34,5
3	0,01%	99,33%	99,34%	0,66%	33,94	349,0	370,2	382,6	33,6
Average	0,02%	99,36%	99,38%	0,62%	32,38	348,8	371,6	384,4	35,6
STDEV	0,02%	0,03%	0,04%	0,04%	1,63	0,7	1,9	2,2	2,7

In table 17 the results of the thermogravimetric analysis of PLA/HA 1% are shown. For these measurements, the time in between the weighting of the crucible and the sample mass was reduced significantly, resulting in a much more accurate measurement. The remaining mass was found to be 1.08%, by subtracting the remaining mass of the extruded PLA, the percentage of HA was found to be 0.91% on average.

Table 17 Thermogravimetric analysis PLA/HA 1%.

	Mass loss (%)				Mass loss per minute (%/min)	T (°C)			Temperature range
PLA/HA 0,1%	1	2	Calculated	Remaining mass	Peak	Onset	Peak	Endset	Degradation (°C)
5	0,01%	98,85%	98,86%	1,14%	31,86	347,8	372,0	384,6	36,8
6	0,03%	98,89%	98,92%	1,08%	31,52	347,7	372,6	385,2	37,5
7	0,05%	98,92%	98,97%	1,03%	31,91	348,0	372,3	385,3	37,3
Average	0,03%	98,89%	98,92%	1,08%	31,76	347,8	372,3	385,0	37,2
STDEV	0,02%	0,04%	0,05%	0,05%	0,21	0,2	0,3	0,4	0,4

In table 18 the results of the thermogravimetric analysis of PLA/HA 3% are shown. The average mass of HA was found to be 3.12% and thus corresponds well to the targeted 3%.

Table 18 Thermogravimetric analysis PLA/HA 3%.

	Mass loss				Mass loss per minute (%/min)	T (°C)			Temperature range
PLA/HA 3%	1	2	Calculated	Remaining mass	Peak	Onset	Peak	Endset	Degradation (°C)
1	0,09%	96,69%	96,78%	3,22%	32,28	346,8	369,8	382,6	35,8
2	0,07%	96,69%	96,76%	3,24%	32,82	346,4	368,3	381,9	35,5
3	0,11%	96,50%	96,61%	3,39%	31,80	347,0	369,9	383,2	36,2
Average	0,09%	96,63%	96,71%	3,29%	32,30	346,7	369,3	382,6	35,8
STDEV	0,02%	0,11%	0,09%	0,09%	0,51	0,3	0,9	0,7	0,4

Table 19 shows the results of the thermogravimetric analysis of PLA/HA 5%. The average mass of HA was found to be 4.99% after the subtraction of the remaining mass of the extruded PLA.

Table 19 Thermogravimetric analysis PLA/HA 5%.

	Mass loss				Mass loss per minute (%/min)	T (°C)			Temperature range
PLA/HA 5%	1	2	Calculated	Remaining mass	Peak	Onset	Peak	Endset	Degradation (°C)
1	0,08%	94,78%	94,86%	5,14%	30,66	344,7	371,0	383,5	38,8
2	0,14%	94,63%	94,76%	5,24%	30,74	344,6	372,0	384,3	39,7
3	0,15%	94,77%	94,91%	5,09%	30,61	344,1	372,5	385,0	40,9
Average	0,12%	94,73%	94,84%	5,16%	30,67	344,5	371,8	384,3	39,8
STDEV	0,04%	0,08%	0,08%	0,08%	0,07	0,3	0,8	0,8	1,1

The onset, peak and end temperature of the degradation are shown in figure 18, figure 19 and figure 20 and table 20. Figure 18 shows that the degradation of PLA starts at lower temperatures when PLA is extruded and when more HA is added. Once extruded, the temperature at which the degradation starts, lowers with the addition of HA. The catalyst effect of HA on the degradation onset appears to be linear up to the addition of 1% HA, after which the onset temperature decreases less. However, the standard deviation of the onset is very high for the 0.5% composite, especially when compared to the other composites. The decrease in onset temperatures increases again when 5% of HA is added. It can thus be concluded that PLA becomes more susceptible to degradation at lower temperatures with the addition of HA.

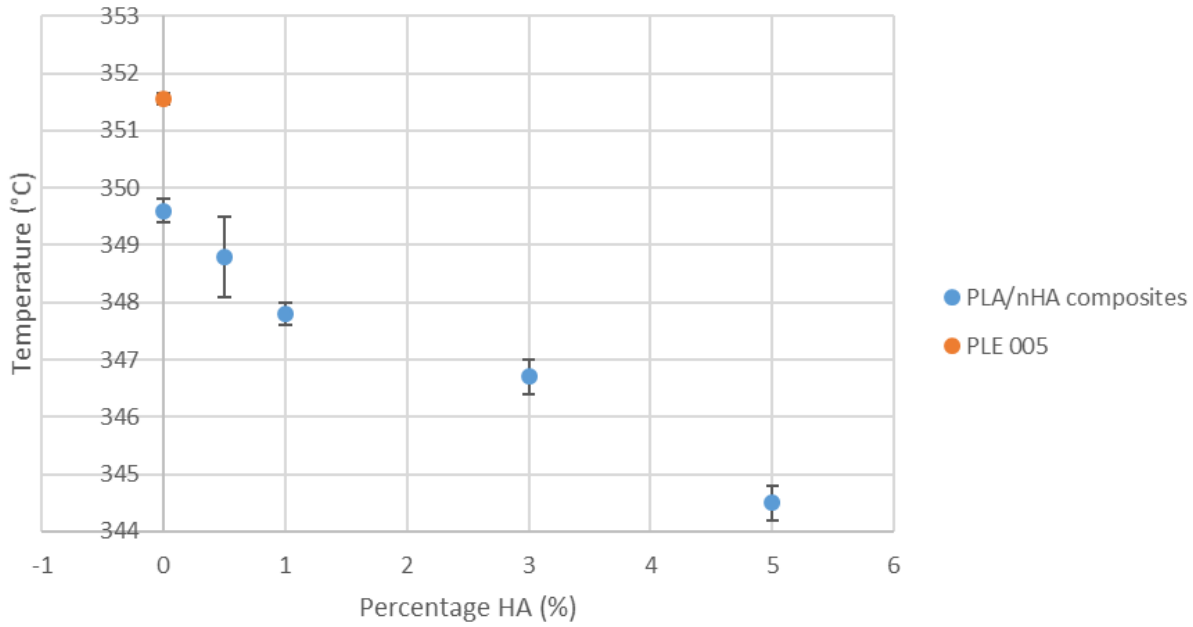

Figure 18 The degradation onset of PLE 005 and PLA/nHA nanocomposites plotted against the HA content.

In figure 19, the temperatures for which the degradation is maximal are shown. The temperature at which maximum degradation occurs all fall in the same interval apart from when 3% of HA is added, for which the temperature decreases. Note that the standard deviation of the 0.5% composite is again, much bigger than the others. Especially the overlap between PLE 005 and the extruded PLA is important. Given the earlier start of the degradation of PLA with the addition of HA, the maximum degradation speed does not appear to be affected, apart from when 3% of HA is added.

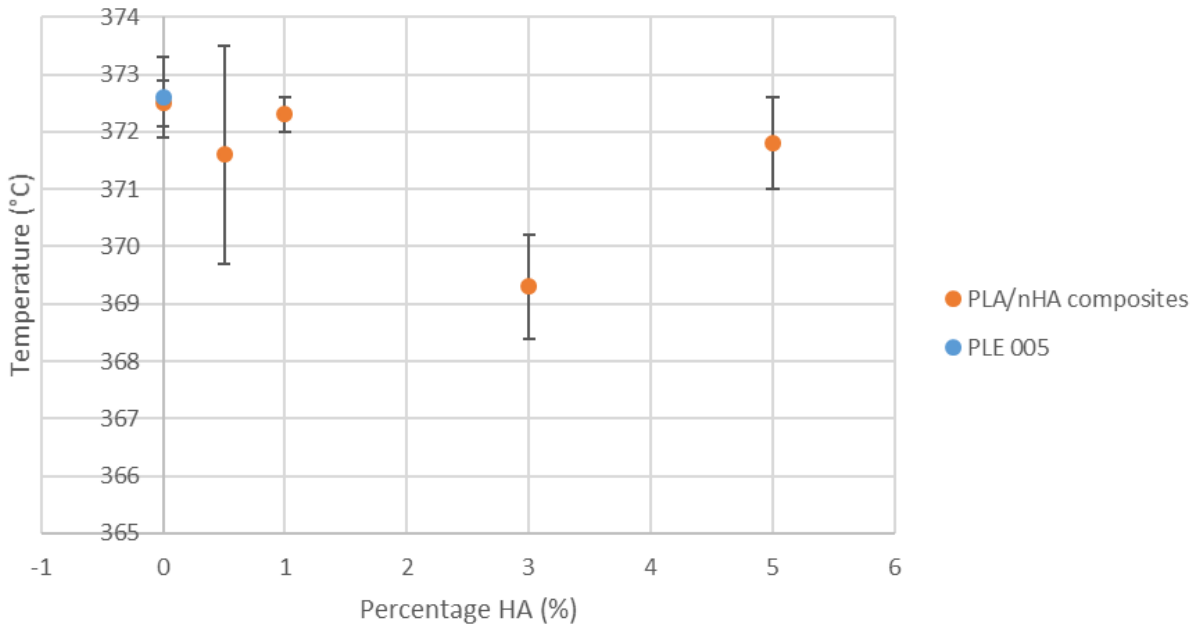

Figure 19 Temperature at which the maximum degradation speed occurs plotted against the HA content for the formulations.

Figure 20 shows the temperatures at which the degradation end in function of the added percentage of HA. The PLE 005 has the highest temperature, while the 3% composite has the lowest temperature. In this case, the 0.5%, 3% and 5% composite have standard deviations that are much higher than the other composites. The end of the degradation increases from the extruded PLA up to the addition of

1% of HA. After which, the degradation ends at a much lower temperature. The addition of 5% HA results in a higher temperature than the 3% composite. Additionally, the standard deviation of the 5% composite is high and there is an overlap between the temperature intervals of the extruded PLA and the 5% composite. On average degradation ends earlier for the extruded PLA and the HA composites when compared to PLE 005. This indicates that PLA does not hinder the degradation in its final stages.

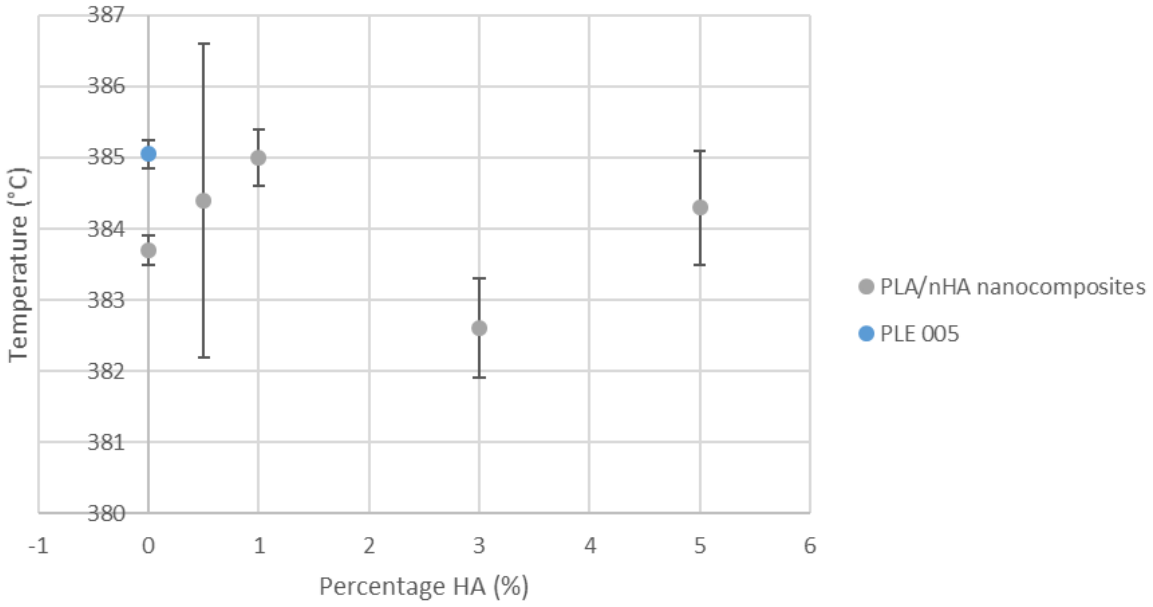

Figure 20 Temperature at which the degradation ends plotted against the HA content.

Table 20 shows that PLE 005 has the smallest temperature in which degradation occurs, followed by the extruded PLA. The temperature range in which degradation occurs increases with the addition of more HA, apart from the 3% composite for which the temperature range is smaller than that of the 1% composite. On average, the temperature range of the HA composites is larger than that of the PLE 005 and the extruded PLA. This could mean that the addition of HA results in a slower degradation by limited mobility.

Table 20 Summary temperatures thermogravimetric analysis.

	T (°C)			Temperature range
Averages	Onset	Peak	Endset	Degradation (°C)
PLE 005	351,6 ± 0,1	372,6 ± 0,7	385,1 ± 0,2	33,5 ± 0,3
PLA extruded	349,6 ± 0,2	372,5 ± 0,4	383,7 ± 0,2	34,1 ± 0,3
PLA/HA 0,5%	348,8 ± 0,7	371,6 ± 1,9	384,4 ± 2,2	35,6 ± 2,7
PLA/HA 1%	347,8 ± 0,2	372,3 ± 0,3	385,0 ± 0,4	37,2 ± 0,4
PLA/HA 3%	346,7 ± 0,3	369,3 ± 0,9	382,6 ± 0,7	35,8 ± 0,4
PLA/HA 5%	344,5 ± 0,3	371,8 ± 0,8	384,3 ± 0,8	39,8 ± 1,1

Table 21 shows that the remaining mass follows the expected trend, namely an increased percentage with the addition of more HA. Additionally, the found percentages of HA are close to the target concentrations of 0%, 0.5%, 1%, 3% and 5%. The maximum mass loss per minute is the highest for the 0.5% composite, followed by the 3% composite. The lowest maximum mass loss per minute was found for the 5% composite, closely followed by the extruded PLA. PLE 005 and the 1% composite both have similar maximum mass losses, in between the highest and lowest maximum mass loss. The temperature range does not explain the high maximum mass loss of the 0.5% and 3% composites. A

possible explanation can be found in the position of their peak, which is more centred in the temperature range. Therefore there is more polymer material available for degradation. Additionally, the higher temperature ranges, with a slower degradation kinetic due to the addition of filler, could be the result of a chain movement limiting caused by the HA filler.

Table 21 Summary mass loss thermogravimetric analysis mixtures.

Summary	Mass		Mass loss per minute (%/min)
Averages	Remaining mass (%)	HA (%)	Peak
PLE 005	0,25% ± 0,50%	0%	31,28 ± 0,46
PLA 0%	0,17% ± 0,01%	0%	30,89 ± 0,11
PLA 0,5%	0,62% ± 0,04%	0,45% ± 0,05%	32,38 ± 1,63
PLA 1%	1,08% ± 0,05%	0,91% ± 0,06%	31,76 ± 0,21
PLA 3%	3,29% ± 0,09%	3,12% ± 0,10%	32,30 ± 0,51
PLA 5%	5,16% ± 0,08%	4,99% ± 0,09%	30,67 ± 0,07

4.2.2.2 Filaments

The results of the thermogravimetric analysis of the filaments will be discussed in this section. For the filaments, only the summary of the averages with their standard deviation is given. Figure 21, figure 22, figure 23, table 22 and table 23 give a summary of the obtained results. The values of PLE 005 have not been included in these figures and tables, this because the PLE 005 did not undergo single-screw extrusion, therefor there are no PLE 005 filaments. Instead PLA/HA 0% will be used as a reference, since it passed through the same processes.

Figure 21 shows the onset temperature of the degradation for all composites. Compared to the granules, the evolution of the onset temperature with the addition of HA is completely different. Even though the standard deviation of the extruded PLA is very high, the addition of HA does not result in a drastic difference from 0.5% to 1% of HA. After this there is the onset temperature decreases for 3%, but unlike for the granules, the addition of 5% of HA results in a slight rise of the onset temperature. However, despite the evolution of the onset temperature being different, the degradation onset occurs at lower temperatures (5.2°C lower on average) for the filaments. The explanation for the start of the degradation at lower temperatures, can be found in the processing of the composites, which leads inevitably to a slight degradation of the polymer material. This degradation that occurs during the extrusions (single-screw and twin-screw) results in the material being more susceptible to degradation.

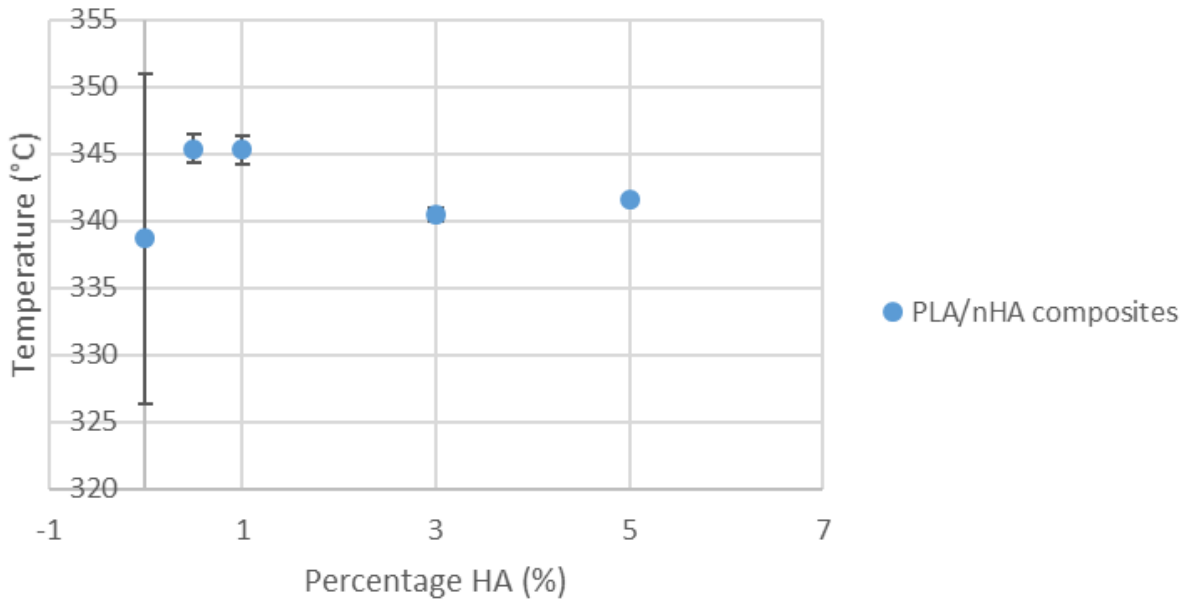

Figure 21 Temperatures at which the degradation starts for the different composites and the extruded PLA.

Figure 22 shows the temperature for which there is a maximum for the degradation speed. The addition of 0.5% HA to PLA leads to the maximum occurring at a much lower temperature. With the addition of more HA, the maximum will shift to a higher temperature until 3% of HA is added, after which the maximum will occur at lower values again when 5% of HA is added. This evolution of the maximum degradation speed is almost completely opposite of that of the granules, for which the maximum occurred at decreasing temperatures before recovering for 5%. Additionally, the temperature values were 0.6°C higher on average for the filaments, when comparing the filaments with the granules obtained after the twin-screw extrusion. So, despite the filaments starting to degrade earlier, the degradation peak occurs at higher temperatures.

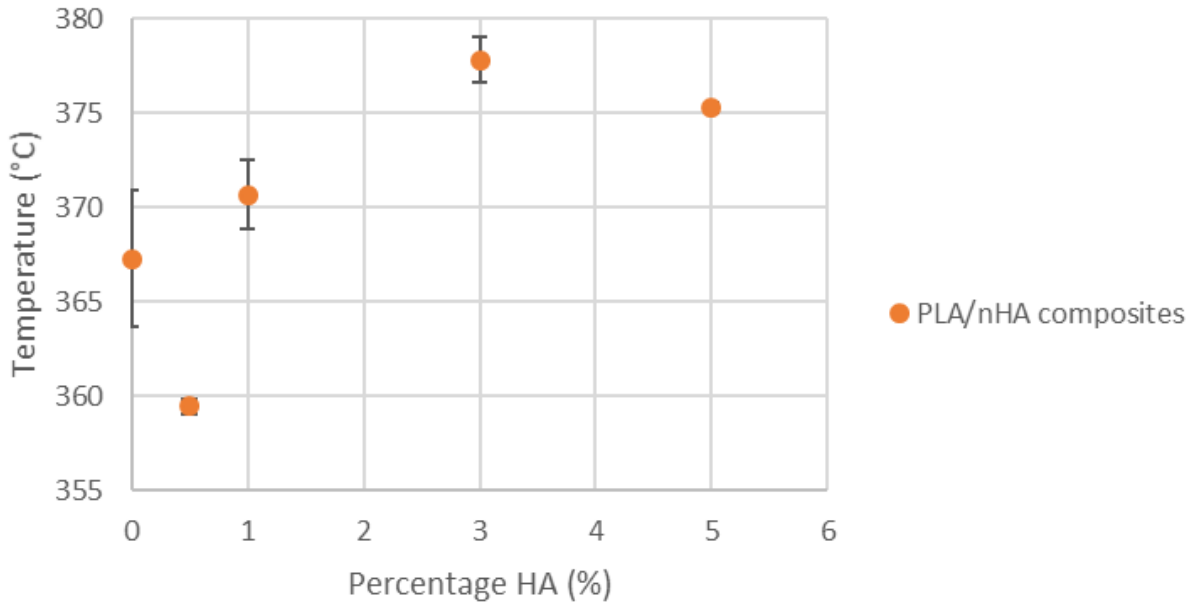

Figure 22 Temperatures at which the maximal degradation speed occurs for the composites and the extruded PLA.

In figure 23 the end temperature of the degradation for the composites is shown in function of the added HA percentage. On average the degradation ended 1.6°C later than the granules. The end

temperature of the degradation evolves in the same way as the degradation peak temperature. However, the standard deviations are high and for the extruded PLA, PLA/nHA 0.5% and PLA/nHA 1% the temperature intervals overlap. Despite this, a trend is starting to appear, the temperatures at which the degradation speed is maximal for the composites and the temperatures at which the degradation ends appear to evolve in the same way.

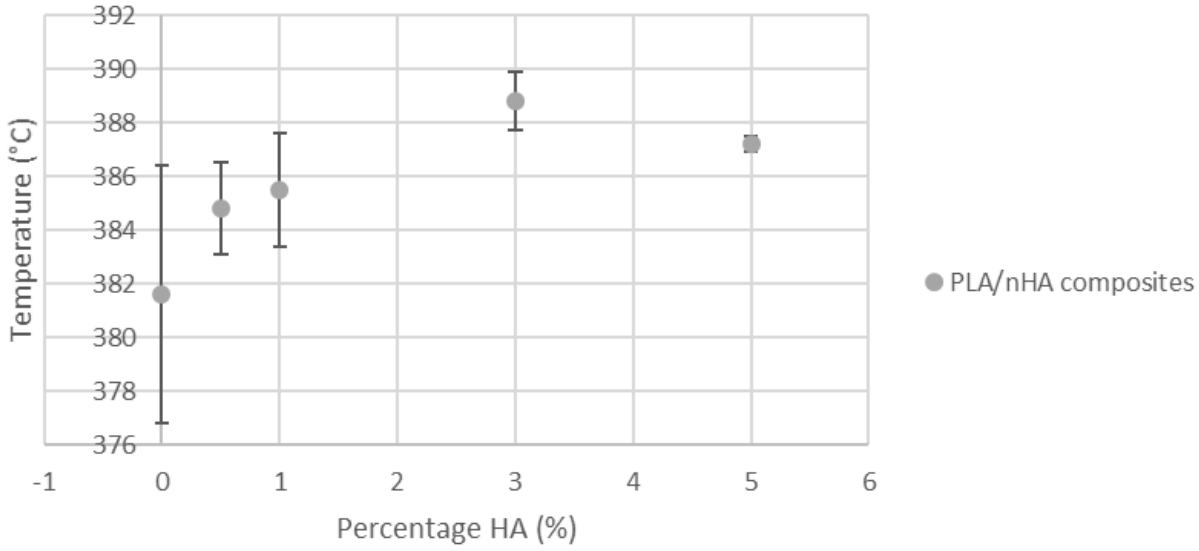

Figure 23 Temperature at which the degradation ends for the composites and the extruded PLA.

Table 22 gives the summary of the onset, peak and end temperatures of the degradation, as well as the temperature range in which the degradation happens. The temperature range of the fillaments appears to evolve following the peak temperature and the end temperature of degradation, which is different from the evolution for the granules. Additionally, the temperature ranges are on average 6.76°C larger than those of the granules. Thus, a potential hypothesis could be that the HA in the filaments is better dispersed and limits the movement more than the HA in the granules.

Table 22 Onset, peak degradation and degradation end temperature, and the temperature range in which degradation occurs of the filaments.

	T (°C)			Temperature range
Averages	Onset	Peak	Endset	Degradation (°C)
PLA extruded	338,7 ± 12,3	367,3 ± 3,6	381,6 ± 4,8	42,8 ± 7,9
PLA/HA 0,5%	345,4 ± 1,1	369,5 ± 0,4	384,8 ± 1,7	39,4 ± 2,8
PLA/HA 1%	345,3 ± 1,1	370,7 ± 1,8	385,5 ± 2,1	40,2 ± 3,2
PLA/HA 3%	340,5 ± 0,5	377,8 ± 1,2	388,8 ± 1,1	48,3 ± 1,5
PLA/HA 5%	341,6 ± 0,2	375,3 ± 0,3	387,2 ± 0,3	45,6 ± 0,3

In table 23 the remaining mass after the TGA, the calculated percentage of HA and the maximal mass loss per minute are shown. Compared to the percentage of HA found for the granules, the HA percentage in the filaments is 0.12% lower. An explanation for the difference is that the single-screw extrusion process partially removed some HA from the composites. The maximum mass loss per minute decreases with the addition of more HA until 3% of HA is added, after which the mass loss recovers slightly. The lowest maximum mass loss for the 3% composite can be explained, since the 3% composite has the largest temperature range in which degradation occurs and the degradation starts very early for this composite. The highest maximum mass loss for the extruded PLA cannot be explained with its temperature range, given that it has a bigger temperature range than the 0.5%

composite, but a significantly higher maximum mass loss per minute. An explanation can be found in the standard deviation of the onset temperature, which is 12.3°C. It is thus very likely that the onset of the extruded PLA occurs at higher temperatures, this would decrease the temperature range and explain the high maximum mass loss per minute. The maximum mass loss per minute was found to be 1.39%/min lower on average for the filaments when compared to the granules. After the single-screw extrusion process, the degradation occurred earlier because of pre-degradation. Gel permeation chromatography could verify this pre-degradation. As mentioned before, the degradation kinetics were lower because of a better dispersion of the filler, hindering the mechanisms of thermal degradation. The dispersion of the filler can be verified with transmission electron microscopy.

Table 23 Remaining mass, percentage HA and maximum degradation speed of the filaments.

	Mass		Mass loss per minute (%/min)
Averages	Remaining mass (%)	HA (%)	Peak
PLA extruded	0,19% ± 0,05%	0%	32,22 ± 2,75
PLA/HA 0,5%	0,65% ± 0,04%	0,46% ± 0,09%	30,78 ± 0,99
PLA/HA 1%	1,06% ± 0,03%	0,87% ± 0,08%	30,03 ± 1,36
PLA/HA 3%	3,04% ± 0,02%	2,85% ± 0,07%	28,93 ± 0,59
PLA/HA 5%	4,99% ± 0,05%	4,80% ± 0,10%	29,07 ± 0,55

4.2.2.3 FDM specimens

The results of the thermogravimetric analysis of the FDM printed specimens will be discussed in this section. For the FDM specimens, only the summary of the averages with their standard deviation is given. Figure 24, figure 25, figure 26, table 24 and table 25 give a summary of the obtained results. The values of PLE 005 have not been included in these figures and tables, this because the PLE 005 did not undergo single-screw extrusion, thus there were no PLE 005 filaments for the FDM printing process and no FDM specimens were created.

In figure 24, the temperatures at which the degradation begins for the FDM specimens is given. The temperature at which the degradation begins lowers with the addition of HA apart from when 5% of HA is added, for which the temperature increases slightly compared to the 3% composite. Compared to the granules, the degradation started on average 2.1°C earlier. This is later than the filaments, for which the degradation started 5.2°C earlier than the granules. Additionally, the evolution of the onset does not correspond to the granules nor the filaments. The earlier start of the degradation for the filaments can be the result of a higher surface/volume ratio. Although other factors can also influence the start, given the 5.2°C difference with the printed samples.

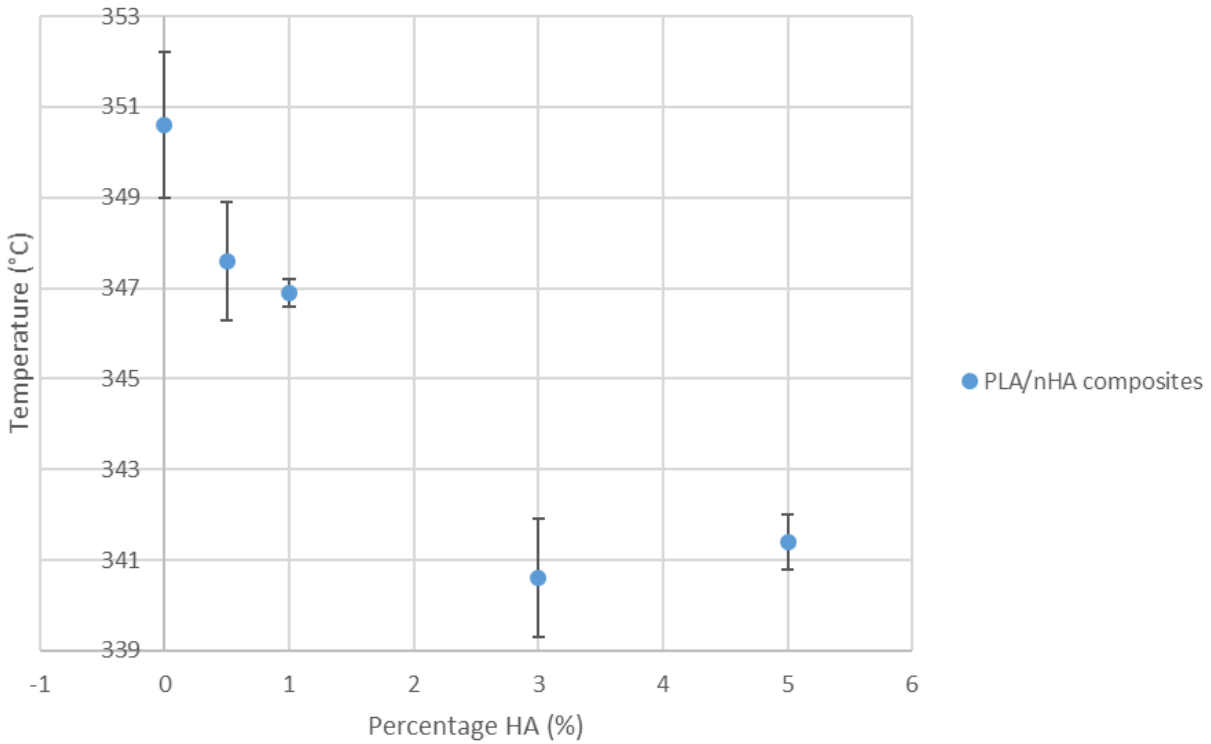

Figure 24 The degradation onset temperature of the FDM specimens.

Figure 25 shows the temperatures at which the degradation speed was maximal for the FDM specimens. The temperature increases with the addition of 0.5% HA, followed by a platform with the addition of 1% HA, after which the temperature increases drastically for 3% HA, before finally decreasing for 5% HA. On average, the temperature at which the maximum degradation speed occurred increased 0.5°C, which is slightly less than the increase in temperature for the filaments (0.6°C). The nanocomposite was more sheared in the extrusions than in the FDM process.

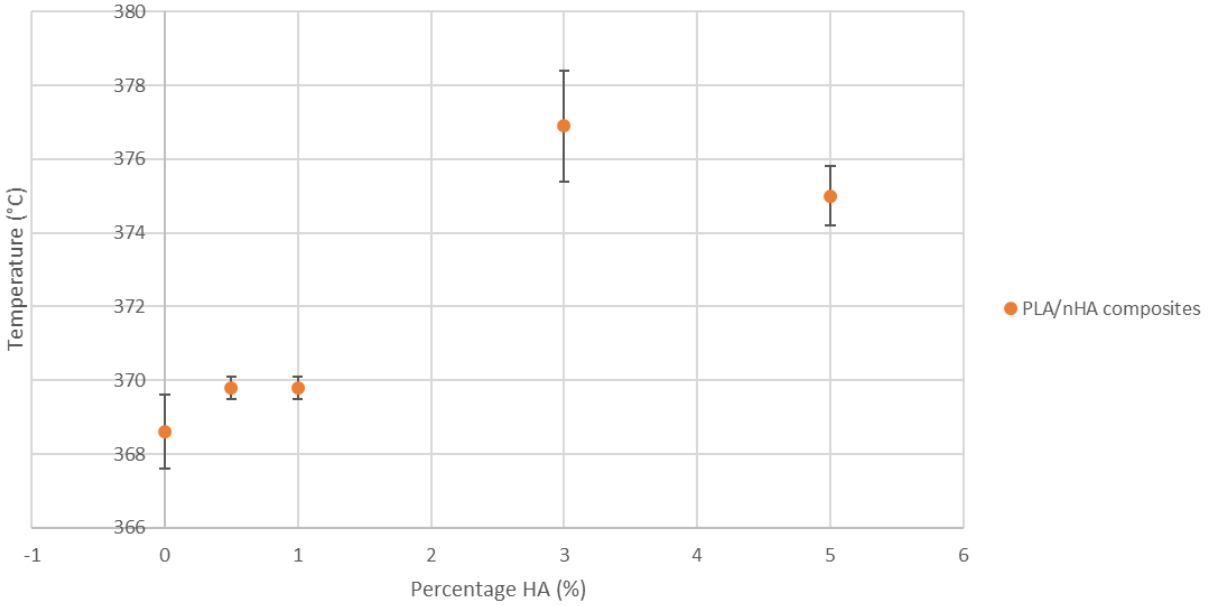

Figure 25 The temperature at which the degradation speed was maximal for the FDM specimens.

In figure 26 the temperatures at which the degradation end, are plotted against the percentage of HA. The temperatures evolve similar to those of the degradation peak temperatures, confirming the trend we previously detected. On average the degradation ended 1.5°C later when comparing the

degradation profile of the FDM specimens to that of the granules. The degradation ended on average faster than that of the filaments, for which the degradation ended 1.6°C later than that of the granules. This further indicates that the FDM process has a less drastic impact on the degradation process.

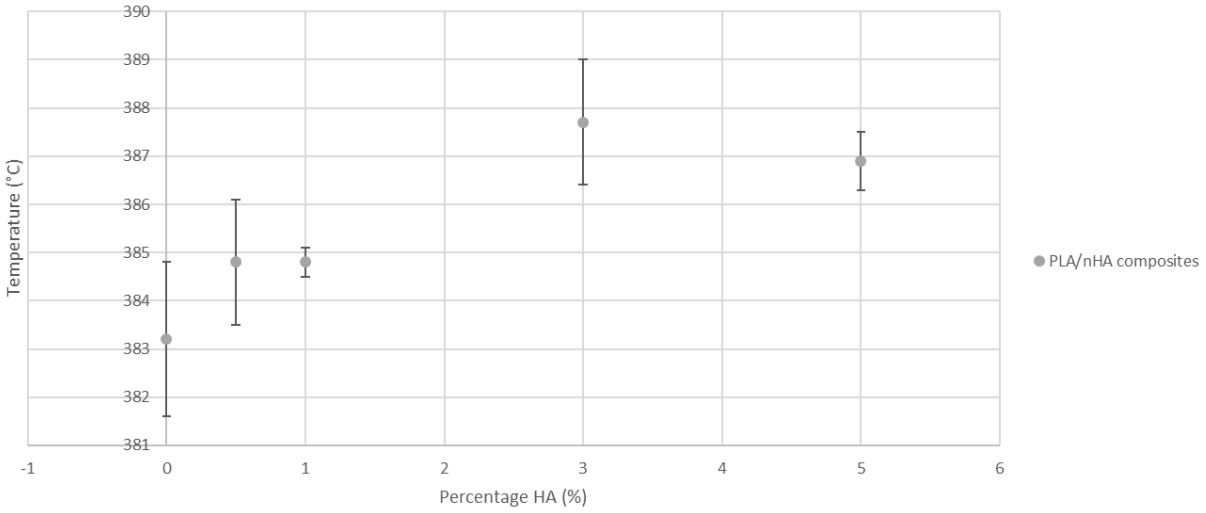

Figure 26 The temperatures at which the degradation ended for the FDM specimens.

Table 24 contains the average degradation onset, peak and end temperature and the average temperature range of the degradation for each composite and the pure PLA. The temperature range increases when adding up to 3% of HA to PLA, after which the temperature range stagnates. On average the temperature range is 3.6°C larger than that of the granules, but smaller than the average temperature range of the filaments, which was 6.8°C larger than that of the granules. Transmission electron microscopy will show whether the HA dispersion is better for the FDM printed samples, which would explain why the temperature range decreases from filament to FDM specimen, given the presence of a degradation kinetic hindering effect caused by HA.

Table 24 The degradation onset, peak and end temperature; and the temperature in which degradation occurred for the FDM specimens.

	T (°C)			Temperature range
Averages	Onset	Peak	Endset	Degradation (°C)
PLA extruded	350,6 ± 0,5	368,6 ± 1,0	383,2 ± 1,6	32,6 ± 1,7
PLA/HA 0,5%	347,6 ± 0,4	369,8 ± 0,3	384,8 ± 1,3	37,2 ± 1,7
PLA/HA 1%	346,9 ± 0,4	369,8 ± 0,3	384,8 ± 0,3	37,9 ± 0,6
PLA/HA 3%	340,6 ± 2,2	376,9 ± 1,5	387,7 ± 1,3	47,1 ± 3,4
PLA/HA 5%	341,4 ± 0,5	375,0 ± 0,8	386,9 ± 0,6	45,5 ± 0,9

The remaining mass, the percentage of HA and the maximum mass loss per minute are shown in table 25. The FDM process further removes some HA from the composites. Despite the pre-degraded matrix after the single-screw extrusion, the temperature range of degradation was lower for FDM specimens, when compared to the filaments. Given the lower amount of HA, the slower degradation kinetics are most likely the result of a better dispersion of HA, which leads to a slower degradation. As mentioned before, the dispersion of the HA in the polymer matrix can be verified with transmission electron microscopy. The maximum mass loss per minute decreases until 3% of HA is added, after which the mass loss per minute increases slightly. The average maximum mass loss per minute is 1.31%/min lower than that of the granules, which is on average slightly higher than the maximum mass loss per

minute of the filaments. This indicates that the composites and the PLA were less susceptible to degradation after the FDM process, when compared to before the process.

Table 25 The remaining mass, the HA percentage and the maximum mass loss per minute for the FDM specimens.

	Mass		Mass loss per minute (%/min)
Averages	Remaining mass (%)	HA (%)	Peak
PLA extruded	0,32% ± 0,06%	0%	32,30 ± 1,40
PLA/HA 0,5%	0,73% ± 0,01%	0,41% ± 0,07%	30,51 ± 1,26
PLA/HA 1%	1,09% ± 0,08%	0,77% ± 0,14%	30,32 ± 0,78
PLA/HA 3%	3,10% ± 0,01%	2,78% ± 0,07%	29,03 ± 0,75
PLA/HA 5%	5,23% ± 0,33%	4,91% ± 0,39%	29,30 ± 0,33

4.2.3 Conclusion

After the TGA, the HA content of the composites was found to be close to the target concentrations of 0%, 0.5%, 1%, 3% and 5%. However, the single-screw extrusion and the FDM printing process both result in a loss of HA content. The degradation of the composites was found to start the earliest for the filaments (after single-screw extrusion), yet the composites were again less susceptible to degradation at lower temperatures after the FDM printing process. Despite the earliest start of the degradation, the filaments did have to lowest average maximum degradation speed. The filaments had the second lowest maximum degradation speed. This can be linked to the fact that the maximum degradation speed occurs at a higher temperature, when more material has already been degraded. Finally, the degradation ended on average the latest for the filaments, with the FDM specimens finishing slightly earlier. In summary, the filaments are the first to start degrading when the temperature is increased, due to pre-degradation caused by the single-screw extrusion. However, from the analysis, a degradation kinetic hindering effect of HA, which increases with the dispersion of HA in the polymer matrix, is proposed. The dispersion of HA can be verified using transmission electron microscopy and is likely the reason why the FDM process has a less drastic impact on the degradation process, when compared to the single-screw extrusion.

4.3 Differential scanning calorimetry

4.3.1 Introduction

For the DSC, the goal of the analysis was to obtain information regarding the phase transitions and the crystallinity rate of the pellets, the filaments and the printed samples. Additionally, the analysis aided in the determination of the minimum printing temperature of the FDM printing process and the dispersion of HA in the PLA matrix. As mentioned before, the DSC consisted of two heating/cooling cycles. Only the first cooling ramp and the second heating ramp of each measurement were analysed. Information regarding the following phase transitions was obtained: the crystallisation upon cooling (T_c), the glass transition (T_g), the cold crystallisation (T_{cc}), the melting upon heating (T_m).

For the glass transition, the temperature onset, inflection and peak (corresponding to the enthalpic relaxation) temperature; and the height of the transition were determined. Similarly, for the crystallisation upon cooling, the onset, peak and end temperature were determined, as well as the crystallisation enthalpy (ΔH_c). The onset, peak and end temperature, and the cold crystallisation

enthalpy (ΔH_{cc}) were determined for the cold crystallisation. Finally, the onset, peak and end temperature, and the melt enthalpy (ΔH_m) were determined for the melting peak. Additionally, the first and second derivative were used to check whether the melting peak displayed a shoulder. T_g corresponds to the inflection temperatures found for the glass transition. T_c, T_{cc} and T_m all correspond to the peaks of their respective phase transitions.

4.3.2 Results

4.3.2.1 Granules

In this section the DSC results of the granules will be discussed. First PLE 005 will partially be discussed, because its DSC curves differ from the other granules. Table 26 and figure 27 give more information with regards to the phase transitions unique to PLE 005. For the PLE 005 there was no crystallisation peak upon cooling, as seen in figure 27. The T_g of PLE 005 was found to be 61.2°C, previous works have already found values close to this one [202]. Right after the glass transition, there was an endothermic peak. Mróz et al. explain this peak as a relaxation process [50]. After this endothermic peak, PLE 005 displayed an exothermic col crystallisation peak. Zhang et al. show that α' to α transition happens during the melting between 150°C and 170°C, therefor the exothermal peak, observed during the heating cycle, does not correspond to this transition [203]. Instead this peak corresponds to the cold crystallisation [50]. T_{cc} was determined and found to be 139.7°C, with the cold crystallisation ranging from 110.3°C to 163.2°C. and the corresponding ΔH_{cc} being 20.38 J/g. Unlike the PLE 005, there is no cold crystallisation peak in the heating cycle for the other composites. This despite the same heating and cooling rate of 5 K/min for PLE 005 and the composites.

Table 26 Cold crystallisation peak and the relaxation peak after the T_g.

	Peak after Tg			Cold crystallisation					
PLE 005	Onset (°C)	Peak (°C)	Delta Cp* (J/(g*K))	Onset (°C)	Peak (°C)	End (°C)	Area (J/g)	Width (°C)	Heigth (mW/mg)
1	58,7	65,3	-0,3381	115,7	141,8	166,3	16,97	50,5	0,1702
2	59,3	65,0	-0,3963	106,7	137,7	160,7	26,03	39,2	0,1300
3	59,6	65,1	-0,3580	108,6	139,5	162,5	18,15	37,9	0,1038
Average	59,2	65,1	-0,3641	110,3	139,7	163,2	20,38	42,5	0,1347
STDEV	0,5	0,2	0,0296	4,7	2,1	2,9	4,93	6,9	0,0334

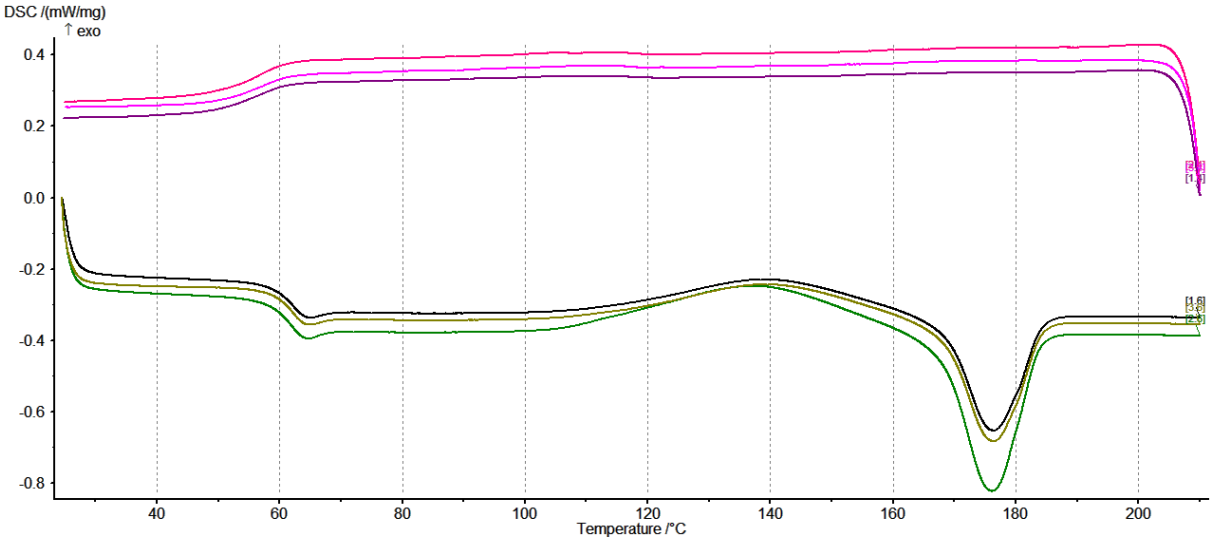

Figure 27 The DSC curves of the PLE 005.

In figure 28, figure 29 and table 27, information regarding the crystallisation upon cooling is displayed. Unlike PLE 005, PLA extruded does have a crystallisation peak during the cooling as shown in figure 30. Pillin et al. explain that it is likely to be ascribed to a gradual decrease of the molecular weight caused by the extrusion of PLA [204]. This decrease in molecular weight results in short PLA chains that can act as nucleating agents and allow crystallisation at this cooling rate, additionally, the short chains also promote mobility. In this case the crystallisation temperature of the extruded PLA corresponded to 108.0°C, with a crystallisation enthalpy of 41.21 J/g. The crystallisation temperature of PLA/nHA 0.5% was found to be 107°C, which is lower than that of the extruded PLA. Additionally, the crystallisation enthalpy, 38.25 J/g was also lower. PLA/HA 1% has a crystallisation temperature of 107.1°C, which is lower than the 108°C found for the extruded PLA and close to that of PLA/HA 0.5%. The crystallisation enthalpy of 36.79 J/g is very close to that of PLA/HA 0.5%. For the PLA/HA 3%, the crystallisation temperature was 108.2°C, similar to the 108°C found for the extruded PLA. The crystallisation enthalpy, 37.47 J/g, was also close to that of PLA/HA 1%. PLA/HA 5% had a crystallisation temperature corresponding to 108.7°C, which is higher than the 108°C found for the extruded PLA. The crystallisation enthalpy of 38.88 J/g is a slight increase compared to that of PLA/HA 3%. In figure 29, the obtained crystallinity during the cooling cycle is shown. Equation 13 was used to calculate the crystallinity from the found enthalpy, and the mass fraction of PLA was taken into account. The crystallinity decreases from pure PLA up to the addition of 1% of HA, after which the crystallinity increases and finally surpasses that of the pure PLA when 5% of HA is added.

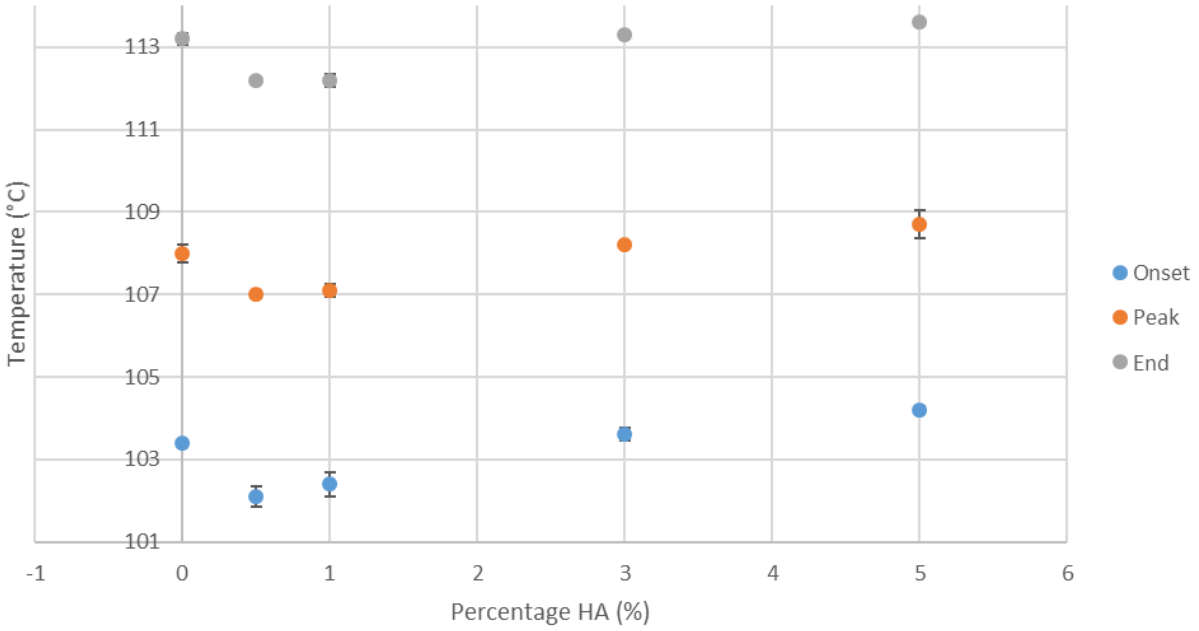

Figure 28 The onset, peak and end of the crystallisation during the cooling cycle.

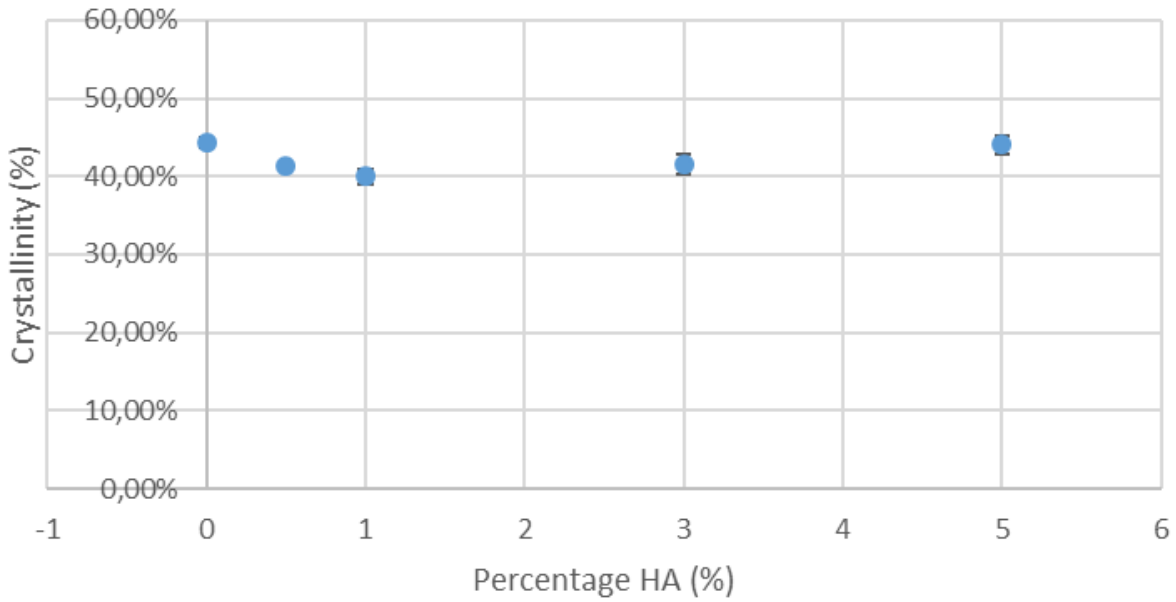

Figure 29 The crystallinity obtained during the cooling cycle of the composites.

Table 27 Summary of the crystallisation during the cooling cycle.

	Crystallisation upon cooling				
Summary	Onset (°C)	Peak (°C)	End (°C)	Area (J/g)	Xc
PLA extruded	103,4 ± 0,1	108,0 ± 0,2	113,2 ± 0,1	41,21 ± 0,6	44,31% ± 0,65%
PLA/HA 0,5%	102,1 ± 0,3	107,0 ± 0,1	112,2 ± 0	38,25 ± 0,1	41,34% ± 0,11%
PLA/HA 1%	102,4 ± 0,3	107,1 ± 0,2	112,2 ± 0,2	36,79 ± 0,9	39,96% ± 0,98%
PLA/HA 3%	103,6 ± 0,2	108,2 ± 0,1	113,3 ± 0,1	37,47 ± 1,1	41,54% ± 1,22%
PLA/HA 5%	104,2 ± 0,1	108,7 ± 0,3	113,6 ± 0,1	38,88 ± 1,0	44,01% ± 1,13%

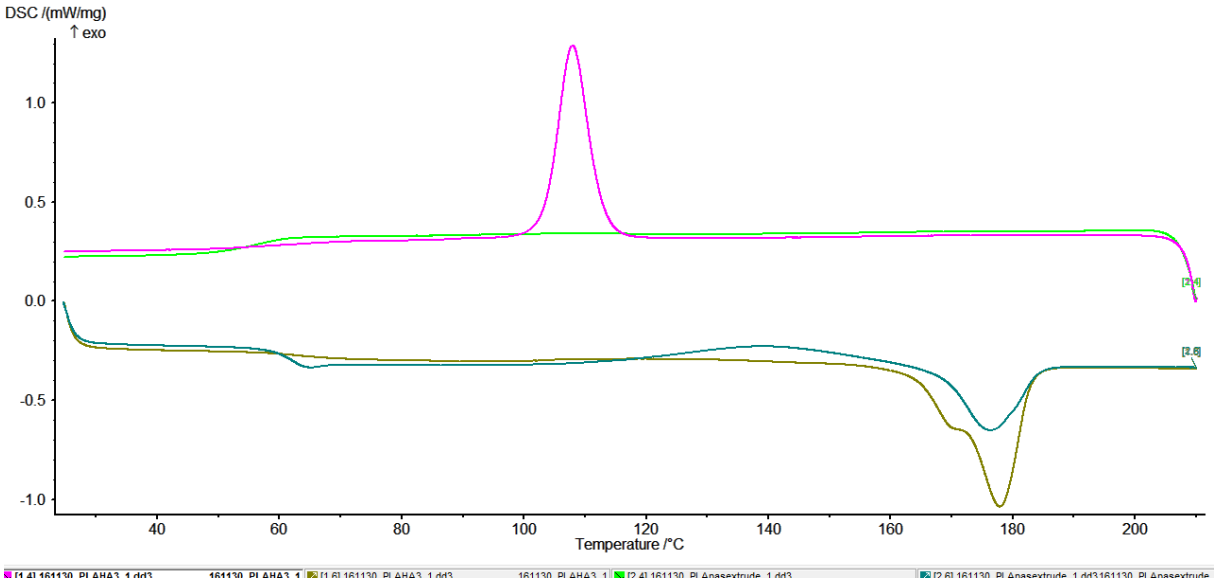

Figure 30 DSC curves of PLE 005 (bright green and blue) and PLA extruded (pink and dark green).

Figure 31, figure 32 and table 28 contain information regarding the glass transition of the granules. In figure 31, the onset, inflection and end temperature of the glass transition are visualised. PLE 005 has the smallest temperature range in which the T_g occurs and the T_g occurs at a lower temperature. The T_g range increases after the extrusion of PLA. Additionally, the range also appears to increases as the

HA content increases, however, the standard deviations are too high to be certain this is the case. On top of that, the software also had issues determining the T_g of the composites due to the low height difference. Despite the increase in range, the T_g (inflection) does not change significantly with every T_g having overlapping ranges. However, the height of the T_g is significantly lower for the composites, 0.394 J/(g*K) on average. The height also appears to decrease with the addition of more HA. Given that the height of the glass transition is proportional to the amorphous phase present in the polymer material, the decreasing height can be linked to the previously found increasing crystallinity during the cooling cycle. The addition of HA also results in a more spread out glass transition, which can be observed when looking at the DSC curves of the composites (Figure 30).

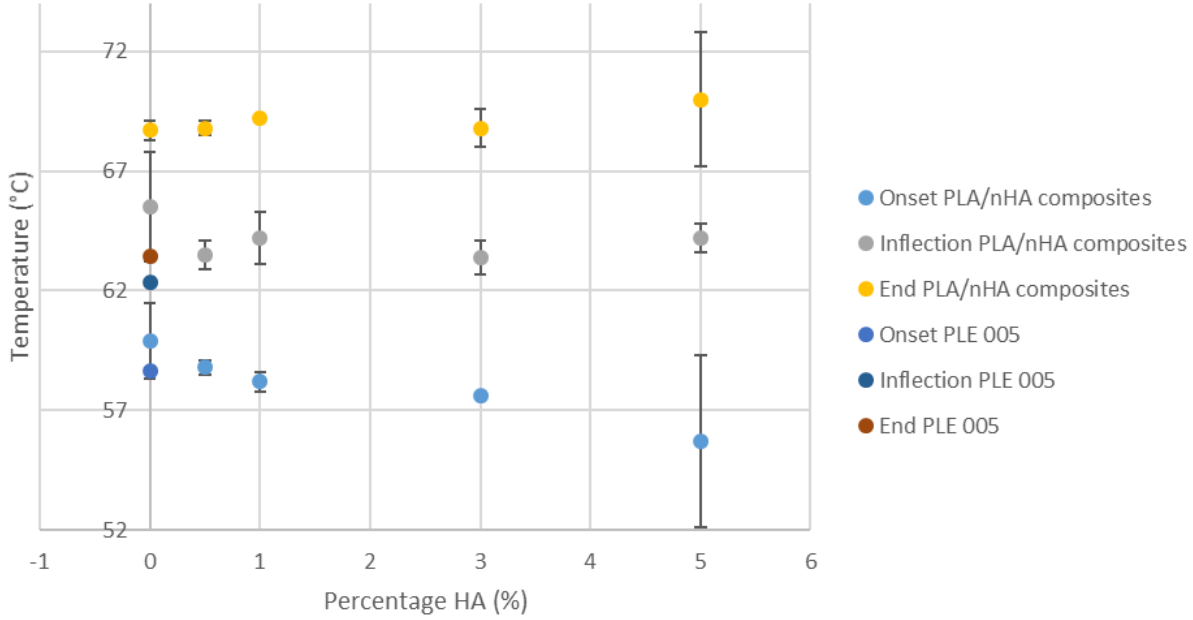

Figure 31 Glass transition PLE 005 and PLA/nHA composites.

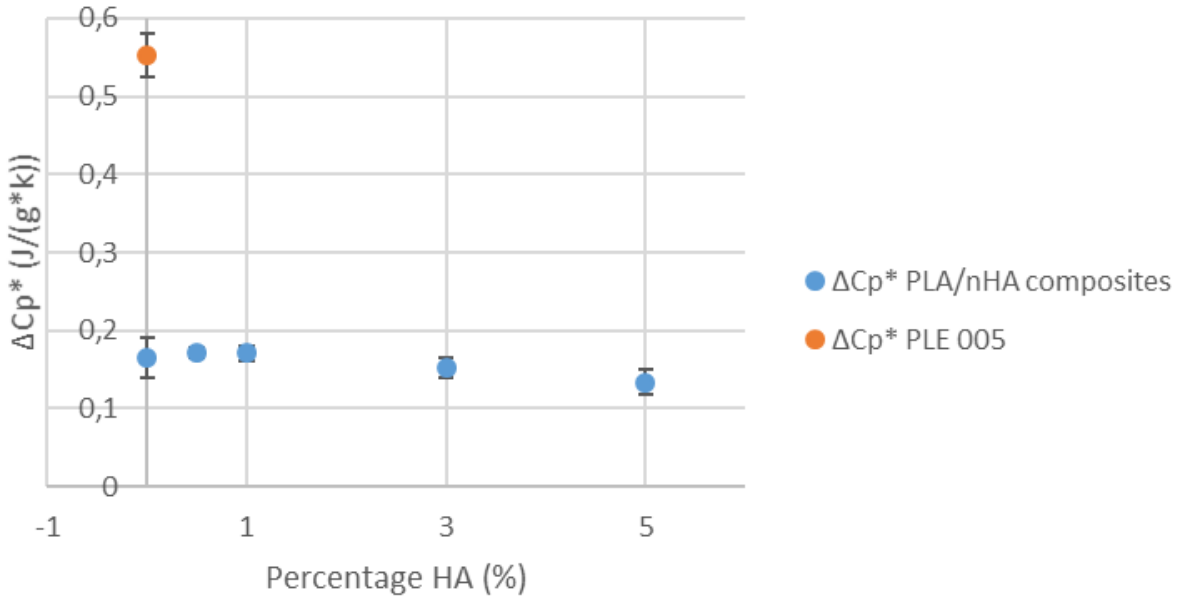

Figure 32 The height of the glass transition of the PLE 005 and the PLA/nHA composites.

Table 28 Temperatures characterising the glass transition and the height of the glass transition (ΔCp).

Averages	Glass transition				
	Onset (°C)	Mid (°C)	Inflection (°C)	End (°C)	Delta Cp* (J/(g*K))
PLE 005	58,7 ± 0,3	61,2 ± 0,2	62,3 ± 0,1	63,4 ± 0,2	0,553 ± 0,027
PLA Extruded	59,9 ± 1,6	63,9 ± 0,1	65,5 ± 2,3	68,7 ± 0,4	0,165 ± 0,025
PLA/HA 0,5%	58,8 ± 0,3	63,7 ± 0,4	63,5 ± 0,6	68,8 ± 0,3	0,172 ± 0,006
PLA/HA 1%	58,2 ± 0,4	63,6 ± 0,2	64,2 ± 1,1	69,2 ± 0,1	0,171 ± 0,010
PLA/HA 3%	57,6 ± 0,1	62,7 ± 0,1	63,4 ± 0,7	68,8 ± 0,8	0,153 ± 0,013
PLA/HA 5%	55,7 ± 3,6	63,1 ± 0,3	64,2 ± 0,6	70,0 ± 2,8	0,133 ± 0,016

Figure 33, figure 35 and table 29 contain information regarding the melt peak. The melting temperature of PLE 005 is slightly lower than the composites and the temperature range of the peak is slightly bigger. For the composites, the peak temperature decreases slightly while the temperature range decreases as more HA is added to the polymer matrix. A shoulder on the right side was detected in the melt peak of the PLE 005, by using the first derivative. This shoulder is an indication for the distribution between α' and α phases of PLA. A shoulder on the right corresponds to more α' phase and a shoulder on the left corresponds to more α phase PLA [203]. Additionally, the α phase is more stable than the α' phase and will thus require more energy to melt and have a higher melting temperature. The extruded PLA displayed a shoulder on the left side of the peak, indicating more α' phase. For the other composites, there was also a shoulder on the left side, which became more visible with the addition of more HA. A new phenomenon appeared for the 5% composite; the apparition of a multi melt peak, as seen in figure 34. Finally, in figure 35 the crystallinity of the PLE 005 and the composites is compared. The crystallinity of PLE 005 is much lower than that of the composites. For the composites the 5% composites has the highest crystallinity, followed by the pure PLA. In between the crystallinity declines until 1% of HA is added, after which the crystallinity increases again. From this it can be concluded that the HA does not facilitate crystallisation in concentrations lower than 5%. The evolution of the crystallinity is the same as that found during the cooling cycle. However, there is a discrepancy between the found percentages for the composites during the cooling and the heating cycle. On average the crystallinity found for the composites during the cooling cycle was 6.57% lower, indicating a cold crystallisation occurred during the heating cycle of the composites. This cold crystallisation was not visible, as it was a low amount of enthalpy spread over a wide range of temperatures.

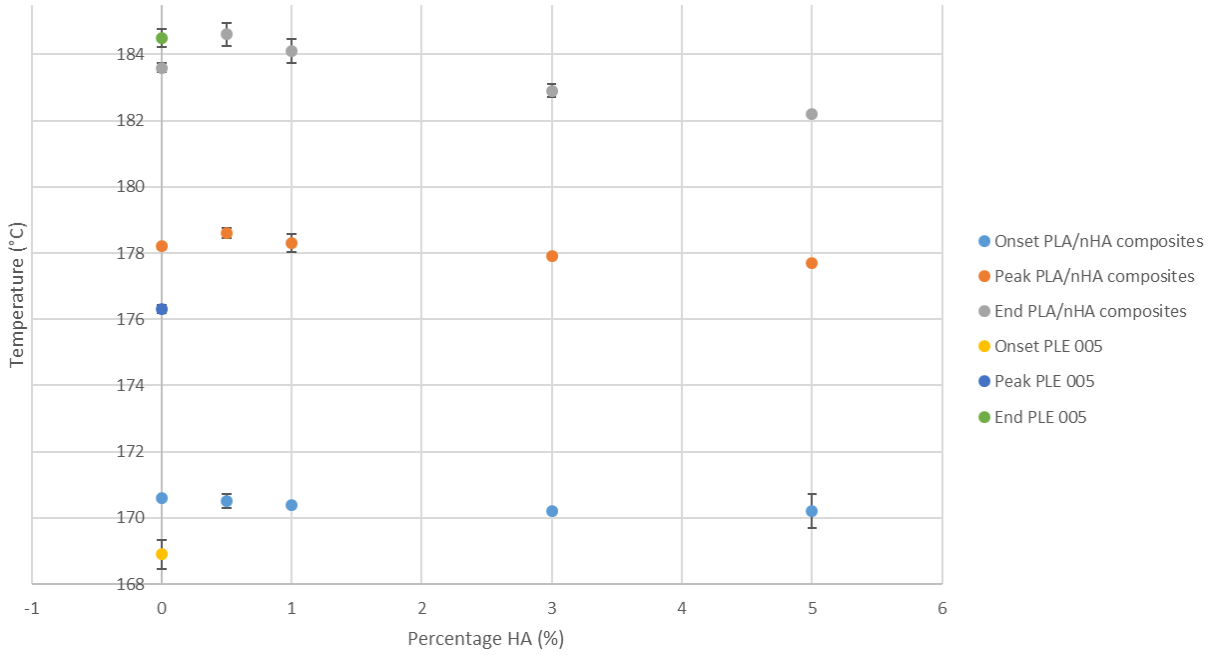

Figure 33 Onset, peak and end temperature melting peak PLE 005 and the composites.

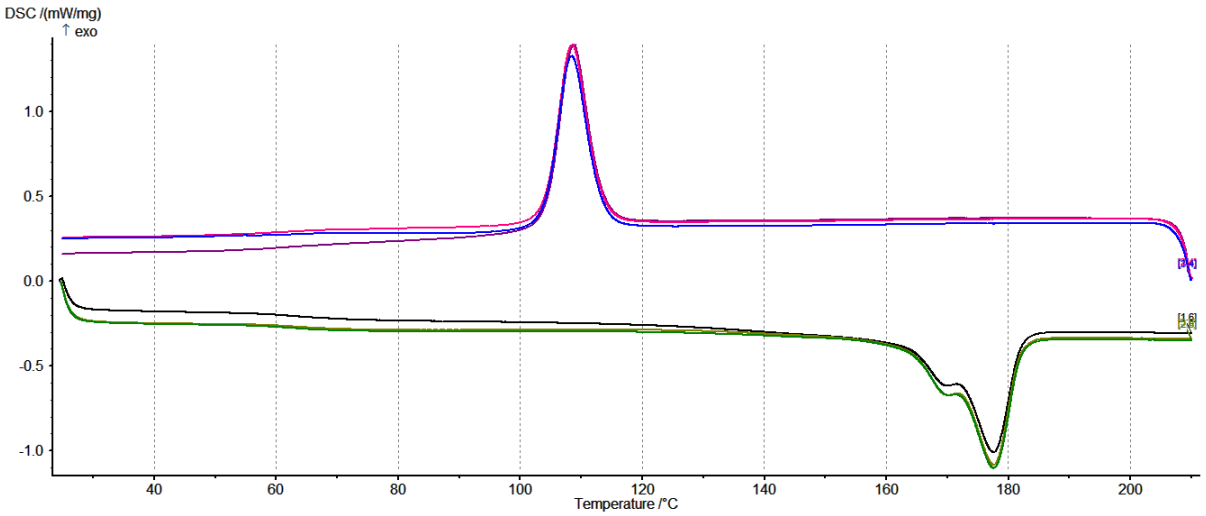

Figure 34 Multi melt peak PLA/Nha 5%.

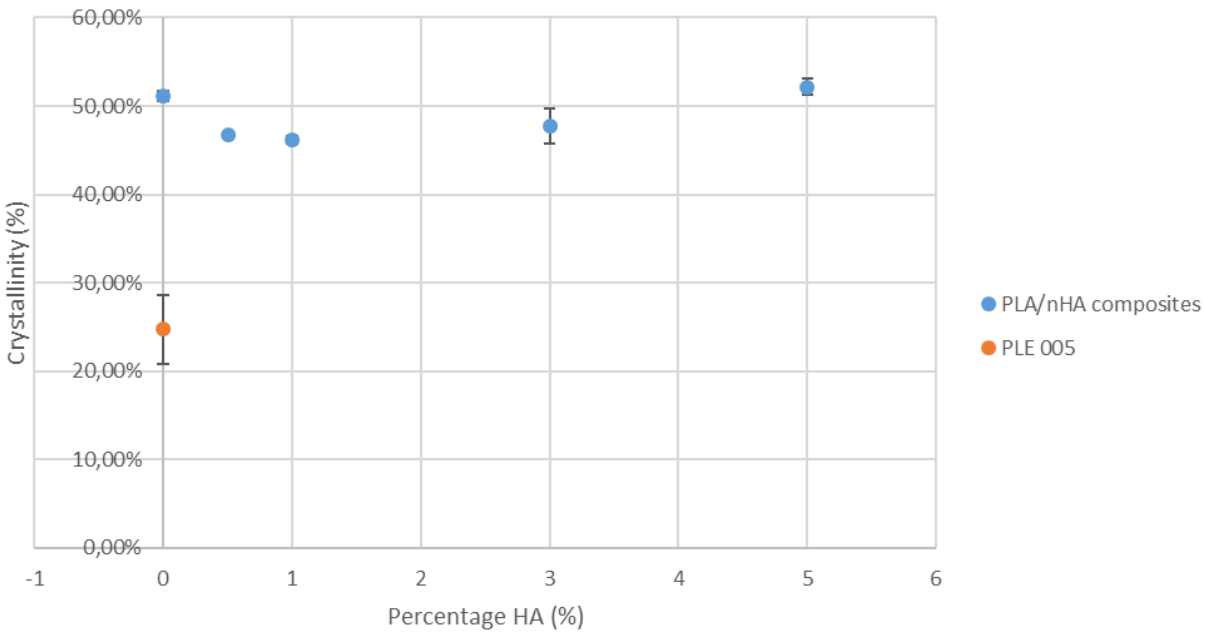

Figure 35 Crystallinity obtained from the melt peak of the PLE 005 and the composites.

Table 29 Summary melting peak PLE 005 and composites.

	Melting peak				
Summary	Onset (°C)	Peak (°C)	End (°C)	Area (J/g)	Xc (%)
PLE 005	168,9 ± 0,4	176,3 ± 0,1	184,5 ± 0,3	-22,99 ± 3,66	24,72% ± 3,94%
PLA extruded	170,6 ± 0	178,2 ± 0,1	183,6 ± 0,1	-47,58 ± 0,54	51,16% ± 0,58%
PLA/HA 0,5%	170,5 ± 0,2	178,6 ± 0,2	184,6 ± 0,4	-43,23 ± 0,19	46,72% ± 0,21%
PLA/HA 1%	170,4 ± 0,1	178,3 ± 0,3	184,1 ± 0,4	-42,50 ± 0,40	46,16% ± 0,43%
PLA/HA 3%	170,2 ± 0,1	177,9 ± 0,1	182,9 ± 0,2	-43,08 ± 1,83	47,76% ± 2,03%
PLA/HA 5%	170,2 ± 0,5	177,7 ± 0,1	182,2 ± 0,1	-46,11 ± 0,81	52,19% ± 0,92%

4.3.2.2 Filaments

The results of the DSC analysis of the filaments are summarised in table 30, table 31, table 32 and table 33, and figure 36. Table 30 and figure 36 show the starting crystallinity of the filaments. The starting crystallinity was calculated by measuring the difference between the crystallisation and the melting enthalpy of the first heating ramp. The composites are primarily amorphous as the highest percentage of crystallinity is 3.48% and all composites have overlapping intervals. The low crystallinity is the result of the quenching step during the twin-screw extrusion. Since the composites are highly amorphous, it could be possible to print at temperatures slightly above the T_g. However, the crystalline regions can cause nozzle clogging and upon deposition, the filaments will not bind probably because there is not enough energy available for inter filament penetration and diffusion.

Table 30 Starting crystallinity filaments.

Filaments	Starting crystallinity (%)
PLA/HA 0%	2,32% ± 0,94%
PLA/HA 0,5%	2,95% ± 0,83%
PLA/HA 1%	2,83% ± 0,90%
PLA/HA 3%	3,07% ± 0,36%
PLA/HA 5%	3,48% ± 1,18%

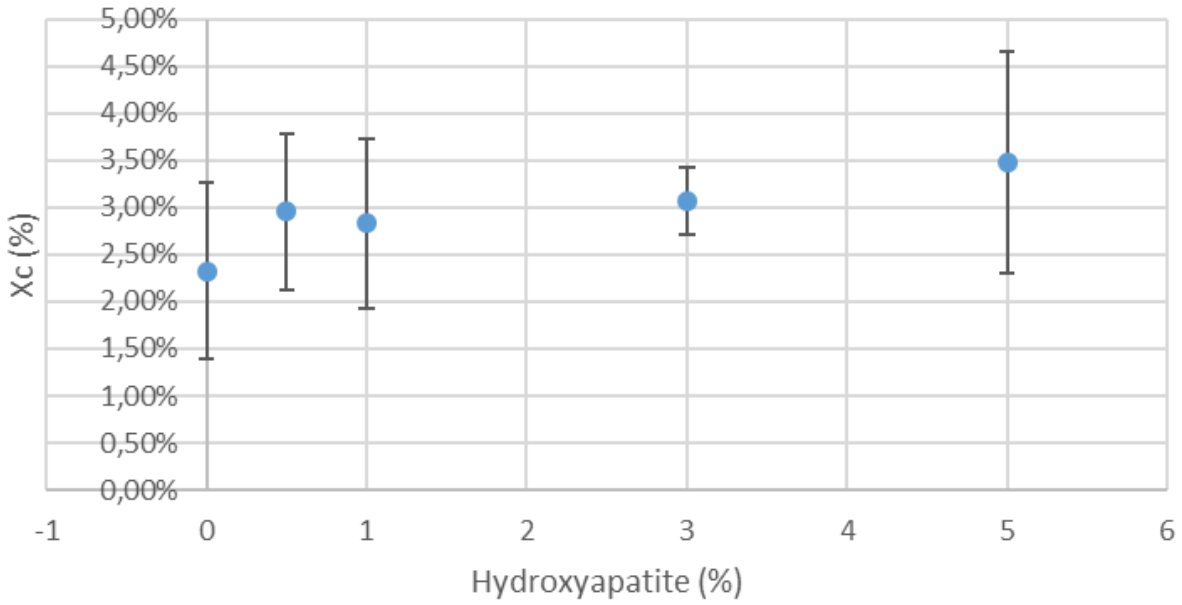

Figure 36 Starting crystallinity filaments visualised.

Table 31 gives information regarding the crystallisation peak upon cooling. The peak occurred around the same temperatures as for the granules, but evolved in a different way. There was a gradual increase of the crystallisation temperature with the addition of HA, except between 0.5% and 1% where the value remained the same. Additionally, the crystallinity obtained after cooling was on average 1.29% lower for the filaments, when compared to the granules. The crystallinity followed the same evolution as the crystallisation temperature when the HA content increased, which was different than the pattern found for the granules. Note that the crystallinity of the filaments is an important parameter for the FDM process, as amorphous filaments can be printed at lower temperatures (in theory just above the T_g). The danger of crystallinity is nozzle clogging, when the temperature of the FDM process is too low. However, higher properties can be reached if the printed samples can easily crystallise.

Table 31 Summary crystallisation filaments.

	Crystallisation filaments upon cooling				
Summary	Onset (°C)	Peak (°C)	End (°C)	Area (J/g)	Xc
PLA extruded	102,6 ± 0,3	107,4 ± 0,1	113,0 ± 0,2	36,97 ± 0,90	39,75% ± 0,97%
PLA/HA 0,5%	103,3 ± 0,3	107,7 ± 0,2	112,6 ± 0,1	37,33 ± 0,70	40,34% ± 0,76%
PLA/HA 1%	103,0 ± 0,5	107,7 ± 0,1	112,5 ± 0,1	37,11 ± 0,38	40,31% ± 0,76%
PLA/HA 3%	104,2 ± 0,2	108,5 ± 0,1	113,5 ± 0,1	37,54 ± 1,21	41,61% ± 1,34%
PLA/HA 5%	104,8 ± 0,2	108,9 ± 0,1	113,9 ± 0,1	37,71 ± 0,13	42,68% ± 0,15%

For the filaments, the glass transition was very similar to that of the granules. All the composites had a low glass transition height and the Tg was around the same temperature (Table 32). As with the granules, the analysis software had difficulties determining the Tg. The standard deviation on the obtained values was much higher this time, indicating the software had more difficulties.

Table 32 Summary glass transition filaments.

	Glass transition				
Averages	Onset (°C)	Mid (°C)	Inflection (°C)	End (°C)	Delta Cp* (J/(g*K))
PLA Extruded	65,4 ± 9,3	68,2 ± 5,3	63,7 ± 0,8	70,5 ± 1,7	0,1427 ± 0,0890
PLA/HA 0,5%	62,2 ± 4,0	67,1 ± 4,3	63,3 ± 2,6	67,9 ± 2,3	0,1170 ± 0,0840
PLA/HA 1%	65,2 ± 12,0	66,2 ± 11,5	64,4 ± 2,1	69,9 ± 1,9	0,1470 ± 0,1790
PLA/HA 3%	43,2 ± 14,6	47,8 ± 0,5	50,5 ± 15,8	52,3 ± 13,6	0,1400 ± 0,1796
PLA/HA 5%	55,5 ± 2,7	64,8 ± 1,7	68,4 ± 12,3	74,6 ± 5,9	0,2610 ± 0,1890

The values corresponding to the melting peak of the filaments are shown in table 33. The peak followed the same evolution as for the granules and happened around the same temperatures, it also showed the multi melt peak. However, the crystallinity determined for the composites is on average 1.17% lower for the filaments. There also was a discrepancy of 6.70% between the cooling enthalpy and the melt enthalpy. As for the granules, the crystallinity followed the same pattern as the previously found pattern for the cooling cycle with the addition of HA. This was different from the pattern obtained for the granules.

Table 33 Summary melt peak filaments.

	Melt peak filaments				
Summary	Onset (°C)	Peak (°C)	End (°C)	Area (J/g)	Xc
PLA extruded	171,0 ± 0,2	178,1 ± 0,2	183,4 ± 0,2	-43,17 ± 0,94	46,42% ± 1,01%
PLA/HA 0,5%	171,0 ± 0,0	177,9 ± 0,3	182,8 ± 0,6	-43,60 ± 0,64	47,12% ± 0,69%
PLA/HA 1%	170,9 ± 0,1	177,9 ± 0,1	182,8 ± 0,3	-43,18 ± 0,64	46,90% ± 0,70%
PLA/HA 3%	170,4 ± 0,1	177,6 ± 0,1	182,3 ± 0,2	-43,72 ± 1,24	48,46% ± 1,37%
PLA/HA 5%	170,4 ± 0,1	177,3 ± 0,1	180,9 ± 0,6	-43,53 ± 0,37	49,27% ± 0,42%

4.3.2.3 FDM specimens

The results of the DSC analysis of the FDM specimens are summarised in table 34, table 35, table 36 and table 37 and figure 37. Table 34 and figure 37, show the starting crystallinity of the FDM specimens. Apart from the neat PLA, the composites all have a higher crystallinity after the FDM process when compared to the crystallinity of the filaments. All composites have overlapping intervals, apart from the 3% composite, which only has an overlapping interval with the 1% composite. The higher crystallinity could help explain improved mechanical properties.

Table 34 Starting crystallinity FDM specimens.

FDM	Starting crystallinity (%)
PLA/HA 0%	2,58% ± 0,31%
PLA/HA 0,5%	8,71% ± 2,85%
PLA/HA 1%	5,96% ± 2,23%
PLA/HA 3%	5,58% ± 0,16%
PLA/HA 5%	6,40% ± 0,64%

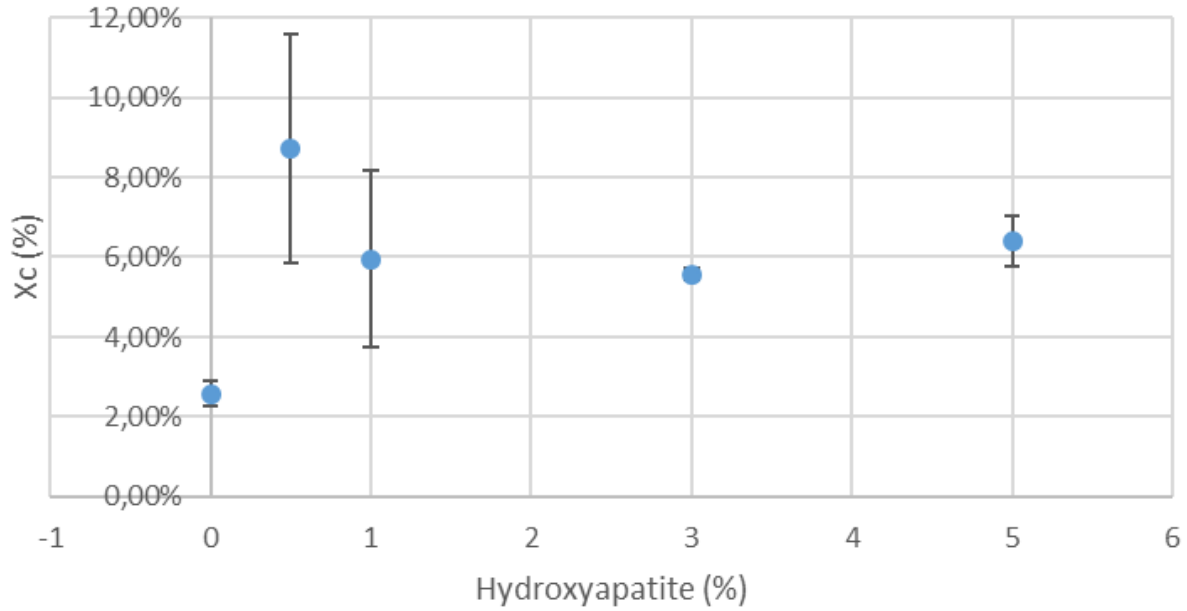

Figure 37 Starting crystallinity FDM specimens.

In table 35, information regarding the crystallisation peak is displayed. The evolution of the peak is close to that of the granules and occurs around the same temperatures, apart from the peak of pure PLA, which occurred at a lower temperature than the other composites. For the crystallinity, the evolution was different from the granules. The crystallinity increased with the addition of more HA and was on average 1.19% lower for the FDM specimens, when compared to the crystallinity upon cooling of the granules. The lower crystallinity of the FDM specimens could be linked to the reduced HA content, as shown by the TGA.

Table 35 Summary crystallisation FDM specimens.

	Crystallisation FDM specimens upon cooling				
Summary	Onset (°C)	Peak (°C)	End (°C)	Area (J/g)	Xc
PLA extruded	100,5 ± 0,7	106,3 ± 0,4	112,2 ± 0,2	36,64 ± 0,34	39,40% ± 0,37%
PLA/HA 0,5%	101,8 ± 0,4	106,9 ± 0,3	112,0 ± 0,3	37,89 ± 0,80	40,95% ± 0,86%
PLA/HA 1%	101,6 ± 0,5	106,7 ± 0,3	111,9 ± 0,2	36,82 ± 0,61	39,99% ± 0,66%
PLA/HA 3%	102,7 ± 0,7	107,7 ± 0,4	113,0 ± 0,2	37,90 ± 0,33	42,01% ± 0,37%
PLA/HA 5%	103,5 ± 0,5	108,3 ± 0,3	113,5 ± 0,2	37,85 ± 0,78	42,84% ± 0,88%

As for the filaments and the granules, the T_g occurred in the same temperature area and yet again the height was very low, as seen in table 36.

Table 36 Summary glass transitions FDM specimens.

	Glass transition FDM specimens				
Averages	Onset (°C)	Mid (°C)	Inflection (°C)	End (°C)	Delta Cp* (J/(g*K))
PLA Extruded	60,7 ± 2,5	66,6 ± 1,8	66,0 ± 0,2	70,8 ± 0,7	0,165 ± 0,031
PLA/HA 0,5%	59,8 ± 0,4	65,6 ± 0,1	64,2 ± 0,3	70,4 ± 0,4	0,172 ± 0,000
PLA/HA 1%	59,8 ± 0,4	65,3 ± 0,7	64,0 ± 0,4	70,0 ± 0,5	0,155 ± 0,006
PLA/HA 3%	59,5 ± 0,7	65,4 ± 0,9	63,0 ± 0,4	70,3 ± 0,4	0,143 ± 0,021
PLA/HA 5%	57,1 ± 0,1	64,5 ± 0,6	62,2 ± 2,0	70,6 ± 0,2	0,153 ± 0,011

Table 37, shows information regarding the melt peak of the FDM specimens. Melting occurs in the same temperature range, but the melting behaviour is different from the granules. There is no multi melt peak and the pure PLA has the highest melt temperature followed by a gradually lowering temperature as more HA is added. As for the granules and the filaments, the melt crystallinity evolved similar to the crystallinity upon cooling. The crystallinity increased with the addition of more HA. On average, the melt crystallinity was found to be 7.14% higher than the crystallinity found upon cooling. However, this was still 0.62% lower than the melt crystallinity found for the granules.

Table 37 Summary melt peak FDM specimens.

	Melt peak FDM specimens				
Summary	Onset (°C)	Peak (°C)	End (°C)	Area (J/g)	Xc
PLA extruded	170,6 ± 0,2	179,6 ± 0,4	186,6 ± 1,0	-42,67 ± 0,12	45,88% ± 0,13%
PLA/HA 0,5%	170,4 ± 0,1	179,0 ± 0,4	185,1 ± 0,5	-44,65 ± 0,62	48,25% ± 0,67%
PLA/HA 1%	170,4 ± 0,1	179,1 ± 0,4	185,3 ± 0,5	-43,23 ± 0,24	46,95% ± 0,26%
PLA/HA 3%	170,2 ± 0,6	178,9 ± 0,6	184,5 ± 1,2	-43,99 ± 0,21	48,76% ± 0,23%
PLA/HA 5%	170,1 ± 0,5	178,3 ± 0,6	183,4 ± 0,6	-45,11 ± 1,11	51,06% ± 1,26%

4.3.3 Conclusion

Based on the results from the DSC analysis, the minimum printing temperature of the FDM process has to exceed 183.4°C as this is the maximal end temperature of the melt peak found for the filaments. However, in practise the needed temperature was found to be greater than 190°C, which exceeds even the maximum end temperature of the FDM specimens (186.6°C). This is due to the heating ramp of the DSC process being much lower than the heating ramp applied to the material in the FDM process. The calculated starting crystallinity of the filaments indicated that printing could also be possible in between the glass transition and the crystallisation onset, however, crystalline regions could lead to nozzle clogging and printing at lower temperature does not allow for a good inter filament penetration and diffusion, ultimately leading to lower mechanical properties. A higher calculated starting crystallinity for the FDM composites, when comparing them to the neat PLA, could indicate that the mechanical properties of the composites are better. This will be verified through the tensile testing and DMA analysis. The crystallinity calculated from the cooling cycle and the second heating cycle was found to be lower for the filaments and the FDM specimens, when compared with the granules for both cycles.

4.4 Oscillatory rheology

4.4.1 Introduction

The oscillatory rheology tests were carried out to help understand the rheological behaviour of the composite material during the different processing steps. Especially the behaviour at high sheer rates is important, as this can be linked to the printing speed of the FDM process. For each composite the following data was obtained with the oscillatory plate-plate rheometer: the storage modulus (G'); the loss modulus (G"); the shift between the elastic and the loss modulus: the loss angle; and the complex viscosity (|η*|). The parameters of the Carreau-Yasuda model for the complex viscosity were determined using the results of the tensile tests and an Excel solver.

4.4.2 Results

In this section, the data obtained for the mixtures will be discussed. Figure 38, figure 39, figure 40 and figure 41 show the results for the average storage modulus, the average loss modulus, the loss angle and the complex viscosity of the mixtures. The averages for PLE 005, the extruded PLA and the PLA/HA 3% mixtures were taken from the repetition of the experiment for these mixtures.

Figure 38 shows the average storage modulus of the mixtures. In general, the storage modulus increases as the frequency increases, indicating that the stored energy increases; it can also be seen that the storage modulus is non-linear and dependent on the HA concentration in the mixtures. However, the addition of HA does not result in a simple increase or decrease of the storage modulus. PLA/HA 0.5% resulted in the highest storage modulus, followed by PLE 005 and the two also share overlapping intervals. PLE 005 was followed by the 1% mixture and the 3% mixture in that order respectively. Finally, the lowest storage moduli belonged to the extruded PLA and the 5% mixture, with the 5% mixture having the lowest storage modulus overall. In summary, the extrusion of PLA resulted in a reduced storage modulus when compared to the PLE 005, this was caused by the degradation of PLA. Adding HA to the extruded PLA resulted initially in a storage modulus higher than the extruded PLA for the 0.5% mixture, after which the storage modulus declined gradually with the addition of more HA. A high storage modulus is associated with a solid-like behaviour, hence why the decrease of the storage modulus with the addition of more HA is surprising. HA is already in a solid state, and expected to restrict movement, leading to a higher storage modulus. However, the storage modulus decreases gradually when more than 0.5% HA is added.

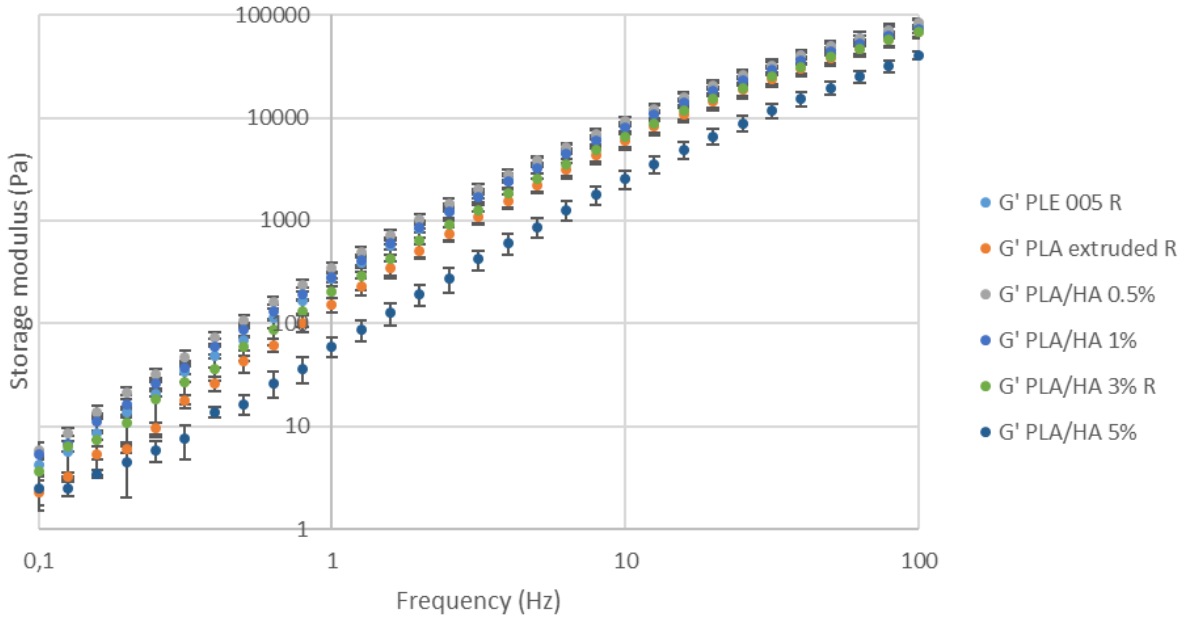

Figure 38 The average storage modulus of the mixtures.

Figure 39 shows the average behaviour of the loss modulus at different frequencies for all the mixtures. The loss modulus evolves in the same way: decreasing after the extrusion of PLA, followed by a recovery after the addition of 0.5% HA; and finally, a gradual decrease with the addition of more HA.

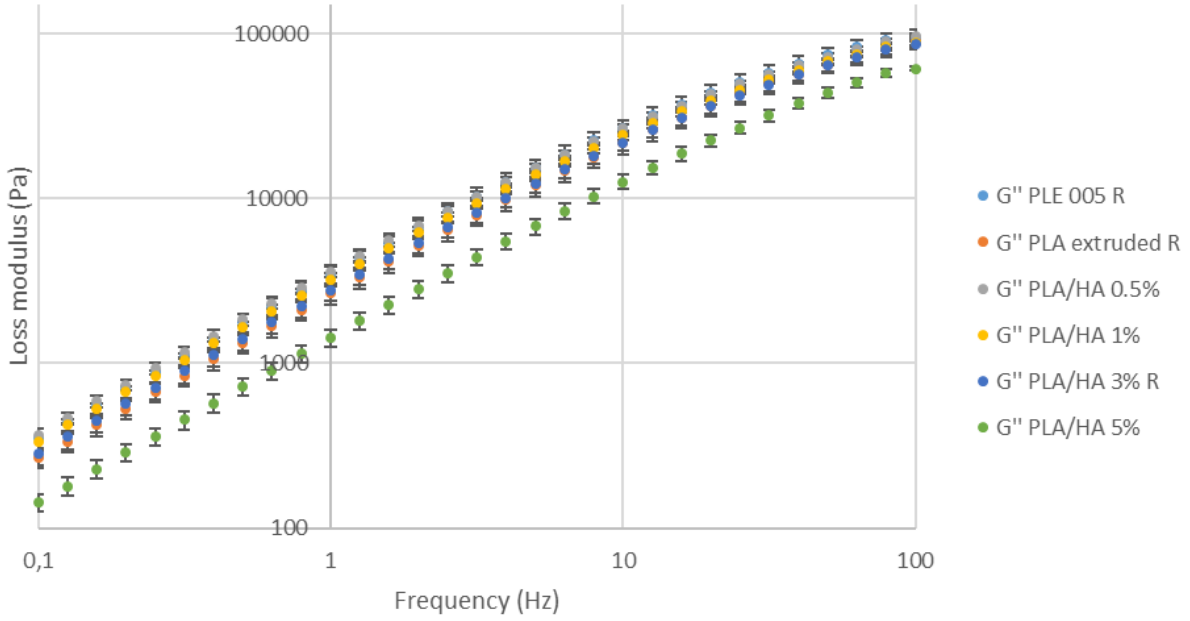

Figure 39 The average loss modulus of the mixtures.

The average loss angle of the mixtures at different frequencies is given by figure 40. The loss angle is the phase shift between the storage modulus and the loss modulus; and is a representation of the viscoelastic behaviour of the mixtures. In general, the loss angle evolves towards what looks like a platform at lower frequencies; while descending steadily for higher frequencies. At low frequencies, the loss angle approaches 90° indicating mainly viscous behaviour. While at higher frequencies, the material becomes more elastic. The highest phase shifts between the storage and loss modulus are found for the 5% mixture, while the lowest is found for the 0.5% mixture.

The phase shift increases with the extrusion of the PLA, this due to a lower molecular mass and a more viscous resulting behaviour. Additional HA results in a recovery of the phase shift. Both the 0.5% and the 1% mixture have loss angles lower than those of the PLE 005. The 3% mixture has a loss angle with values in between those of the PLE 005 and the extruded PLA. The loss angle thus indicate that the first additions of HA make the PLA more elastic, while an inclusion of 5% of HA makes the PLA more viscous.

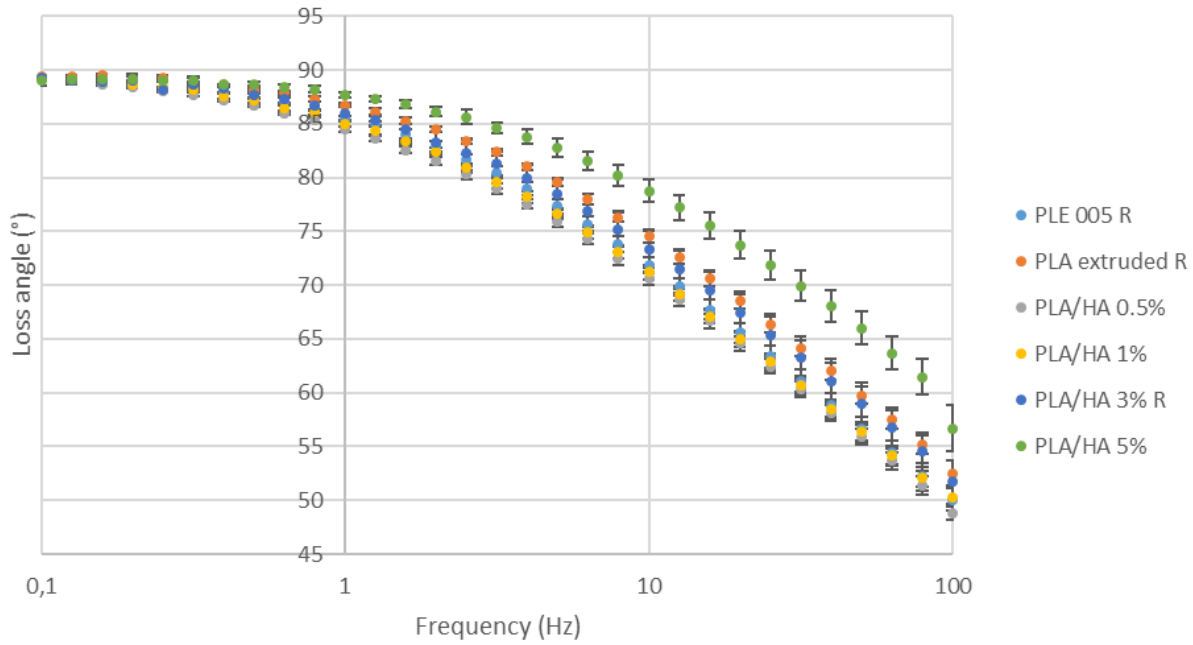

Figure 40 The average loss angle of the mixtures.

Figure 41 shows the average complex viscosity of the mixtures at different frequencies. The general behaviour is a Newtonian plateau at lower frequencies, followed by shear-thinning, characteristic for rheo-fluidifying or pseudo-plastic behaviour. The relaxation time corresponds to the length of the Newtonian plateau and differs for each mixture, as does the start of the pseudo-plastic behaviour, given that the start is the end of the plateau. The viscosity at zero shear (the plateau) decreases with the extrusion of PLA. The first addition of HA resulted in a thickening effect, the viscosity at zero shear increased, followed by a decreasing thickening effect when more HA was added, up to introduction of a thinning effect for the addition of 3% and more HA. Pavlovic et al. showed that the viscosity is the result of the diffusion of atoms or molecules in amorphous material [205]. Therefore, the decline in viscosity after extrusion could be the result of the degradation, resulting in a lower molar mass, which hindered diffusion. The first addition of HA, seems to facilitate the diffusion again and the gradual reduction of the viscosity with more HA could be the result of an HA saturation.

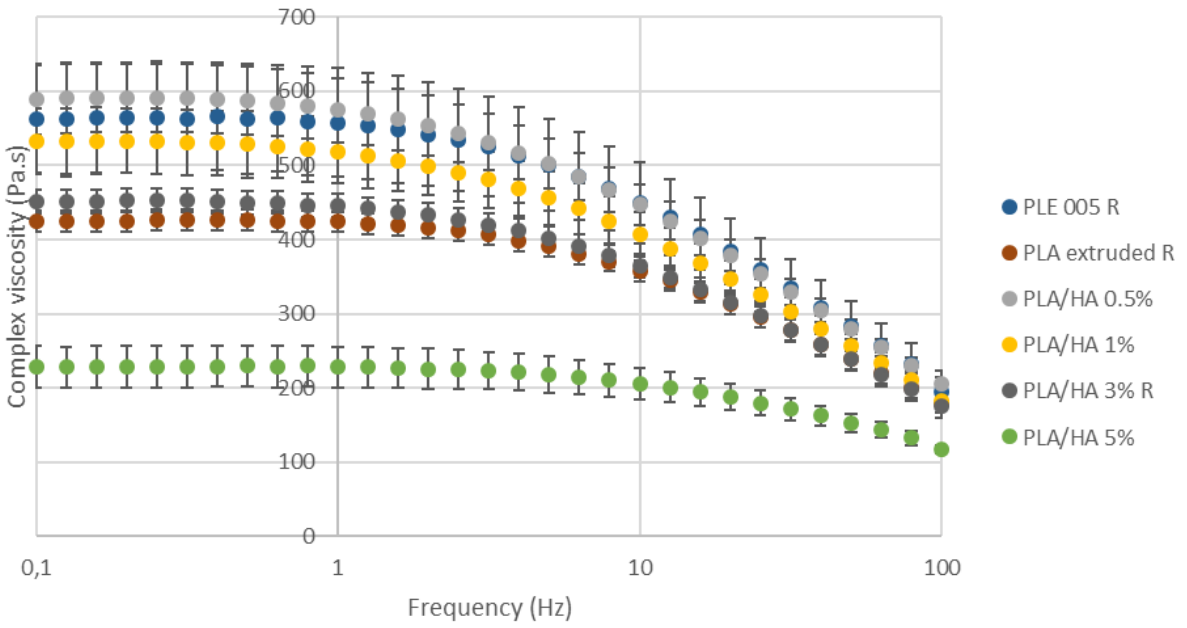

Figure 41 The average complex viscosity of the mixtures.

By supposing the Cox-Merz rule applied, it was possible to use the complex viscosity plotted against the frequency instead of the apparent viscosity plotted against the shear rate for the Carreau-Yasuda model. Table 38 contains the parameters, obtained using a solver, the model of each mixture and its fit. Each model requires a fitting higher than 0.9, this to ensure the fit of the model is not a coincidence. However, as shown in table 38, the fit is 1 or nearly one for all mixtures. The viscosity at zero shear (η_0) corresponds to the height of the Newtonian plateau, which follows the behaviour discussed in the previous paragraph and is also an indication for the molar mass. The relaxation time (λ) corresponds to the onset of the fluidification, which indicates that the fluidification starts the earliest for the PLE 005 and the latest for the extruded PLA. The Yasuda index (a), which determines the curve of the fluidification transition, is the highest for the extruded PLA and the lowest for the PLE 005, the 0.5% and the 1% mixture. A higher Yasuda index, corresponds to a more important curve. Finally, the index of the power law (n), is an indication for the sharpness of the shear-thinning effect. The lower n is, the more the viscosity decreases with shear rate. Therefore, the sharpest decrease corresponds to the PLE 005. Additionally, the extruded PLA has the least sharp decrease, with the sharpness increasing with the addition of 0.5% and 1% of HA, before decreasing again with the addition of more HA. This means that at a higher shear rate, viscosity will be lower for the composites, when compared to the extruded PLA. Note that the addition of filler often leads to greater viscosity, but in the case of HA there is an inverse effect, which is very interesting for the FDM process, as a high shear rate/high temperature combination will result in a decrease of nozzle clogging due to the lower viscosities found at high shear rates.

Table 38 The parameters of the Carreau-Yasuda model of the different mixtures.

nHA	η0 (Pa.s)	λ (s)	a	n	R^2
PLE 005 R	574,3	1,56E-02	0,82	0,018	0,998
0% Repeat	428,1	5,64E-02	1,12	0,540	1
0,5%	601,5	3,94E-02	0,82	0,374	0,999
1%	541,2	3,33E-02	0,82	0,332	1
3% Repeat	455,9	5,22E-02	0,98	0,494	1
5%	229,9	2,58E-02	1,05	0,482	0,999

4.2.4 Conclusion

Both the extrusion of PLA and the addition of HA influence the viscosity. The extrusion results in a reduction of the viscosity, due to the reduction of the molar mass, while the first addition of HA increases the viscosity of the extruded PLA, after which the viscosity decreases gradually with the addition of more HA. For all formulations, the viscosity decreased at higher frequencies due to shear-thinning behaviour. Using the Cox-Merz law, it can thus be said that the viscosity decreases at higher shear rates. This could mean that the viscosity decreases for higher printing speeds during the FDM process. Additionally, the viscosity also decreased with the addition of 3% and more HA, which could also help prevent nozzle clogging during the printing process.

4.5 Tensile tests

4.5.1 Introduction

Tensile tests were carried out for each nanocomposite and with two goals in mind. The first goal is the optimisation of the mechanical properties of the FDM printed specimen, in this case the optimisation meant maximising the mechanical properties, this to compensate for the loss in mechanical performance caused by the AM techniques. The second goal consisted of judging the impact of the FDM process, more specifically the temperature and the printing speed on the tensile properties. Injection moulded test specimens were created to verify if adding fillers in composites shaped by AM gives the same or better mechanical properties than neat PLA shaped by injection moulding. Additionally, the impact of the filler on the mechanical properties can also be compared between the two processes.

4.5.2 Design of experiments with printed specimens

Table 39 gives the Young modulus and ultimate strength of each condition for PLA/HA 0%. The printing temperatures and printing speed corresponding to each condition can be found in table 5 (Section 3.2.1.3.2). The values of each condition are very close, but the calculation of the p-values showed with good probability that the experimental points are not the same. This could be an indication that the printing speed and temperature do not result in varying mechanical properties within the studied domain. Upon examination of the printing quality of the samples, there were significant differences in quality as discussed in the result section of FDM (Section 4.1.3). For neat PLA, the highest quality was found for condition 5. However, condition 5 does not possess the highest Young modulus or ultimate strength. This indicates that the previously determined quality does not necessarily result in the highest mechanical properties as the bonding quality and/or the porosity inside may or may not be satisfying.

Table 39 Results tensile tests PLA/HA 0%.

PLA/HA 0%	E modulus (MPa)	Ultimate strength (MPa)
1	1169 ± 34	61,8 ± 0,8
2	1220 ± 15	62,0 ± 0,4
3	1206 ± 18	61,8 ± 1,1
4	1216 ± 18	60,8 ± 0,8
5	1193 ± 7	60,7 ± 1,2
6	1155 ± 10	57,3 ± 1,1
7	1214 ± 5	60,7 ± 0,1

Table 40 gives the coefficients of the theoretical model, the p-values of the coefficients (Young modulus and ultimate strength) and the coefficient of determination of the model. For the Young modulus, the coefficients are important in absolute value, indicating that the first and second order interactions and effects of the printing speed and temperature, and between them are not unneglectable. However, there seems to be no dominant coefficient, a_{11} and a_{22} both have a negative value indicating a maximum. Figure 42 shows that the maximum shifted towards higher printing temperatures and lower printing speed with its predicted value being 1221 MPa (70.3 mm/s; 232.3°C) for the young modulus. The response surface of the ultimate strength had the shape of a horse saddle (figure 43), which is confirmed by a_{11} and a_{22} having opposite signs, the dominance of the a_2 and a_{12} coefficient and the absence of a clear maximum within the studied domain. For both models the determination coefficient was found to be greater than 0.8 and the p-value of each coefficient was calculated. The p-values for the coefficients of the Young modulus were all very close to 0.1 with 0.1166 being the highest value and 0.0764 being the lowest value (apart from the p-value of a_0, but the coefficient of a_0 corresponds to the value of condition 7, which resulted in a p-value of 0,0019). The model of the young modulus was thus accepted as corresponding to the experimentations, given the low p-value and the high determination coefficient. For the ultimate strength, the p-values of the coefficients were well above 0.1 (apart for a_0 as mentioned previously), with a maximum p-value of 0.810, therefore the coefficients were suspected to be zero. For the ultimate strength, it can thus be concluded that there is no impact of both factors in this study field and therefore a model is unnecessary.

Table 40 Coefficients theoretical Doehlert model, p-values coefficients and the determination coefficient of PLA/HA 0%.

PLA/HA 0%	a0	a1	a2	a12	a11	a22	ε	R^2
Young Modulus (MPa)	1214,3	-19,7	22,3	30,3	-21,7	-20,5	4,0	0,9756
Ultimate strength (MPa)	60,70	-0,20	1,67	2,08	0,60	-0,53	-0,70	0,8124
P-value Young Modulus	0,002	0,117	0,103	0,076	0,106	0,112		
P-value Ultimate strength	0,007	0,810	0,235	0,192	0,525	0,562		

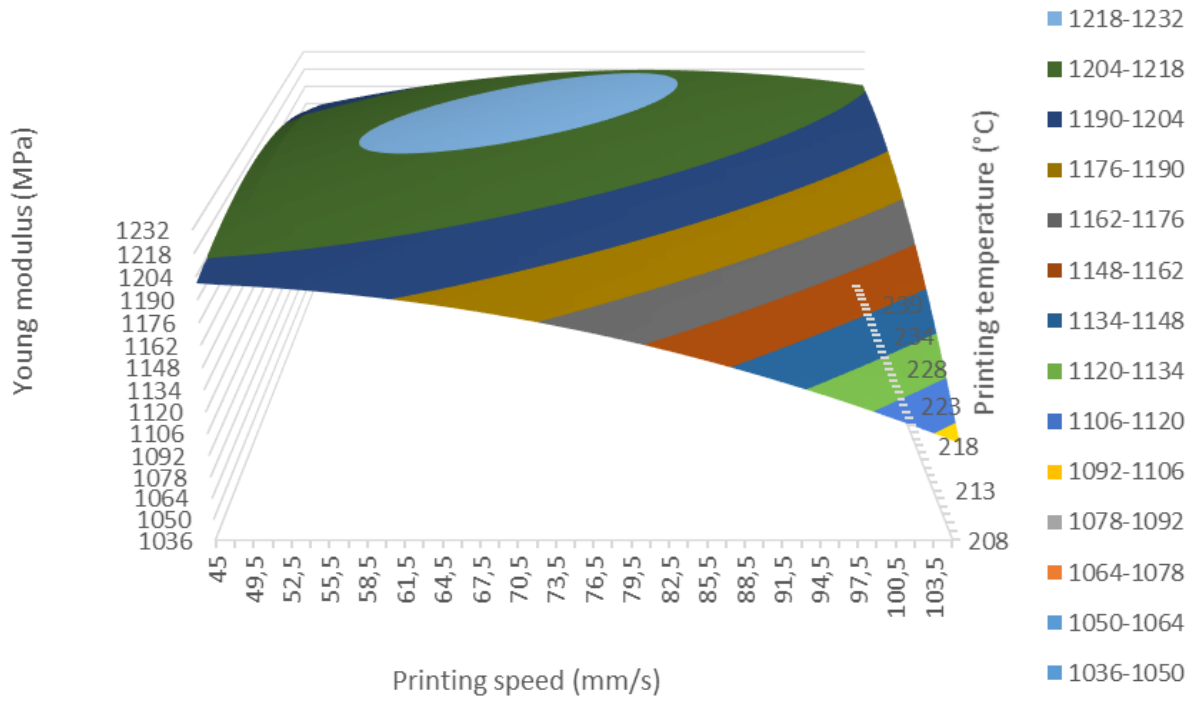

Figure 42 Response surface Young modulus PLA/HA 0%.

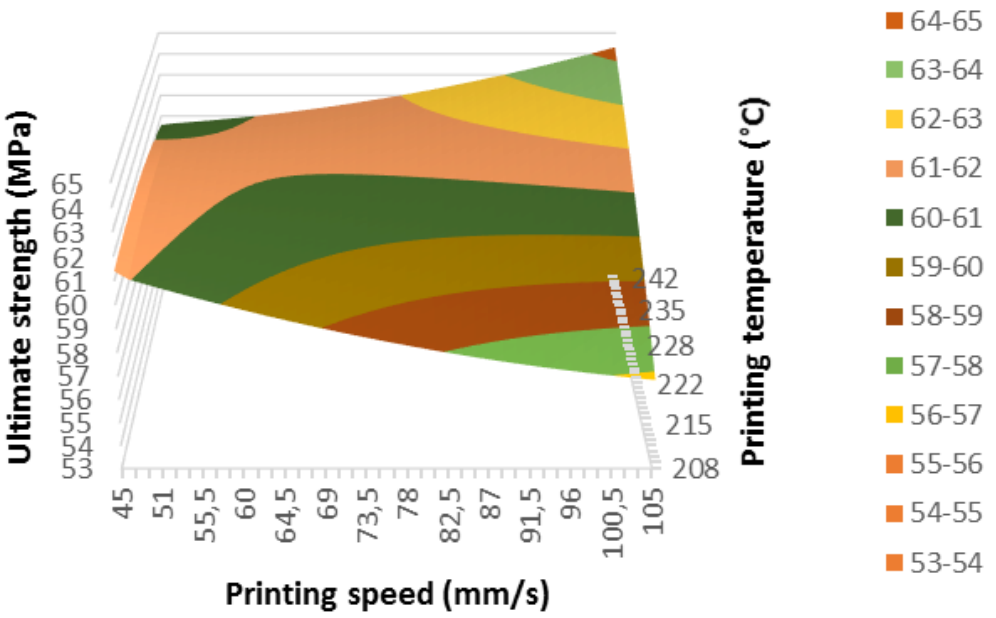

Figure 43 Response surface ultimate strength PLA/HA 0% (Horse saddle shape).

Table 41 shows the results of the tensile tests of PLA/HA 0.5%. Again, there is overlap between the intervals of individual points for both the young modulus and the ultimate strength. However, for the Young modulus there are less overlapping intervals and there is less of an overlap, compared to PLA/HA 0%. The opposite is true for the ultimate strength, as the overlap increases when compared to PLA/HA 0%. Additionally, the values of both the Young modulus and the ultimate strength are lower, the Young modulus does share the same evolution of its value across the different points, compared to the PLA/HA 0%.

Table 41 Results tensile tests PLA/HA 0.5%.

PLA/HA 0,5%	E modulus (MPa)	Ultimate strength (MPa)
1	1161 ± 5	58,3 ± 0,9
2	1213 ± 11	58,6 ± 1,7
3	1185 ± 14	59,7 ± 2,2
4	1169 ± 12	58,6 ± 1,4
5	1185 ± 12	59,9 ± 2,0
6	1148 ± 12	56,5 ± 2,8
7	1172 ± 12	59,4 ± 1,3

Table 42 shows the coefficients of the theoretical Doehlert model for the Young modulus of PLA/HA 0.5%, a_{11} and a_{22} have opposite signs and there is a prominent a_{12} coefficient, indicating the presence of a horse saddle shape in the response surface. A_2 and a_{12} indicate a dominance of a first order effect and the interaction between the printing speed and temperature. The theoretical model has a calculated determination coefficient of 1, which corresponds to a perfect fit. For each coefficient, the p-value was calculated and found to be below 0.01, indicating a very low probability that the coefficients are zero. For the ultimate strength, the values of the coefficients are all very low and the determination coefficient is smaller than 0.8. Therefore, the theoretical model does not correspond to the response of the material.

Table 42 Coefficients theoretical Doehlert model PLA/HA 0.5%.

PLA/HA 0,5%	a0	a1	a2	a12	a11	a22	ε	R^2
Young Modulus (MPa)	1172,10	-4,15	18,62	37,35	-7,40	16,77	-0,05	1,0000
Ultimate strength (MPa)	59,40	-0,85	0,55	1,33	-0,95	-0,65	-0,70	0,6301
P-value Young Modulus	0,001	0,007	0,002	0,001	0,004	0,002		

Table 43 gives the Young modulus and the ultimate strength of the printed PLA/HA 1% samples. The evolution of the Young modulus across the different points is different from PLA/HA 0% and PLA/HA 0.5%, which share the same evolution. The ultimate strength does evolve similarly to PLA/HA 0.5%, apart from the final value, which decreases for PLA/HA 1%. By comparing the values of PLA/HA 1% and PLA/HA 0.5%, the addition of more HA leads to different mechanical properties. Although the differences between the two composites are minimal for a lot of the points.

Table 43 Results tensile tests PLA/HA 1%.

PLA/HA 1%	E modulus (MPa)	Ultimate strength (MPa)
1	1209 ± 17	57,2 ± 2,9
2	1196 ± 20	58,5 ± 1,1
3	1199 ± 15	59,7 ± 1,1
4	1148 ± 11	57,4 ± 2,8
5	1151 ± 72	59,0 ± 3,5
6	1192 ± 47	56,2 ± 2,1
7	1185 ± 30	55,5 ± 2,6

Table 44 shows the coefficients of the theoretical Doehlert model of the Young modulus and ultimate strength of PLA/HA 1%. A horse saddle shape can be expected for the response surface of the Young modulus, given that the second order coefficients have opposite signs and the a_{12} coefficient is prominent. The absolute value of the first order coefficients and the interaction coefficient indicate that these relationships with and between the printing speed and temperature on the Young modulus are dominant. For the ultimate strength, a minimum can be found given that the signs of the second order coefficients are the same and positive. This minimum was predicted to be 55,41 MPa. The determination coefficients of the models are greater than 0.8, yet the calculation of the p-value resulted in multiple values being greater than 0.1, indicating that the probability that these coefficients are zero is rather high. However, at least one coefficient has a p-value smaller than 0.1 for both the Young modulus and the ultimate strength. The models can thus be kept.

Table 44 Coefficients theoretical Doehlert model PLA/HA 1%.

PLA/HA 1%	a0	a1	a2	a12	a11	a22	ε	R^2
Young Modulus (MPa)	1185,0	26,5	15,0	-25,5	-6,8	1,3	-4,0	0,9724
Ultimate strength (MPa)	55,50	-0,73	0,87	0,92	1,80	3,20	-0,63	0,8248
P-value Young Modulus	0,002	0,088	0,153	0,091	0,230	0,129		
P-value Ultimate strength	0,007	0,430	0,379	0,360	0,064	0,051		

Table 45 shows the results of the tensile tests of PLA/HA 3% samples. The values of the Young modulus do not share the same evolution as those of PLA/HA 0%, but there are some points with overlapping intervals. Similarly, the evolution of the ultimate strength is different, however, the ultimate strength values are on average 11% lower than those of PLA/HA 0%.

Table 45 Results tensile tests PLA/HA 3%.

PLA/HA 3%	E modulus (MPa)	Ultimate strength (MPa)
1	1239 ± 14	55,0 ± 1,5
2	1244 ± 9	54,1 ± 0,9
3	1206 ± 10	56,2 ± 2,3
4	1213 ± 14	52,7 ± 2,2
5	1174 ± 18	53,8 ± 1,4
6	1285 ± 18	52,7 ± 0,6
7	1169 ± 30	51,5 ± 1,8

Table 46 gives the coefficients of the theoretical Doehlert model of PLA/HA 3%. A minimum can be found for the Young modulus, as both second order coefficients are positive. Given that one goal of the experiment is the optimisation by maximum of the mechanical properties to reach a higher resistance for bone implant application, the chosen domain seems to be non-ideal. Although the optimisation is done with bone implant applications in mind, the main objective remains the expansion of the range of applicable materials in FDM by nanofiller incorporation. Figure 44 visualises the theoretical model of the Young modulus, and there is a minimum at lower temperatures and higher printing speeds. A maximum can be searched more easily thanks to the Doehlert method, with the use of the uniform space-filling principle. Instead of starting all over again and remaking a new matrix, Doehlert allows the re-usage of experimental points. However, the new points have to result in the creation of a new hexagon with the distance between neighbouring points being the same. However, given the lack of fit of the theoretical model, no conclusions can be drawn from it. The ultimate strength shares the same characteristics, both second order coefficients are positive and indicate the presence of a minimum. Again, no conclusions can be drawn from the model given the lack of fit.

Table 46 Coefficients theoretical Doehlert model PLA/HA 3%.

PLA/HA 3%	a0	a1	a2	a12	a11	a22	ε	R^2
Young Modulus (MPa)	1168,5	33,5	-2,7	-42,6	57,4	59,4	20,5	0,7533
Ultimate strength (MPa)	51,50	0,23	1,10	-0,58	2,35	2,82	-0,92	0,6627

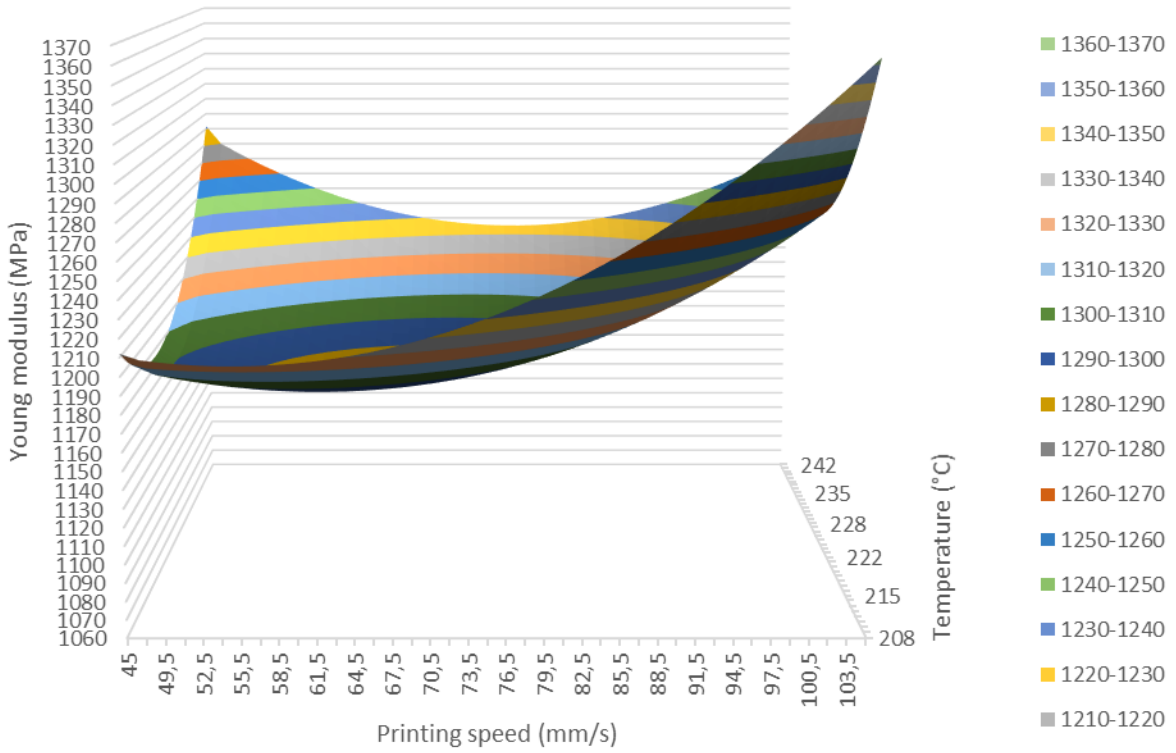

Figure 44 Response surface Young modulus PLA/HA 3%.

Table 47 shows the results of the tensile tests of PLA/HA 5% samples. The values of the young modulus are similar to those of PLA/HA 0%, but the evolution of the values for points 5-7 is different. For the ultimate strength, the values are on average 12% lower than those of PLA/HA 0%.

Table 47 Results tensile tests PLA/HA 5%.

PLA/HA 5%	E modulus (MPa)	Ultimate strength (MPa)
1	1197 ± 14	55,0 ± 2,5
2	1235 ± 14	54,1 ± 4,8
3	1215 ± 11	56,2 ± 3,0
4	1230 ± 9	52,7 ± 1,8
5	1242 ± 9	53,8 ± 1,8
6	1231 ± 19	52,7 ± 0,8
7	1185 ± 11	51,5 ± 1,1

Table 48 shows the coefficients of the theoretical Doehlert models of PLA/HA 5%. For both the Young modulus and the ultimate strength the second order coefficients are both positive indicating a minimum. For the Young modulus, the second order interaction appears to be dominant as both coefficients are substantially larger than the first order coefficients and the interaction coefficient. Most of the calculated p-values were substantially higher than 0.1 for the coefficients of the Young modulus, indicating that there is a high probability these coefficients are zero. However, the determination coefficient was still high enough, so the model was kept. For the ultimate strength, the determination coefficient is lower than 0.8 and thus the model was refused.

Table 48 Coefficients theoretical Doehlert model PLA/HA 5%.

PLA/HA 5%	a0	a1	a2	a12	a11	a22	ε	R^2
Young Modulus (MPa)	1185,3	-9,4	-6,3	18,0	28,1	51,4	6,9	0,8923
Ultimate strength (MPa)	51,5	0,23	1,10	-0,58	2,35	2,82	0,92	0,6627
P-value Young Modulus	0,003	0,381	0,505	0,219	0,143	0,079		

4.5.3 Results injection moulded specimens

In table 49, the Young modulus and the ultimate strength of the injection moulded tensile test specimens are displayed. The average Young modulus of the injection moulded specimens decreases with the first addition of HA, after which the modulus increases with each addition of HA. Note that the modulus for the specimens with 1% HA is already greater than that of the pure PLA. However, the variation on the Young moduli is quite high and multiple percentage have overlapping intervals. The ultimate strength increases with the first addition of HA, after which it steadily decreases for each addition of HA except for the addition of 3%, which results in a minor recovery.

Table 49 Young modulus and ultimate strength injection moulded tensile test specimens.

IM	Young modulus (MPa)	Ultimate strength (Mpa)
PLA/HA 0%	1414,4 ± 38,5	69,0 ± 1,7
PLA/HA 0,5%	1378,0 ± 34,4	69,8 ± 1,3
PLA/HA 1%	1425,1 ± 50,4	65,0 ± 1,1
PLA/HA 3%	1449,0 ± 15,7	66,0 ± 0,4
PLA/HA 5%	1491,7 ± 22,9	61,8 ± 0,4

Figure 45 shows the Young modulus of the printed and injection moulded specimen. For each concentration of HA, the modulus of the different Doehlert points is shown. The injection moulded specimens have much higher Young moduli. The Young modulus of the injection moulded samples decreases with the first addition, followed by a recovery with the addition of 1% of HA, a stabilisation for 3% HA as the intervals overlap again and finally an increase of the Young modulus for 5% of HA. The evolution of the FDM printed samples with the addition of HA differs from printing condition to printing condition with only condition (or point) 3 sharing a similar evolution with the injection moulded samples. In figure 46 the ultimate strength of the injection moulded specimens is compared with the FDM printed ones. As for the Young modulus, the ultimate strength of the injection moulded samples is higher for all concentrations regardless of the chosen Doehlert point. The FDM printing thus results in lower mechanical properties, which was expected. Additionally, the evolution of the ultimate strength with the addition of HA differs from the FDM process and the injection moulding process. For the injection moulding, the ultimate strength evolves in a stepwise fashion, having an overlapping interval between 0 and 0.5% HA and between 1 and 3% of HA, while decreasing in value. However for the FDM printed samples, the ultimate strength shares an overlapping interval between 0, 0.5 and 1%, after which the ultimate strength decreases with the addition of 3% of HA before having an overlapping interval again between 3 and 5% of HA.

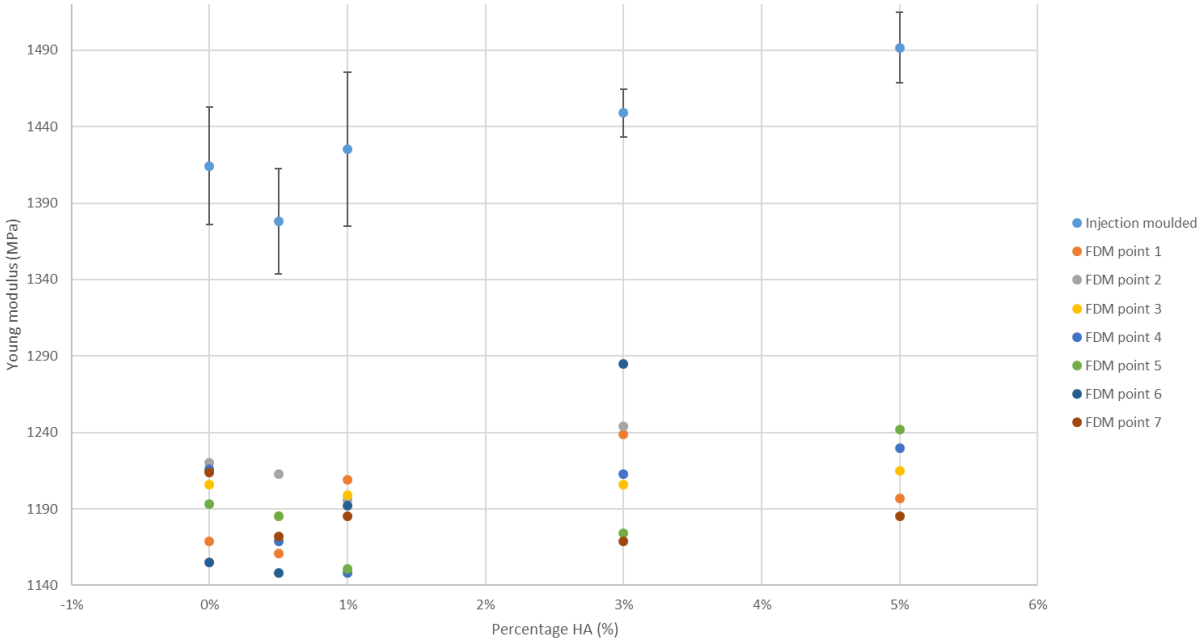

Figure 45 Comparison Young modulus between the injection moulded and printed tensile specimens for different concentrations of HA.

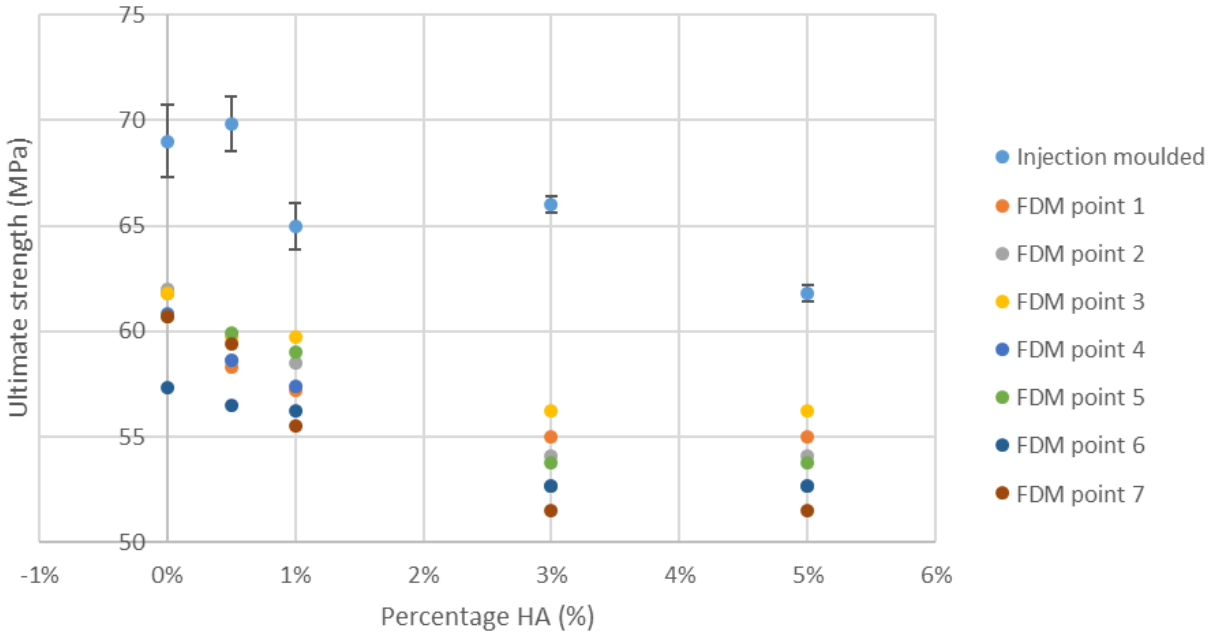

Figure 46 Comparison ultimate strength between the injection moulded and the printed tensile specimens for different concentrations of HA.

4.5.4 Conclusion

The overlap of value intervals between certain Doehlert points is a global trend that returns for most PLA/HA composites. However, the printing parameters do result in different mechanical properties. The impact of the filler on the Young modulus differs for the injection moulded and the FDM printed samples. For the Young modulus, only printing condition 3 shared some similarities in evolution with the injection moulded samples. The FDM printed samples did not all share a similar evolution for the Young modulus, while this was the case for the ultimate strength. The evolution of the ultimate

strength was, again, different for the injection moulded specimens. Additionally, the printing process introduced a lot of faults in the printed samples, which led to lower mechanical properties when compared to the injection moulded samples for both the Young modulus and the ultimate strength. No printing condition resulted in properties similar to those of the injection moulded samples. For the Young modulus, the closes properties for each concentration of HA were found for different Doehlert points. While for the ultimate strength, Doehlert point 3 resulted in the properties closest to those of the injection moulded samples for all concentrations of HA apart from 0.5%, for which condition 5 was the closest to the injection moulded specimens. Samples showed macro pores and micro pores. These were a direct result of the printing process as the raster lines left room for air gaps, this despite the selection of 100% filling during the printing process. The faults caused by the printing process are not necessarily bad as they can be used to control the resulting mechanical properties. However, more research is needed to better characterise the influence of all printing parameters on the mechanical properties.

4.6 Dynamic mechanical analysis

4.6.1 Introduction

In this section, the results of the dynamic mechanical analysis (DMA) will be discussed. Pressed and printed samples were tested for each formulation. The DMA was executed, firstly to study the thermomechanical properties given by the addition of HA in PLA. Secondly to characterise the differences between pressed and printed samples. The crystallinity in the pressed samples was the result of an annealing process, while the crystallinity in the printed samples was kept authentic to the printing process. The annealing process for the pressed samples was necessary to control the differences in crystallinity rate caused by a variant cooling speed.

4.6.2 Results

The results of the dynamic mechanical analysis are discussed in this section. The relaxation peak of the storage modulus (E’), the peak of the loss modulus (E”) and the Tangent Delta (tan δ) peak are given for the pressed and FDM printed samples as well as the onset and endset of the relaxation peak of the storage modulus and the onset and endset of the loss modulus peak and Tangent Delta peak. Delta corresponds to the phase shift between the storage modulus and loss modulus, as discussed previously in the oscillatory rheology section ($\delta = \tan^{-1}(E"/E')$). Tangent Delta thus corresponds to the ratio of E”/E’ and is also known as the damping factor.

First, the results of the storage modulus are given. The storage modulus (E’) is the contribution of the elastic components of the composite and related to its load-bearing capacity, it indicates the viscoelastic rigidity of the composites and is proportional to the energy stored after every deformation cycle [206]. In other words, the storage modulus reveals the capability of a material to store mechanical energy and resist deformation [207]. The general behaviour of the storage modulus was found to consist of a gradual decrease, followed by a rapid decrease until a plateau is reached. Finally, the storage modulus increases again. In the literature, this behaviour has been described as the glassy state (below 45°C), the glass transition (approximately 50-80°C) and the rubber plateau (Between 80 and 100°C) [208] [209] [210]. In the glassy state, the storage modulus is predominantly determined by the strength of the intermolecular forces and the way the polymer chains are aligned [211]. The high

storage modulus in the glassy state can be linked to the components being highly immobile, close and tightly packed [206]. The storage modulus of PLA decreases rapidly during the glass transition, this is typical for amorphous thermoplastics and is due to the amorphous phase, which increases at higher temperatures [211]. The decrease in storage modulus is a result of the PLA softening during the heating, which leads to an increase in chain segment movements and a decreasing elasticity without a distinct softening point [211] [212]. The increase in the storage modulus above 100°C is associated with the cold crystallisation of PLA during the heat scanning process [212].

Table 50 shows the onset and end of the rapid decrease of the storage modulus (the glass transition). Immediately it can be seen that there is a difference between the pressed and the FDM printed samples. For all formulations, the FDM printed samples have a much smaller temperature interval in which the glass transition occurs and the rubber plateau is reached, additionally, the onset and endset of the glass transition in a formulation are at lower temperatures. For the FDM printed samples, the onset of the glass transition gradually decreases in temperature with the addition of HA, this supplements the results of the DSC analysis, which indicated a plateau (due to high standard deviation) followed by a decrease in the onset temperature with the addition of 5% of HA. The end temperature of the glass transition of FDM samples decreases with the addition of 0.5% HA, then stays at the same temperature (around 59°C) when more HA is added. Pressed samples have a glass transition onset temperature that initially decreases with the addition of HA, followed by a slight recovery when 3% of HA is added, after which the temperature stabilises. The pressed samples have a similar behaviour for the onset and end of their glass transition, note that when 3% of HA is added, the temperature of the glass transition end is higher than that of pure PLA. The evolution of the onset and end temperature of the FDM samples differs from that of the pressed samples.

Table 50 Onset and end rapid decrease storage modulus.

Storage modulus		Onset		End		Interval
		Temperature (°C)	Storage modulus (MPa)	Temperature (°C)	Storage modulus (MPa)	Temperature (°C)
PLA/HA 0%	FDM	60,02 ± 0,16	1994,2 ± 200,6	66,96 ± 0,19	234,6 ± 30,4	6,94 ± 0,35
	CARVER	67,01 ± 1,10	1785,8 ± 39,0	84,63 ± 0,40	491,9 ± 30,0	17,62 ± 1,50
PLA/HA 0,5%	FDM	59,33 ± 0,07	2205,3 ± 229,2	66,00 ± 0,26	274,0 ± 28,7	6,67 ± 0,33
	CARVER	64,98 ± 0,89	1788,6 ± 77,1	84,09 ± 0,48	465,7 ± 33,3	19,11 ± 1,37
PLA/HA 1%	FDM	59,24 ± 0,23	2266,3 ± 76,8	66,03 ± 0,06	266,7 ± 16,8	6,79 ± 0,29
	CARVER	62,85 ± 0,23	1881,6 ± 77,3	83,65 ± 0,06	464,4 ± 18,1	20,80 ± 0,29
PLA/HA 3%	FDM	58,97 ± 0,24	2183,3 ± 120,0	65,74 ± 0,10	259,8 ± 7,5	6,77 ± 0,34
	CARVER	65,89 ± 0,74	1826,0 ± 58,2	86,38 ± 0,82	451,9 ± 15,5	20,49 ± 1,56
PLA/HA 5%	FDM	58,95 ± 0,11	1852,9 ± 106,6	66,54 ± 0,43	225,4 ± 14,3	7,59 ± 0,54
	CARVER	64,98 ± 0,82	1864,8 ± 113,4	84,72 ± 0,67	585,6 ± 25,6	19,74 ± 1,49

The differences between the glass transition of FDM printed and pressed samples could be due to the processing differences between the two. During the FDM process, the composites are only air quenched and there is no additional annealing process. For the pressed samples, there was an annealing step, allowing crystallisation. Therefore, the differences could be a result of a difference in crystallinity. DSC analysis showed that FDM samples had a maximum starting crystallinity of 8.71% for PLA/HA 0.5% and were mostly amorphous. The pressed samples did not undergo a DSC analysis; therefore, the effects of the crystallinity are only a hypothesis. The presence of filaments in the FDM specimens could also influence the glass transition, given that the pressed samples were made by pressing granules in heated moulds, potentially allowing for a more random crystal growth, while the FDM filaments could have resulted in an orientation of the polymer chains.

A remarkable trend was observed, the onset of the storage modulus of the FDM printed samples was higher than that of the pressed samples for the same formulation. This despite the FDM printed samples having a porous mesostructure and the pressed samples undergoing a heat treatment to maximise crystallinity, as a higher crystallinity results in a higher storage modulus [206]. A possible explanation for this could be the forced alignment invoked by the FDM printing process, which might have a reinforcing effect. During the FDM printing of the samples, the crossed raster pattern was aligned with the length and the width of the sample. This in turn could restrict bending invoked by the DMA analyser. The porosity of the FDM samples was not determined, but was estimated to be 10% or more. This could be verified with tomographic analysis. Note that the porosity in the FDM process is highly dependent on the printing process. The higher storage modulus could also be due to the test frequency being too high and resulting in the material to behave stiffer than it can be, as described for composites containing fibres by Chen et al. [207]. In this case the printing pattern could be considered as a multitude of fibres. These "fibres" are tightly packed in the contour lines. Annealing the FDM specimens could also be interesting for further research, as the annealing process removes stress from the aligned polymer chains. However, other phenomena could occur, such as bonding between the filaments, porosity reduction etc.

Table 51 gives information regarding the peak of the storage modulus. Only the values for the FDM printed samples are given. For the samples shaped with the Carver press, there was no peak in the storage modulus, as was the case for PLA/HA 5%. The storage modulus of PLA/HA 5% instead levels out in the area where the peak occurs for the other FDM composites, no plateau is created however. The peak occurs earlier when hydroxyapatite is added to the polymer matrix. Additionally, the peak value appears to increase with the addition of 0,5% and 1% of HA and then decreases with the addition of more HA. Yet, the standard deviation on the peak value is quite high, causing overlapping storage modulus intervals for the concentrations that display the peak. In the literature, the appearance of a peak in the storage modulus has been ascribed to the relaxation of internal stresses frozen in the polymer during sample preparation via melt-quenching, which is the case for FDM printed samples as they are quenched by air [213] [214] [215] [216] [217]. The effect has been observed to decrease with the filling, which seems to correspond with the results, as the peak becomes less pronounced with the addition of HA [213]. The peak does not appear for pressed samples, as the effect is decreased or damped totally by thermomechanical history (aging, crystallisation, orientation, or plasticisation) and the pressed samples underwent an annealing process [216]. The pressed samples received a heat treatment prior to the DMA tests to maximise crystallinity, which in this case led to the total dampening of the effect. Figure 47 shows the storage modulus in function of the temperature, for the different composites representative curves are shown.

Table 51 Peak storage modulus FDM samples.

Peak storage modulus		Temperature °C	Storage Modulus MPa
PLA/HA 0%	FDM	57,02 ± 0,35	2203,3 ± 227,9
PLA/HA 0,5%	FDM	56,40 ± 0,97	2420,3 ± 263,6
PLA/HA 1%	FDM	56,45 ± 0,14	2511,3 ± 83,2
PLA/HA 3%	FDM	56,31 ± 0,24	2420,0 ± 116,0
PLA/HA 5%	FDM	/	/

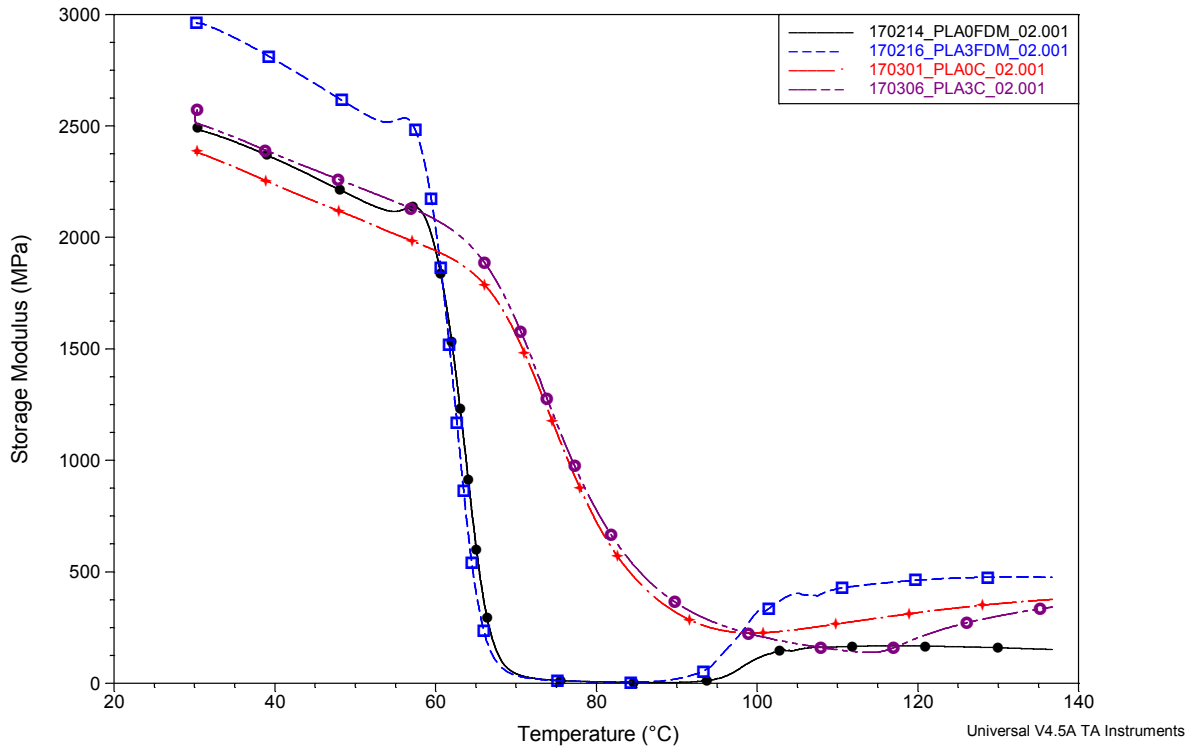

Figure 47 Storage moduli pressed (red: neat PLA; purple: PLA/HA 3%) and FDM printed (black: neat PLA; blue: PLA/HA 3%) samples.

Table 52 shows the temperatures at which the rubber plateau and the cold crystallisation begin for the FDM printed samples. The cold crystallisation increases the height of the rubber plateau, due to the reinforcing effect of the crystalline phase. For the pressed samples, there was no cold crystallisation. This is more than likely a result of the annealing process. If the annealing resulted in a higher crystallinity, the amount of amorphous phase would decrease. Due to the reduced amorphous phase, the glass transition is less significant as there is less material which undergoes this transition. Additionally, the increased crystallinity could also result in a restriction of the movement of the amorphous material. This in turn would result in a wider temperature range in which the glass transition takes place, due to the slow kinetic of the transition.

Table 52 End glass transition and onset cold crystallisation storage modulus.

Storage modulus		End glass transition	Onset cold crystallisation
		Temperature (°C)	Temperature (°C)
PLA/HA 0%	FDM	66,96 ± 0,19	95,58 ± 0,69
PLA/HA 0,5%	FDM	66,00 ± 0,26	92,15 ± 0,46
PLA/HA 1%	FDM	66,03 ± 0,06	94,08 ± 0,93
PLA/HA 3%	FDM	65,74 ± 0,10	93,42 ± 0,14
PLA/HA 5%	FDM	66,54 ± 0,43	91,43 ± 0,18

Table 53 gives the minimum values of the storage modulus of the FDM specimens in between the end of the glass transition and the beginning of the cold crystallisation. The minimum storage modulus approaches zero for all the mixtures. The minimum value increases with the addition of HA, but does not vary inter HA formulations. All HA formulations have overlapping intervals, when considering the standard deviation.

Table 53 Minimum storage modulus in between the end of the glass transition and the beginning of the cold crystallisation.

Minimum Storage modulus		Temperature (°C)	Storage Modulus (MPa)
PLA/HA 0%	FDM	87,30 ± 1,08	4,2 ± 0,5
PLA/HA 0,5%	FDM	84,71 ± 0,51	5,3 ± 0,2
PLA/HA 1%	FDM	86,06 ± 0,19	3,3 ± 2,8
PLA/HA 3%	FDM	84,64 ± 0,54	5,0 ± 0,2
PLA/HA 5%	FDM	83,14 ± 0,29	7,6 ± 3,6

Table 54 gives the storage moduli at the end of the measurement for both the pressed and FDM printed samples. The storage modulus of both samples recovered during the cold crystallisation process. There is a large standard deviation for both the pressed and the FDM printed samples. By comparing the averages, it is found that the storage modulus increases from 0-3% of HA for FDM printed samples and then decreases again with the worst modulus belonging to the composites with 5% HA. The pressed samples on the other hand seem to be less affected by the varying HA concentrations. The average storage modulus decreases with the addition of more HA apart from a small recovery when 5% HA is added, it can however be seen that all concentrations have overlapping intervals.

Table 54 Storage moduli at the end of the measurement.

End measurement		Temperature °C	Storage Modulus MPa
PLA/HA 0%	FDM	136,76 ± 0,07	351,9 ± 191,2
	CARVER	136,70 ± 0,07	443,4 ± 80,4
PLA/HA 0,5%	FDM	136,68 ± 0,08	434,6 ± 257,6
	CARVER	136,71 ± 0,08	383,8 ± 27,2
PLA/HA 1%	FDM	136,72 ± 0,04	521,8 ± 35,9
	CARVER	136,71 ± 0,05	367,7 ± 20,3
PLA/HA 3%	FDM	136,65 ± 0,06	348,5 ± 110,2
	CARVER	136,72 ± 0,04	355,3 ± 29,9
PLA/HA 5%	FDM	136,71 ± 0,12	168,0 ± 9,2
	CARVER	136,69 ± 0,05	387,0 ± 42,6

The loss modulus represents the viscous response of materials and is related to the amount of energy dissipated due to viscous motions inside the material itself [206]. It is a measure of the energy dissipated or lost as heat per cycle of sinusoidal deformation [218]. Usually the loss modulus increases and then decreases with increasing temperatures. The temperature at which the maximum heat dissipation occurs corresponds to the glass transition temperature (T_g) [206] [219].

Table 55 contains the temperatures and corresponding loss moduli of the onset and end of the loss modulus peak for all composites. The loss moduli of the pressed samples are much higher than those of the FDM printed samples. An explanation for this can be found in the loss modulus corresponding to the viscous response of materials. The viscous response can be linked to the quantity of amorphous phase in the composites. Given that the pressed samples were crystallised, they contain much less amorphous phase. Besides a reinforcing effect, the crystalline phase also reduces the viscous fraction. Additionally, the pressed samples have a much broader peak as the temperature interval is higher.

This is due to the lack of amorphous phase and the reduced chain mobility caused by the crystalline phase, which hinders the mobility and thus slows down the glass transition. Both the pressed and printed samples follow the same trend, the interval increases with the addition of more HA. However, the onset and end are found at lower temperatures for the printed samples. The corresponding loss moduli increase from 0-1% HA and then decrease when more HA is added for the printed samples. Whilst the onset loss moduli of the pressed samples simply increase when more HA is added and the end moduli follow the same pattern as the printed samples except for the value of PLA/HA 5%, which increases again.

Table 55 Onset and end peak loss modulus.

Loss modulus		Onset		End		Interval
		Temperature (°C)	Loss modulus (MPa)	Temperature (°C)	Loss modulus (Mpa)	Temperature (°C)
PLA/HA 0%	FDM	59,25 ± 0,22	142,3 ± 11,8	69,70 ± 0,19	106,0 ± 10,2	10,45 ± 0,41
	CARVER	63,09 ± 0,67	47,9 ± 6,1	93,21 ± 0,50	58,5 ± 2,1	30,12 ± 1,17
PLA/HA 0,5%	FDM	56,97 ± 0,16	148,8 ± 19,7	68,85 ± 0,31	116,2 ± 14,5	11,88 ± 0,47
	CARVER	60,81 ± 0,56	48,8 ± 2,4	91,50 ± 0,24	61,8 ± 2,7	30,69 ± 0,80
PLA/HA 1%	FDM	56,60 ± 0,21	158,5 ± 6,7	68,81 ± 0,07	120,6 ± 5,3	12,21 ± 0,28
	CARVER	59,05 ± 0,36	50,1 ± 4,9	90,95 ± 0,26	61,0 ± 2,4	31,90 ± 0,62
PLA/HA 3%	FDM	56,29 ± 0,16	151,9 ± 5,2	68,56 ± 0,06	116,9 ± 4,8	12,27 ± 0,22
	CARVER	61,72 ± 0,09	54,6 ± 4,8	93,92 ± 0,41	57,5 ± 0,7	32,20 ± 0,50
PLA/HA 5%	FDM	56,54 ± 0,17	121,2 ± 4,0	69,48 ± 0,59	95,2 ± 7,4	12,94 ± 0,76
	CARVER	60,34 ± 0,36	61,1 ± 6,5	93,33 ± 0,63	65,0 ± 3,7	32,99 ± 0,99

Table 56 contains the temperature and the loss modulus values corresponding to the loss modulus peaks of the different formulations. Again, the temperatures and loss moduli of the printed samples are lower than the pressed samples, due to more crystallised material for the pressed samples. For both the printed and the pressed samples, the loss moduli increase from 0-1% HA and then decrease. The temperatures on the other hand are rather stable, for the printed samples the loss modulus peak shifts to lower temperatures, but shifts back to a higher temperature when 5% of HA is added. The peak of the pressed samples also shifts to lower temperatures, but recovers faster. With the addition of 3%, the peak shifts back to higher temperatures and with the addition of 5% a minimal shift to lower temperatures occurs, although the variance is rather high for this composite. This is visualised in figure 48.

Table 56 Peak loss modulus for the pressed and printed composites.

Peak loss modulus		Temperature (°C)	Loss Modulus (MPa)
PLA/HA 0%	FDM	64,00 ± 0,25	582,1 ± 56,6
	CARVER	75,60 ± 0,15	180,9 ± 8,8
PLA/HA 0,5%	FDM	63,07 ± 0,10	630,1 ± 79,1
	CARVER	73,66 ± 0,37	200,8 ± 5,0
PLA/HA 1%	FDM	63,01 ± 0,06	657,5 ± 21,7
	CARVER	72,45 ± 0,40	201,5 ± 8,1
PLA/HA 3%	FDM	62,82 ± 0,08	637,7 ± 28,7
	CARVER	74,81 ± 0,43	179,6 ± 6,3
PLA/HA 5%	FDM	63,26 ± 0,23	504,6 ± 21,3
	CARVER	74,35 ± 1,01	173,1 ± 9,2

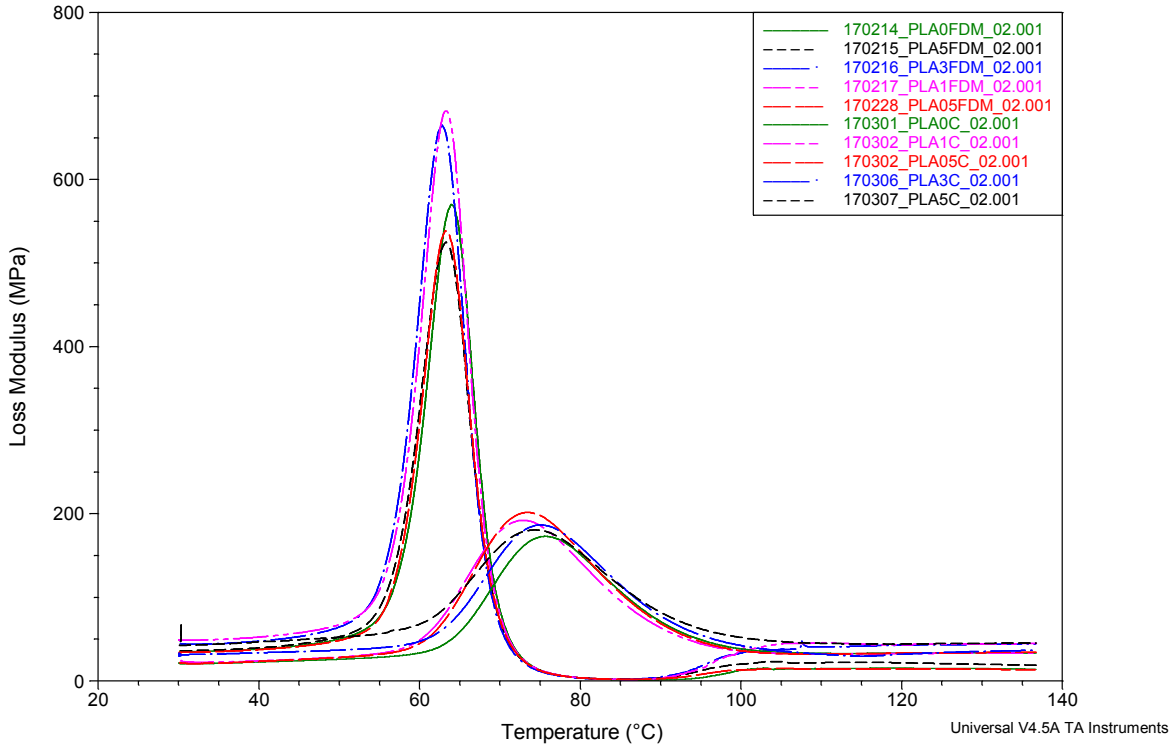

Figure 48 Loss moduli PLA/HA composites.

Table 57 shows the minimum loss moduli of the formulations and at which temperature the minimum loss moduli were obtained. Immediately, the difference between the printed and pressed samples becomes apparent. The printed samples have their minimum loss moduli after their loss modulus peaks, while the pressed samples attain their minimum loss moduli at the beginning of the measurement. Additionally, the loss moduli of the printed samples are quasi zero.

Table 57 Minimum loss moduli composites and corresponding temperatures.

Mininmum Loss modulus		Temperature (°C)	Loss Modulus (MPa)
PLA/HA 0%	FDM	87,14 ± 0,77	1,3 ± 0,2
	CARVER	31,43 ± 1,39	22,9 ± 2,0
PLA/HA 0,5%	FDM	85,06 ± 0,71	1,9 ± 0,1
	CARVER	30,71 ± 0,27	22,0 ± 1,7
PLA/HA 1%	FDM	85,95 ± 0,18	1,5 ± 0,1
	CARVER	32,17 ± 0,60	25,6 ± 3,1
PLA/HA 3%	FDM	85,51 ± 0,73	1,7 ± 0,2
	CARVER	30,50 ± 0,71	28,3 ± 1,6
PLA/HA 5%	FDM	85,75 ± 0,24	2,8 ± 1,1
	CARVER	30,86 ± 0,56	32,0 ± 9,0

Table 58 contains the final loss moduli, recorded at the end of the experiment. The loss modulus of each composite is higher than the minimum value. The evolution of the loss moduli with the addition of HA varies for the printed and pressed samples. Printed samples displayed an increase in loss moduli from 0-1% HA and then a decrease with the addition of more HA. In pressed samples, the loss moduli decreased initially, but then increased for 1-5% added HA.

Table 58 Loss moduli at the end of the experiment.

End measurement		Temperature °C	Loss Modulus MPa
PLA/HA 0%	FDM	136,76 ± 0,07	27,7 ± 13,4
	CARVER	136,70 ± 0,07	39,74 ± 8,47
PLA/HA 0,5%	FDM	136,68 ± 0,08	35,7 ± 20,1
	CARVER	136,71 ± 0,08	34,27 ± 2,00
PLA/HA 1%	FDM	136,72 ± 0,04	42,4 ± 2,8
	CARVER	136,71 ± 0,05	34,50 ± 2,09
PLA/HA 3%	FDM	136,65 ± 0,06	33,6 ± 9,2
	CARVER	136,72 ± 0,04	38,09 ± 1,81
PLA/HA 5%	FDM	136,71 ± 0,12	17,9 ± 0,9
	CARVER	136,69 ± 0,05	43,04 ± 4,55

The tan δ or damping factor corresponds to the ratio of loss modulus to storage modulus, this is the dissipating energy expressed in terms of the recoverable energy. δ is the phase difference between the dynamic stress and the dynamic strain. The damping properties of a material represent its capacity to reduce the transmission of vibration caused by mechanical disturbances to a structure [220]. Much of the energy used to deform a material during DMA testing is dissipated directly into heat [218]. Increasing the crystallinity of a material would reduce the height of the tan δ peak and a peak shift can be attributed to a mobility restriction in the amorphous domains [221]. Nguyen et al. mention the existence of two different amorphous phases (Free and constrained) [221]. Crystalline lamella start growing in the pure amorphous matrix, giving rise to mobility-restricted amorphous regions [221]. This in turn could be interpreted as an increase in the relaxation time of the molecular chains motion [221]. During the glass transition, the long-range polymer chain acquires mobility and therefore dissipates a great amount of energy through viscous movement, which is shown by the tan δ peak [222]. Reducing the number of mobile chains during the glass transition thus results in a depression in tan δ values [222]. Previous studies with a PHBHV/HA nanocomposite found that the tan δ peak of the polymer dropped when the filler content was increased and a certain broadening of the peak was observed [207]. This effect was attributed to the reinforcing effect of the homogeneously dispersed hydroxyapatite, which hinders the mobility of the polymer chains in the amorphous phase [207]. Zhang et al. considered the broadening of the tan δ peak at higher temperatures as evidence for soft segment mobility and the interaction between their nanosilica surface and EVA [223].

Table 59 shows the temperatures and the corresponding tan δ values of the onset and end of the tan δ peak. Again, the temperature interval for the pressed samples is much bigger, indicating a broader peak. The printed samples have much closer temperature onset and end values than the pressed samples. Furthermore, the tan δ values at the end of the peak are much higher for the printed values, indicating a bigger lag phase and thus a higher viscous part compared to elastic part. This indicates an increase of the viscous part compared to the elastic part.

Table 59 Onset and end tan δ peak.

Tangent delta		Onset		End		Interval
		Temperature (°C)	Tan delta	Temperature (°C)	Tan delta	Temperature (°C)
PLA/HA 0%	FDM	62,78 ± 0,12	0,39 ± 0,01	78,55 ± 0,46	0,62 ± 0,01	15,77 ± 0,58
	CARVER	65,50 ± 0,38	0,04 ± 0,01	106,28 ± 2,54	0,13 ± 0,01	40,78 ± 2,92
PLA/HA 0,5%	FDM	61,62 ± 0,06	0,34 ± 0,02	78,94 ± 0,69	0,57 ± 0,02	17,32 ± 0,75
	CARVER	62,96 ± 0,51	0,04 ± 0,01	108,44 ± 3,04	0,13 ± 0,01	45,48 ± 3,55
PLA/HA 1%	FDM	61,92 ± 0,13	0,39 ± 0,01	77,95 ± 0,12	0,60 ± 0,01	16,03 ± 0,25
	CARVER	61,40 ± 0,38	0,036 ± 0,01	111,81 ± 1,51	0,13 ± 0,01	50,41 ± 2,89
PLA/HA 3%	FDM	61,64 ± 0,14	0,40 ± 0,01	78,18 ± 0,16	0,63 ± 0,01	11,77 ± 0,30
	CARVER	64,24 ± 0,29	0,039 ± 0,01	120,55 ± 4,32	0,13 ± 0,01	56,31 ± 4,61
PLA/HA 5%	FDM	61,48 ± 0,37	0,31 ± 0,06	79,96 ± 0,31	0,56 ± 0,04	18,48 ± 0,68
	CARVER	63,07 ± 0,60	0,04 ± 0,01	101,55 ± 1,65	0,14 ± 0,01	38,48 ± 2,25

Table 60 gives the temperature and tan δ value of the peak maximum for the pressed and printed samples. Not only do the pressed samples have their peak maximum at a much higher temperature than the printed samples, the corresponding tan δ are much lower. Tan δ decreases from 0-0.5%, increases for 0.5-1%, remains constant for 1-3% (same value as the 0%) and decreases again for 5% HA for the printed samples. While the tan δ of pressed samples remained quasi constant except for the addition of 5% of HA, which led to a decrease in its value. The lowered peak can be explained by the higher crystallinity of the pressed samples, while the peak shift to higher temperatures can be attributed to a mobility restriction in the amorphous domains following Nguyen et al. [221]. The broadening of the tan δ peak could also be an indication of interaction between the HA surface and PLA [102].

Table 60 Temperature and Tan δ values corresponding to the tan δ peak.

Peak Tan delta		Temperature (°C)	Tan Delta
PLA/HA 0%	FDM	69,49 ± 0,19	1,99 ± 0,03
	CARVER	86,21 ± 0,83	0,24 ± 0,01
PLA/HA 0,5%	FDM	68,81 ± 0,21	1,87 ± 0,09
	CARVER	84,97 ± 1,21	0,25 ± 0,01
PLA/HA 1%	FDM	68,69 ± 0,32	2,02 ± 0,01
	CARVER	84,01 ± 0,76	0,24 ± 0,01
PLA/HA 3%	FDM	68,50 ± 0,18	2,04 ± 0,03
	CARVER	85,46 ± 0,86	0,22 ± 0,01
PLA/HA 5%	FDM	69,09 ± 0,26	1,65 ± 0,22
	CARVER	82,89 ± 0,59	0,19 ± 0,01

For some of the printed composite samples (0%; 0.5% and 1% HA), a shoulder in the tan δ peak was observed. The temperatures at which this shoulder occurred and the corresponding tan δ value are given in table 61. One explanation for this shoulder could be the glass transition of the mobility-restricted amorphous regions. Another explanation could be that this is the start of the pre-crystallisation, which precedes the actual cold crystallisation. The pressed samples only showed peak broadening, except for one 3% composite sample, which did have a second peak. In the literature, a second peak was observed during the DMA analysis of resin composites and attributed to a thermal curing process [224]. However, it is very unlikely that PLA undergoes thermal curing. Instead, the

preceding thermal crystallisation process might have resulted in mobility restricted amorphous phases. Figure 49 gives a visual representation of the tan δ behaviour of pressed and printed samples.

Table 61 Temperatures and Tan δ values corresponding to the second Tan δ peak.

Peak 2 Tan delta		Temperature (°C)	Tan Delta
PLA/HA 0%	FDM	87,98 ± 0,92	0,32 ± 0,02
	CARVER	/	/
PLA/HA 0,5%	FDM	84,45 ± 1,53	0,37 ± 0,01
	CARVER	/	/
PLA/HA 1%	FDM	86,10 ± 0,18	0,31 ± 0,01
	CARVER	/	/
PLA/HA 3%	FDM	/	/
	CARVER	/	/
PLA/HA 5%	FDM	/	/
	CARVER	/	/

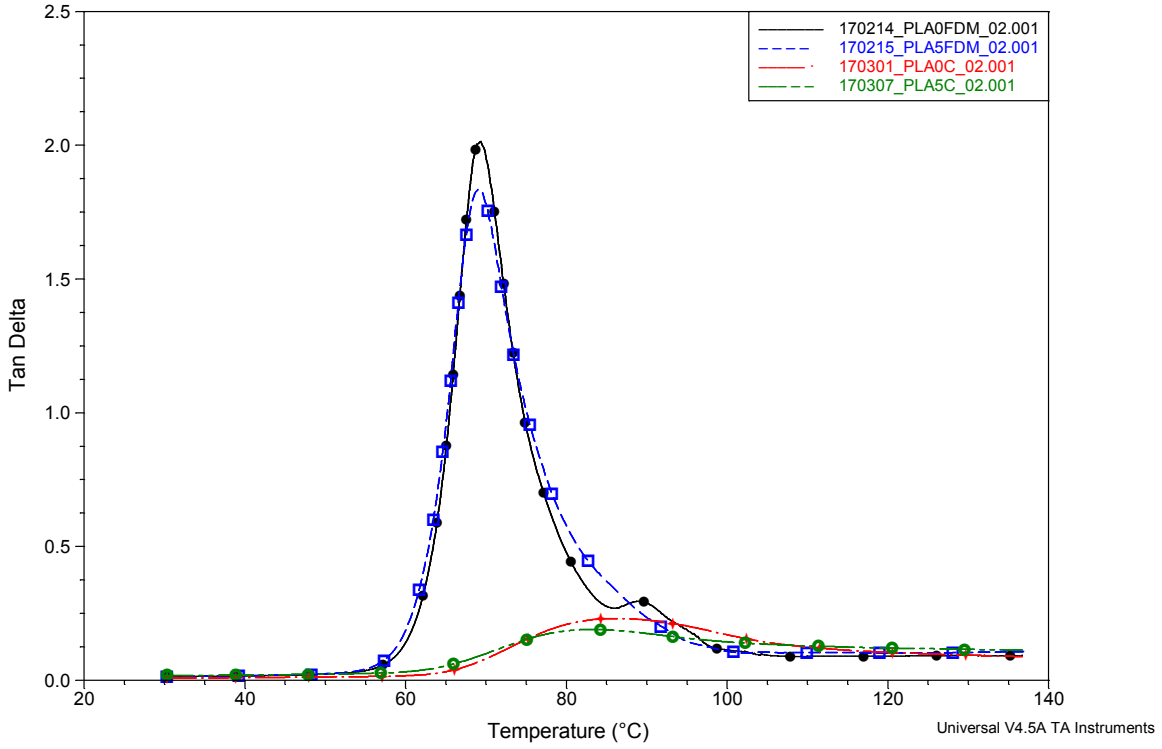

Figure 49 Tan δ in function of the temperature for the pressed and printed samples.

4.6.3 Conclusion

The results of the DMA analysis showed a different behaviour for the FDM printed and compression moulded samples. For the storage modulus of the compression moulded samples, the rubber phase did not display itself as a plateau, while this was the case for the FDM printed samples. Additionally, despite the annealing process, the FDM printed samples had a higher starting storage modulus. This could be the result of the alignment caused by the FDM process. The evolution of the onset of the decrease in storage modulus differed for the FDM printed and pressed samples, while the onset happened at earlier temperatures until the addition of 1% of HA after which the temperature remained

constant for the FDM samples, the temperature decreased until the addition of 3% of HA, followed by an increase and a plateau for the pressed samples. Additionally, the FDM samples displayed a peak in the storage modulus for all composites except PLA/HA 5%. The end of the glass transition was only visible for the FDM samples, the temperature of the end stayed constant till the addition of 3% of HA after which it increased. After the end of the glass transition, it was possible to determine the onset of the cold crystallisation for the FDM samples, the temperature decreased until 1% of HA was added, for which the temperature recovered, and then decreased again with the addition of more HA. The loss modulus peak was over 3 times higher for the FDM printed samples when compared to the compression moulded samples; and happened at a lower temperature. The temperatures at which the peak occurred decreased with the first addition of HA and then remained constant for the FDM printed samples; and decreased for the pressed samples up to the addition of 3% of HA for which the temperature increased again, only to remain constant for the addition of 5% of HA. Finally, the tan δ peak for the compression moulded samples was much lower than that of the FDM printed samples, indicating a restriction of the mobility of the amorphous phase. This could be linked to a higher crystallinity, resulting from the annealing process. A shoulder appeared in the tan δ peak of the FDM printed samples. The origin of this peak was not determined, but it was suggested that it was either the result of the relaxation of the mobility-restricted amorphous regions; or the start of a pre-crystallisation. Further experiments with annealed FDM specimens could determine whether the peak was caused by relaxation, however, the annealing could result in significant changes in the morphology of the FDM specimens. The rubber plateau attained by the FDM samples, is a good indication for the possibility to FDM print at lower temperatures, however, as mentioned before, the lower temperatures do not allow for proper filament interaction and inter filament diffusion.

4.7 Wide angle X-ray diffraction on powder analysis

4.7.1 Introduction

The goal of this study was to determine the interplanar distance and the mean particle size of hydroxyapatite and PLA crystals respectively. The analysis served as a first indication of the actual size of the HA and PLA crystals, after which TEM would be used to determine the particle size of HA. Given that the PLA particles do not show in the TEM analysis, the WAXD-P was also interesting to get an indication of the crystal size. Additionally, it was also possible to identify the HA by using a databank and to identify the purity of the HA.

4.7.2 Results

In this section the results of the WAXD-P analysis are discussed. Figure 50 shows the diffractograms for the extruded PLA and the obtained HA powder. The maximum intensity of the extruded PLA was found at a Bragg angle (2θ) of 16,7025° and the maximum intensity of the HA at 31,8276° (2θ). The positions of these peaks are characteristic for both PLA and HA. Figure 51 shows the results for granules and FDM specimens of the mixtures. The peaks of both PLA and HA show up in the diffractograms of the mixtures, with the PLA peak having maximum intensity. The HA peak of the mixtures is visible in all cases, but has a rather low intensity. Additionally, the HA peak intensity increases with the addition of more HA. This could be an indication for a different crystal size before and after the processing.

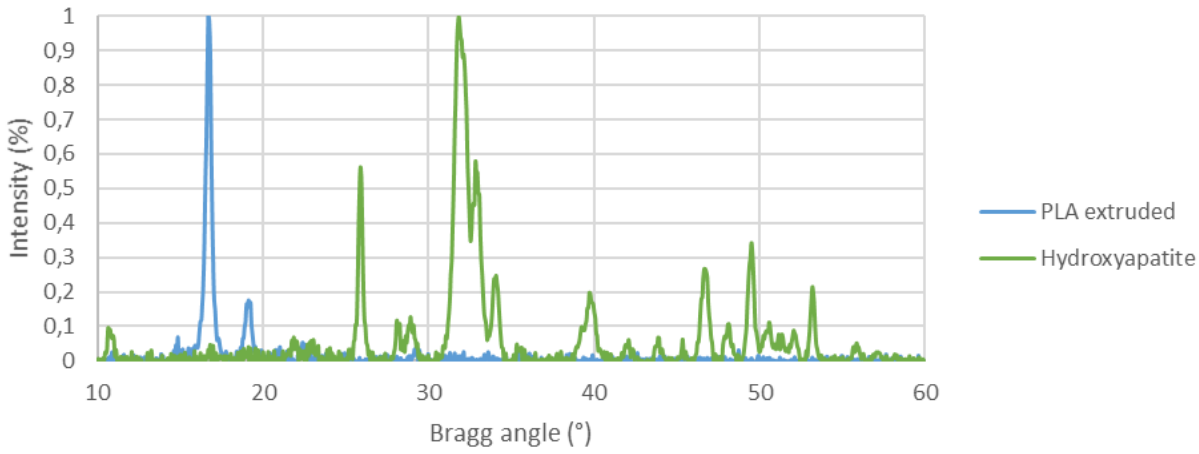

Figure 50 Diffractogram HA powder and extruded PLA powder.

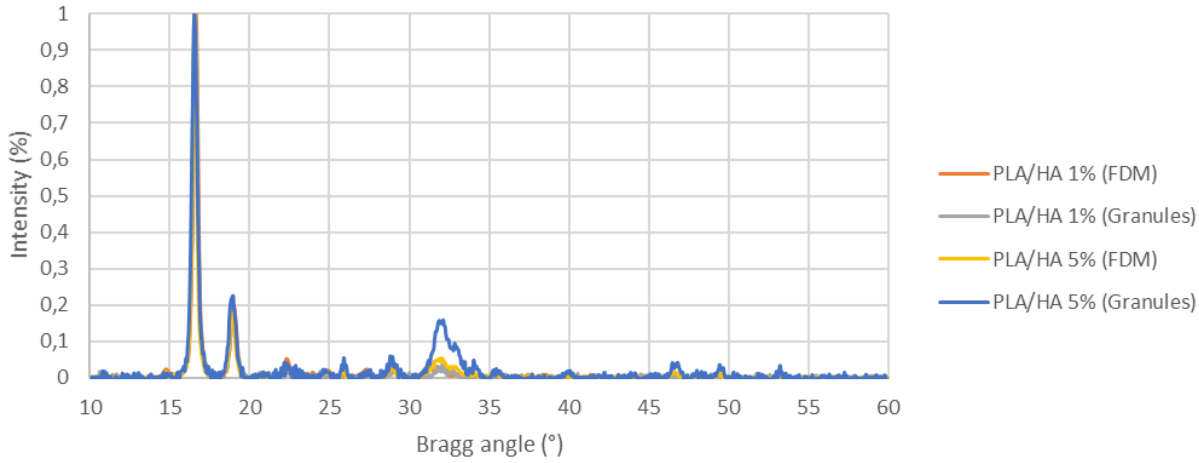

Figure 51 Diffractogram PLA/HA composites.

The Miller indices corresponding to the peaks in the diffractograms were identified with the PLA diffractogram of Zhang et al. and the HA diffractograms of Cengiz et al. and are shown in table 62 and table 63 [74] [203]. The tables also give the corresponding Bragg angle (2θ) and interplanar distance of the PLA and HA crystals. For extruded PLA powder, three peaks were identified, corresponding to (010), (200/110) and (203). The interplanar distance of PLA is larger than that of HA; and for HA, more Miller indices could be attributed to the peaks. The technical sheet of the HA, found on the site of the manufacturer found a similar interplanar distance of 0.34 nm for (002) crystals [225].

Table 62 Bragg angle, Miller index and interplanar distances corresponding to the PLA peaks.

PLA extruded		
2θ (°)	Miller index (hkl)	$d_{(hkl)}$ (nm)
14,8637	(010)	0,600
16,7025	(200/110)	0,532
19,1344	(203)	0,468

Table 63 Bragg angle, Miller index and interplanar distances corresponding to the HA peaks.

HA		
2θ (°)	Miller index (hkl)	$d_{(hkl)}$ (nm)
25,8962	(002)	0,344
31,8276	(211)	0,281
32,8359	(300)	0,273
39,7163	(202)	0,227
46,6561	(222)	0,195
49,5031	(213)	0,184
53,1806	(004)	0,172

Table 64 and table 65 contain the crystal sizes calculated with the Scherrer equation for PLA and HA respectively. It was only possible to calculate the crystal size for single peaks with a high enough intensity, therefore only the crystal size of two peaks for both PLA and HA were calculated. The crystal sizes of HA were not calculated for the composites due to the low intensity of the peaks and the presence of interference, which meant that the results would be inconclusive. It was also presumed that HA was a solid and was not affected as much as a PLA by the different processes, given its nanoform. The $PLA_{(200/210)}$ and $PLA_{(203)}$ crystals increase in size with the addition of HA for the FDM process, while the granules' crystal sizes increase with the addition of 1% of HA, but decrease with the addition of 5% of HA when compared to extruded PLA. There is no significant difference in crystal size, with the average ratio between both crystals being close to 1 for PLA. The crystal shape could not be determined, since it was impossible to attribute directions to the miller indices. The $HA_{(002)}$ and $HA_{(213)}$ crystals have a similar size. The peaks used in this case were not the ones with the highest intensity, this due to the presence of multiple peaks. Again, the miller indices could not be attributed to the peaks. For the HA it is possible to determine the particle shape with TEM analysis.

Table 64 Crystal sizes of PLA for extruded PLA and the composites.

	τ (nm)				
	PLA/HA 0%	PLA/HA 1%		PLA/HA 5%	
Miller index (hkl)		FDM	Granules	FDM	Granules
PLA (200/110)	20,231	22,027	24,857	25,837	19,963
PLA (203)	17,115	17,832	19,508	19,351	16,277
$\tau_{(200/110)}/\tau_{(203)}$	1,2	1,2	1,3	1,335	1,226

Table 65 Crystal sizes of HA.

Miller index (hkl)	τ (nm)
HA (002)	27,159
HA (213)	20,569
$\tau_{(002)}/\tau_{(213)}$	1,320

Figure 52 shows the diffractogram of pure HA and its peaks and their respective intensity. A database was used to match the diffractogram with that of an HA in the database and the HA with the closest diffractogram was found to be reference HA 9 432. The peaks and their intensity of the reference HA, match well with the position and intensity of the peaks found for HA. The good match is also a measure for the purity of the HA.

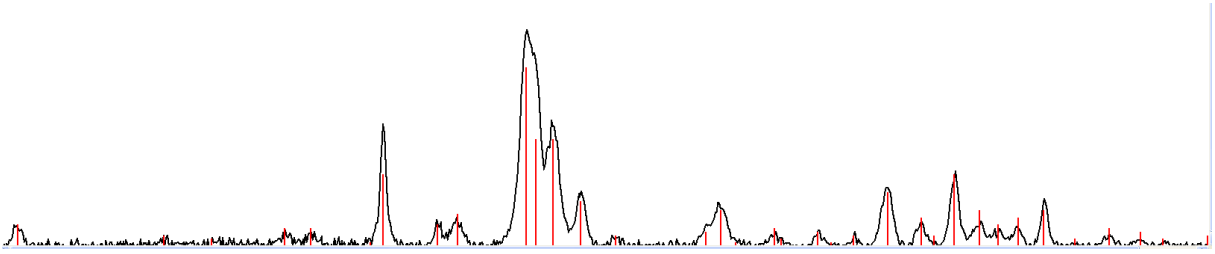

Figure 52 Diffractogram HA and the reference peaks and their intensity of the reference HA 9432.

4.7.3 Conclusion

The $PLA_{(200/210)}$ and $PLA_{(203)}$ crystals increase in size with the addition of HA for the FDM process, while the granules' crystal sizes increase with the addition of 1% of HA, but decrease with the addition of 5% of HA when compared to extruded PLA. Additionally, the ratio of the crystal size of $PLA_{(200/210)}$ and $PLA_{(203)}$ was found to be close to 1. However, it was impossible to determine the shape of the PLA crystals, since the directions corresponding to the two peaks are unknown. Additionally, the directions are not necessarily orthogonal. The nanohydroxyapatite diffractogram was found to correspond with the diffractogram of the reference HA 9-432. Additional TEM testing is necessary to determine the particle shape and size of hydroxyapatite. The TEM testing is also necessary for the determination of the distribution of the nanoparticles, as the WAXD-P only gives information regarding the crystal sizes and interplanar distances. This is important given the possibility that the hydroxyapatite is grouped in nanostructured microparticles and given that this study aims to create PLA/HA composites with a uniform distribution of nano HA particles.

4.8 Transmission electron microscopy

4.8.1 Introduction

The results of the TEM analysis will be discussed in this section. Granule and FDM samples of 1% and 5% HA were tested. The goal of the TEM analysis was the verification of the agglomeration of the nHA particles in the polymer matrix, as well as the determination of the size of the HA nanoparticles. Figure 53 shows the TEM image supplied by the manufacturer and shows an agglomeration of HA particles.

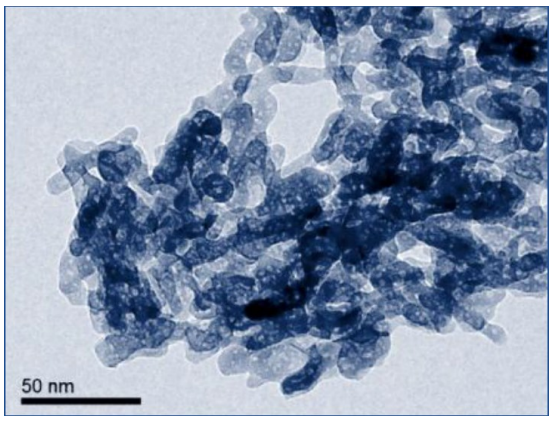

Figure 53 High resolution TEM image of nanoXIM HAp paste [225].

4.8.2 Results

4.8.2.1 Granules

Figure 54, figure 55 and figure 56 show the results for the TEM analysis for PLA/HA 1% granules. From the figures it can be seen that there is a homogenous distribution of HA particles throughout the polymer matrix. The HA particles were found to have a length of 40-50 nm and a diameter of approximately 20 nm.

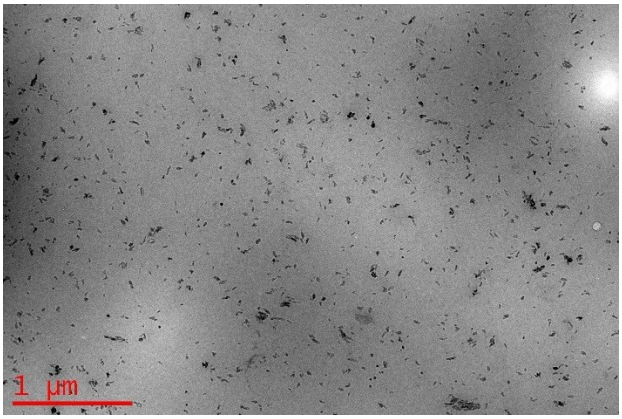

Figure 54 TEM image PLA/HA 1% granules (scale 1 µm).

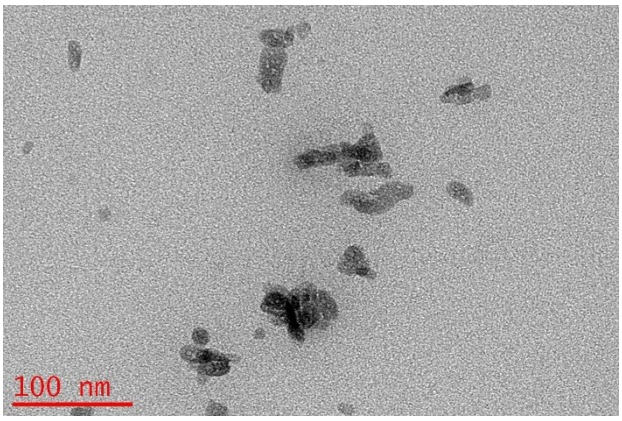

Figure 55 TEM image PLA/HA 1% granules (scale 100 nm).

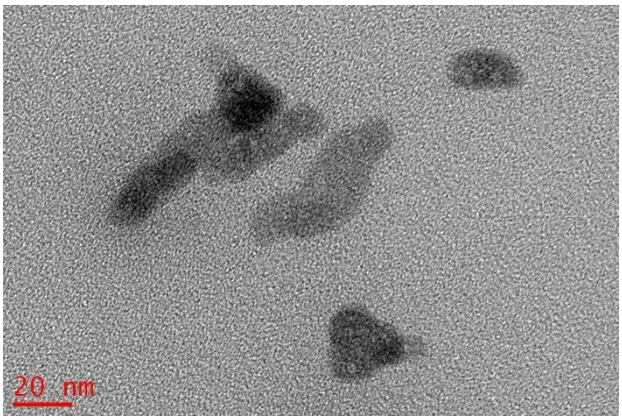

Figure 56 TEM image PLA/HA 1% granules (scale 20 nm).

Figure 57, figure 58 and figure 59 show the results of the TEM analysis of the PLA/HA 5% granules. Compared to the 1% granules, there is more agglomeration of HA particles. However, despite the agglomerations, the HA particles are still homogenously distributed throughout the polymer matrix.

For the PLA/HA 5% granules, the HA particles were found to again have a length of 40-50 nm and a diameter of approximately 20 nm.

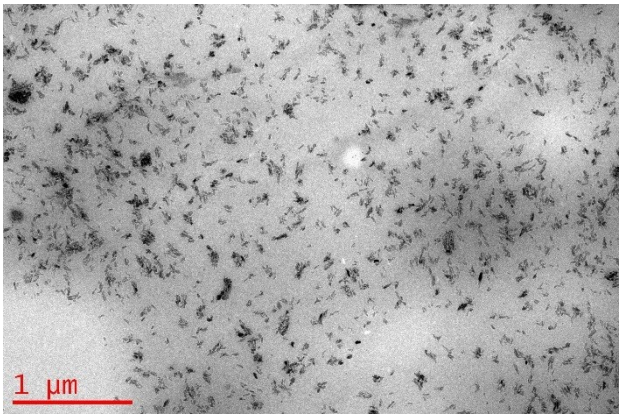

Figure 57 TEM image PLA/HA 5% granules (scale 1 µm).

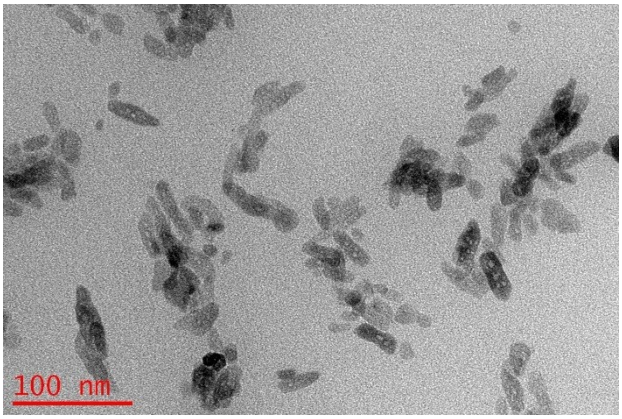

Figure 58 TEM image PLA/HA 5% granules (100 nm).

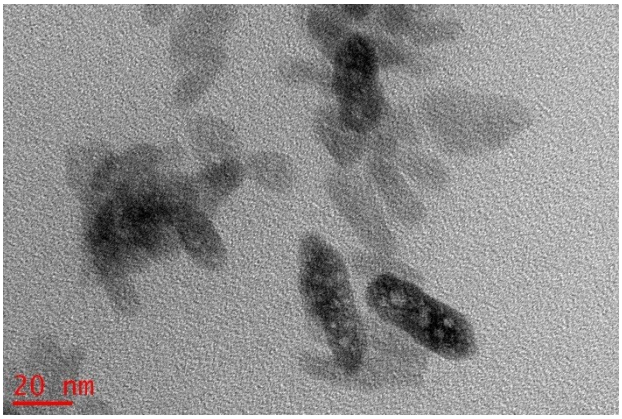

Figure 59 TEM image PLA/HA 5% granules (scale 20 nm).

4.8.2.2 FDM specimens

Figure 60, figure 61 and figure 62 show the results of the TEM analysis of PLA/HA 1% FDM samples. Again, the nanoparticles are homogenously distributed throughout the polymer matrix. The HA particles were found to have a length of 40-50 nm and a diameter of approximately 20 nm. Therefore, the size of the nanoparticles seems to have been unaffected by the different processes, as a similar

size was found for the granules, which did not undergo a single-screw extrusion and FDM printing process.

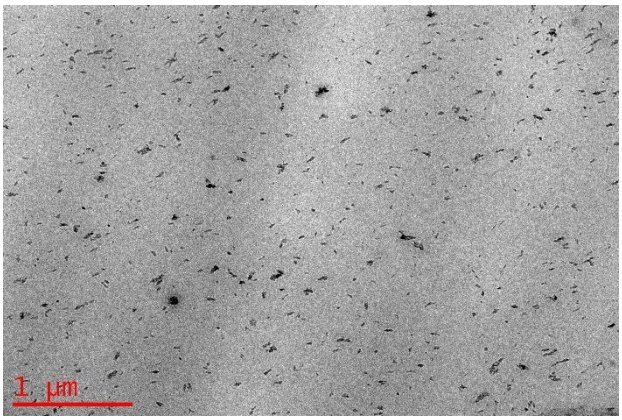

Figure 60 TEM image PLA/HA 1% FDM specimen (scale 1 µm).

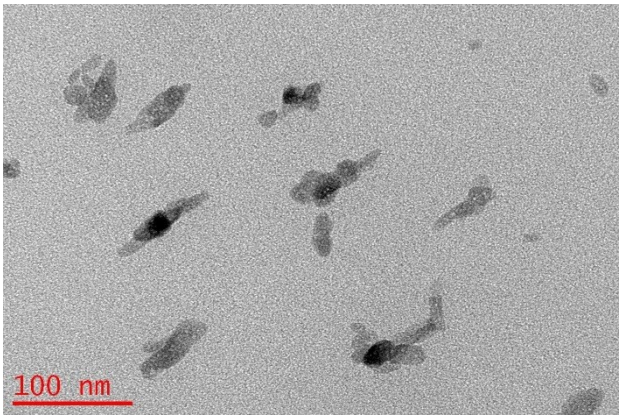

Figure 61 TEM image PLA/HA 1% FDM specimen (scale 100 nm).

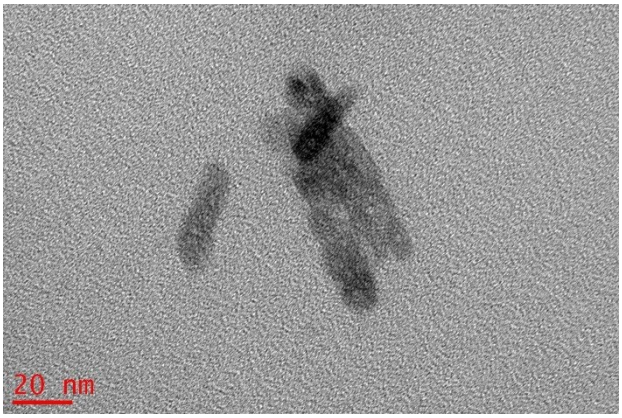

Figure 62 TEM image PLA/HA 1% FDM specimen (scale 20 nm).

Figure 63, figure 64 and figure 65 show the results of the TEM analysis of PLA/HA 5% FDM specimens. Compared to the 5% granules, the FDM specimens seem to have more agglomeration, making the dispersion less homogenous. Additionally, due to the agglomeration, the particle size was not found. However, the particle size is expected to have stayed the same, given that the 1% FDM specimens showed a similar particle size.

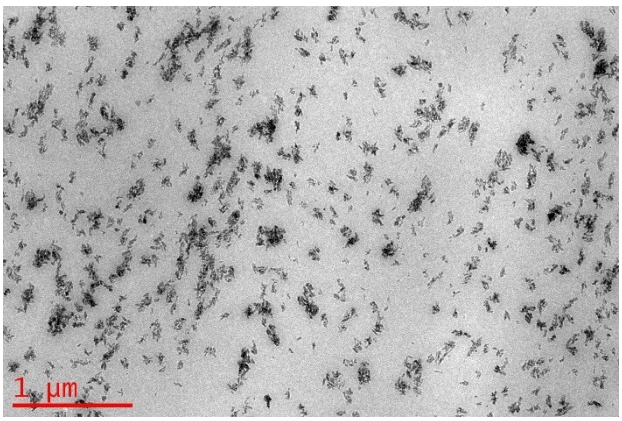

Figure 63 TEM image PLA/HA 5% FDM specimen (scale 1µm).

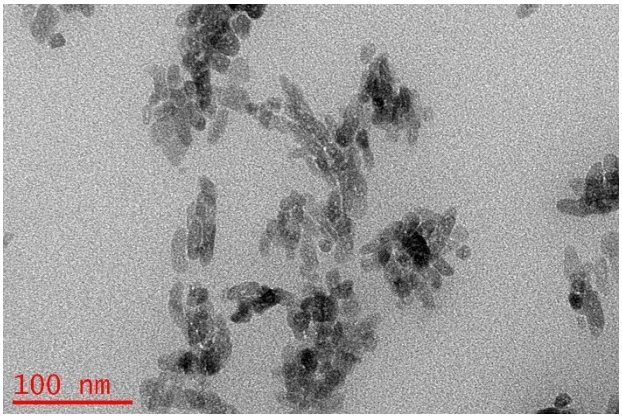

Figure 64 TEM image PLA/HA 5% FDM specimen (scale 100 nm).

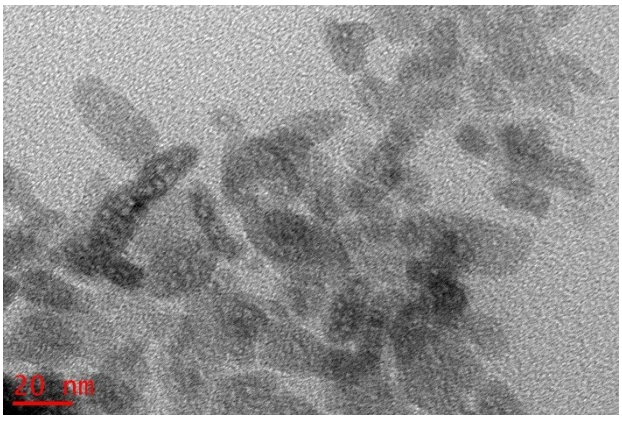

Figure 65 TEM image PLA/HA 5% FDM specimen (scale 20 nm).

4.8.3 Conclusion

Compared to the TEM image supplied by the manufacturer, the distribution of the HA in the PLA matrix is very good for both the granules and the FDM specimens. Additionally, the different processes do not seem to affect the agglomeration as much as the addition of more HA. The agglomeration of HA nanoparticles only increased slightly when comparing the FDM process to the extruded granules, while the increase of the HA concentration resulted in a higher agglomeration, which was expected. The agglomeration results in a lower specific surface and thus the mechanical properties will be less impacted by the filler. However, the distribution is still good, so globally, the mechanical properties will still be similar in a specimen. The size of the nanoparticles of approximately 40-50 nm in the length

and 20 nm for the diameter indicates that each particle is composed of one to two crystals, when considering that the Scherrer calculation resulted in a crystal size of 27.159 nm for the (002) crystals and 20.569 nm for the (213) crystals. It can thus be supposed that the particles are mono- or bi-crystalline.

4.9 Permeability tests

4.9.1 Introduction

In this section, the results of the permeability tests will be discussed. Compression moulded films of the formulations were tested for WVTR and OTR. The results of the permeability tests were used to verify the influence of the HA content on the WVTR and OTR.

4.9.2 Results

Table 66 shows the results of the WVTR tests. The table shows that the first addition of HA increases the WVTR, adding 3% of HA results in a recovery to the WVTR of PLE 005, adding 5% of HA results in another increase and adding 10% of HA results in a decrease in WVTR up to values under that of the PLE 005. The initial increase in WVTR, could be due to the degradation caused by extrusion. The recovery of the WVTR with the addition of 3% and more HA, could be linked to the crystallinity. Tsuji et al. found that the WVTR of PLA decreased monotonically with the addition of HA [163].

Table 66 WVTR values found for the PLA/HA composites and PLE 005.

	WVTR (g*mm/[m²*day*bar])
PLE 005	124
PLA/HA 0,5%	136
PLA/HA 3%	124
PLA/HA 5%	128
PLA/HA 10%	118

Table 67 shows the results of the OTR tests. The OTR of PLA decreases with the addition of HA. Additionally, the OTR decreased over time, which was especially notable for the PLE 005. The difference between PLE 005 and the HA composites can be explained by the higher molar weight of the PLE 005.

Table 67 OTR values PLA/HA composites and PLE 005.

	Thickness (µm)		Test area (cm²)		OTR
	Sample 1	Sample 2	Sample 1	Sample 2	cc/[m²-day]
PLE 005	93,8 ± 1,4	94,2 ± 1,9	15,14	14,68	178,2 ± 3,0
PLA/HA 5%	92,3 ± 2,1	90,3 ± 3,1	14,07	14,44	161,5 ± 4,6
PLA/HA 10%	93,6 ± 1,5	93,3 ± 1,5	14,77	14,44	152,0 ± 0,1

4.9.3 Conclusion

The addition of nHA to PLA does not seem to affect the WVTR and the OTR greatly. For PLA, an interesting behaviour was observed during the testing, the OTR decreased over time for repeated measurements on the same sample, especially for the neat PLA. Under 38°C and 50% RH, the neat PLA also displayed an interesting behaviour for the WVTR, given that the WVTR was found to be lower

compared to WVTR tests at 23°C and 50% RH. Given the low impact of the nHA on the OTR and the WVTR, nHA cannot be used to control the permeability of PLA, this would have been interesting for BTE and packaging applications.

5 Conclusion

The first goal of this study was to formulate PLA/nHA (0 wt.%; 0.5 wt.%; 1 wt.%; 3 wt.% and 5 wt.%) nanocomposites from polylactide acid and an aqueous hydroxyapatite paste. This was done successfully, by melt mixing PLA and nHA in a twin-screw extruder. To achieve the second goal, the application of the nanocomposites in fused deposition modelling and injection moulding, the composites were turned into filaments with a single-screw extruder. After which the filaments were used in fused deposition modelling, with 7 different printing conditions, as described by the doehler matrix.

The characterisation of the obtained materials was the third goal of this study. The hydroxyapatite content before and after each process was verified with a thermogravimetric analysis and the results indicated that after each process, the hydroxyapatite content was slightly reduced. Processes also affected the degradation profile of the different formulations, with the degradation starting the earliest for the filaments. Differential scanning calorimetry was used to determine the minimum printing temperature for the fused deposition modelling process. However, the minimum temperature of 183.4°C did not correspond to the actual minimum printing temperature, as printing temperatures were required to exceed 190°C for certain formulations. This was attributed to the difference in heating ramp between the analysis and the printing process. Oscillatory rheology results showed that the extrusion and the addition of hydroxyapatite both influence the viscosity. The extrusion resulted in a reduction of the viscosity, due to the reduction of the molar mass, while the first addition of HA increases the viscosity of the extruded PLA, after which the viscosity decreases gradually with the addition of more HA. Additionally, there was also a thinning effect after 3% of HA was added. The evolution of the viscosity was linked to the fused deposition printing process and it was suggested that the viscosity decreases for higher printing speeds. Consequently, there is no risk of nozzle clogging when using PLA with a high HA content during the FDM printing process, which was suggested by the literature. Finally, dynamic mechanical analysis indicated that the storage modulus of fused deposition modelling printed samples was higher, when compared to compression moulded samples. It was suggested that the higher storage modulus was the result of alignment caused by the fused deposition modelling process.

The fourth goal of this study was the comparison of the impact of the fused deposition modelling process and injection moulding on the tensile properties of the composites. Doehlert response surface methodology was used to determine the impact of the fused deposition modelling process on the tensile properties. However, the used model was found to be inadequate to describe the evolution of the tensile properties of all formulations. The tensile test results of the injection moulded samples showed that the tensile properties of these samples were much higher when compared to samples obtained by fused deposition modelling process. Although the printing parameters used during the fused deposition modelling process did influence the tensile properties, the lower tensile properties were mainly attributed to the process given that it introduced a lot of faults into the tensile specimens.

Determining the dispersion state of the nano-charges in the polymer matrix was the fifth goal of this study. A combination of x-ray diffraction analysis and transmission electron microscopy was used to determine the dispersion of the nano-charges. The x-ray diffraction analysis also allowed for the

identification of the used hydroxyapatite, which was found to be HA 9-432 (reference). The crystal size of HA was found to be 27.159 nm for (002) HA crystals and 20.569 nm for (213) HA crystals. TEM analysis showed that the HA particles were 40-50 nm long and had a diameter of approximately 20 nm, from which it was concluded that the particles were mono- or bicrystalline. Additionally, for both the granules and the FDM process, the dispersion was found to have improved when compared to the TEM image supplied by the manufacturer.

The final objectives of this study were the creation of composite films and the testing of the permeability of these films. A heated press was successfully used to create composite films with an average thickness of 90 µm. However, the results of the WVTR and the OTR tests showed that the HA did not have a major impact on these properties.

In perspective, the results of this study can be used as starting points for future research. Doehlert response surface methodology indicated that the used model for the characterisation of the tensile properties of fused deposition modelling specimens was inadequate. Therefore, future studies can focus on the determination of the exact model. Additionally, more tests are needed with regards to the influence of the parameters used in the fused deposition modelling process on the process. Especially the control of the porosity, measured by tomography, could be an interesting study, given that this would be of interest for bone tissue engineering applications. The tensile tests were used to study the bonding quality of the FDM printed samples, but for BTE compression tests are more used, since this is the type of strain will be applied to the implants. The use of hydroxyapatite microcharges in the fused deposition modelling process could also be tested, this would greatly reduce the cost. Additionally, the micro charges could impact the material differently, however, nozzle clogging is a very real threat, since micro charges are much larger and can more easily obstruct the nozzle. Dynamic mechanical analysis resulted in a higher storage modulus for the fused deposition modelling printed samples, which was surprising and thus requires more testing to validate and understand this phenomenon. Finally, the results of the oscillatory rheology indicate a complex behaviour with the addition of hydroxyapatite. More tests are needed, at different temperatures and using capillary rheology. A time temperature superposition is needed to model the rheological behaviour; this was difficult to obtain with the oscillatory rheometer due to the flowing of the polymer material. The capillary rheometer is needed to model the behaviour at higher shear rates and temperatures.

References

[1] Université de Reims Champagne-Ardenne, “Laboratory of Engineering and Materials Sciences (LISM - EA 4695),” [Online]. Available: http://www.univ-reims.eu/about-the-university/organisation/organisation,77,18761.html?&args=bl3P8HNScfah65Uek-amZ3pu4GPo7H2TaI_qTyAn0FRSQJsWGb61Uw1V_7X1Ji_3cmFA1GMa4KqDRaUhgRZ_qA. [Accessed 1 March 2017].

[2] G. Ginoux, “PolyFabAdd - Polymères chargés en fabrication additive,” [Online]. Available: http://www.theses.fr/s143395. [Accessed 1 March 2017].

[3] I. Armentano, N. Bitinis, E. Fortunati, S. Mattioli, N. Rescignano, R. Verdejo, M. A. Lopez-Manchado and J. M. Kenny, “Multifunctional nanostructured PLA materials for packaging and tissue engineering,” *Progress in Polymer Science,* vol. 38, no. 10-11, pp. 1720-1747, 2013.

[4] B. N. Turner and S. A. Gold, “A review of melt extrusion additive manufacturing processes: II. Materials, dimensional accuracy, and surface roughness,” *Rapid Prototyping Journal; Bradford,* vol. 21, no. 3, pp. 261-250, 2015.

[5] B. N. Turner, R. Strong and S. A. Gold, “A review of melt extrusion additive manufacturing processes: I. Process design and modeling,” *Rapid Prototyping Journal; Bradford,* vol. 20, no. 3, pp. 192-204, 2014.

[6] A. K. Sood, R. K. Ohdar and S. S. Mahapatra, “Parametric appraisal of mechanical property of fused deposition modelling processed parts,” *Materials & Design,* vol. 31, no. 1, pp. 287-295, 2010.

[7] O. S. Carneiro, A. F. Silva and R. Gomes, “Fused deposition modeling with polypropylene,” *Materials & Design,* vol. 83, pp. 768-776, 2015.

[8] Anonymous, “3D Printing Materials | Stratasys,” [Online]. Available: http://www.stratasys.com/materials. [Accessed 22 March 2017].

[9] Anonymous, “FDM materials: PLA and ABS,” [Online]. Available: https://3faktur.com/en/3d-printing-materials-technologies/fdm-materials-pla-and-abs/. [Accessed 22 March 2017].

[10] Anonymous, “Materialise,” [Online]. Available: http://www.materialise.com/en/manufacturing/technologies-materials/fused-deposition-modeling. [Accessed 3 March 2017].

[11] Anonymous, “Page 2 | 3d Printer Filaments Shop | Nexeo 3D,” [Online]. Available: https://www.nexeo3d.com/en/products.html?%3Fgclid=CL2GruTd6NICFcSfGwod8JgItQ&p=2. [Accessed 3 March 2017].

[12] F. Rayegani and G. C. Onwubolu, “Fused deposition modelling (FDM) process parameter prediction and optimization using group method for data handling (GMDH) and differential evolution (DE),” *The International Journal of Advanced Manufacturing Technology,* vol. 73, no. 1-4, pp. 509-519, 2014.

[13] A. Mahboubi Soufiani, M. Salehi, M. Skrifvars, M. Persson and S.-W. Cho, "Thermomechanical properties of poly(lactic acid) films reinforced with hydroxyapatite and regenerated cellulose microfibers," *Journal of Applied Polymer Science,* vol. 131, no. 20, p. n/a, 2014.

[14] O. A. Mohamed, S. H. Masood, J. L. Bhowmik, M. Nikzad and J. Azadmanjiri, "Effect of Process Parameters on Dynamic Mechanical Performance of FDM PC/ABS Printed Parts Through Design of Experiment," *Journal of Materials Engineering and Performance,* vol. 25, no. 7, pp. 2922-2935, 2016.

[15] J. Torres, J. Cotelo, J. Karl and A. P. Gordon, "Mechanical Property Optimization of FDM PLA in Shear with Multiple Objectives," *The Journal of The Minerals, Metals & Materials Society (TMS),* vol. 67, no. 5, pp. 1183-1193, 2015.

[16] O. Ivanova, C. Williams and T. Campbell, "Additive manufacturing (AM) and nanotechnology: promises and challenges," *Rapid Prototyping Journal; Bradford,* vol. 19, no. 5, pp. 353-364, 2013.

[17] Q. Yao, B. Wei, Y. Guo, C. Jin, X. Du, C. Yan, J. Yan, W. Hu, Y. Xu, Z. Zhou, Y. Wang and L. Wang, "Design, construction and mechanical testing of digital 3D anatomical data-based PCL-HA bone tissue engineering scaffold," *Journal of Materials Science : Materials in Medicine,* vol. 26, no. 1, pp. 1-9, 2015.

[18] G. Wei and P. X. Ma, "Structure and properties of nano-hydroxyapatite/polymer composite scaffolds for bone tissue engineering," *Biomaterials,* vol. 25, no. 19, pp. 4749-4757, 2004.

[19] E. Nejati, H. Mirzadeh and M. Zandi, "Synthesis and characterization of nano-hydroxyapatite rods/poly(l-lactide acid) composite scaffolds for bone tissue engineering," *Composites Part A: Applied Science and Manufacturing,* vol. 30, no. 10, pp. 1589-1596, 2008.

[20] H.-T. Liao, C. Yo-Yu, L. Yu-Ting, M.-F. Hsieh and J. Cho-Pei, "The Osteogenesis of Bone Marrow Stem Cells on mPEG-PCL-mPEG/Hydroxyapatite Composite Scaffold via Solid Freeform Fabrication," *BioMed Research International,* vol. 2014, p. 13, 2014.

[21] A. B. Kutkov and J. Song, "An amphiphilic degradable polymer/hydroxyapatite composite with enhanced handling characteristics promotes osteogenic gene expression in bone marrow stromal cells," *Acta Biomaterialia,* vol. 9, no. 9, pp. 8354-8364, 2013.

[22] L. Han, C. Han, H. Zhang, S. Chen and L. Dong, "Morphology and properties of biodegradable and biosourced polylactide blends with poly(3-hydroxybutyrate-co-4-hydroxybutyrate)," *Polymer Composites,* vol. 33, no. 6, pp. 850-859, 2012.

[23] Y. Guo, K. Yang, X. Zuo, Y. Xue, C. Marmorat, Y. Liu, C.-C. Chang and M. H. Rafailovich, "Effects of clay platelets and natural nanotubes on mechanical properties and gas permeability of Poly (lactic acid) nanocomposites," *Polymer,* vol. 83, pp. 246-259, 2016.

[24] E. Picard, E. Espuche and R. Fulchiron, "Effect of an organo-modified montmorillonite on PLA crystallization and gas barrier properties," *Applied Clay Science,* vol. 53, no. 1, pp. 58-65, 2011.

[25] T. Iwata, “Biodegradable and Bio-Based Polymers: Future Prospects of Eco-Friendly Plastics,” *Angewandte Chemie INternational Edition,* vol. 54, no. 11, pp. 3210-3215, 2015.

[26] K. Van de Velde and P. Kiekens, “Biopolymers: overview of several properties and consequences on their applications,” *Polymer Testing,* vol. 21, no. 4, pp. 433-442, 2002.

[27] M. Patel, F. Marscheider-Weidemann, J. Schleich, B. Hüsing and G. Angerer, “Techno-economic feasibility of large-scale production of bio-based polymers in Europe,” Technical Report EUR 22103 EN, 2005.

[28] D. K. Platt, Biodegradable Polymers: Market report, Shrewsbury, UK: Smithers Rapra Limited, 2006.

[29] M. Jamshidian, E. A. Tehrany, M. Imran, M. Jacquot and S. Desobry, “Poly-Lactic Acid: Production, Applications, Nanocomposites, and Release Studies,” *Comprehensive Reviews in Food Science and Food Safety,* vol. 9, no. 5, pp. 552-571, 2010.

[30] M. Murariu and P. Dubois, “PLA composites: From production to properties,” *Advanced Drug Delivery Reviews,* vol. 107, no. 15, pp. 17-46, 2016.

[31] K. Madhavan Nampoothiri, N. R. Nair and R. P. John, “An overview of the recent developments in polylactide (PLA) research,” *Bioresource Technology,* vol. 101, no. 22, pp. 8493-8501, 2010.

[32] L.-T. Lim, R. Auras and M. Rubino, “Processing technologies for poly(lactic acid),” *Progress in Polymer Science,* vol. 33, no. 8, pp. 820-852, 2008.

[33] R. Auras, B. Harte and S. Selke, “An Overview of Polylactides as Packaging Materials,” *Macromolecular Bioscience,* vol. 4, no. 9, pp. 835-864, 2004.

[34] E. T. Vink, K. R. Rábago, D. A. Glassner and P. R. Gruber, “Applications of life cycle assessment to NatureWorks™ polylactide (PLA) production,” *Polymer Degradation and Stability,* vol. 80, no. 3, pp. 403-419, 2003.

[35] A. J. R. Lasprilla, G. A. R. Martinez, B. H. Lunelli, A. L. Jardini and R. M. Filho, “Poly-lactic acid synthesis for application in biomedical devices — A review,” *Biotechnology Advances,* vol. 30, no. 1, pp. 321-328, 2012.

[36] S. Farah, D. G. Anderson and R. Langer, “Physical and mechanical properties of PLA, and their functions in widespread applications — A comprehensive review,” *Advanced Drug Delivery Reviews,* 2016.

[37] A. Södergård and M. Stolt, “Properties of lactic acid based polymers and their correlation with composition,” *Progress in Polymer Science,* vol. 27, no. 6, pp. 1123-1163, 2002.

[38] M. L. Di Lorenzo, “Crystallization behavior of poly(l-lactic acid),” *European Polymer Journal,* vol. 41, no. 3, pp. 569-575, 2005.

[39] J. Puiggali, Y. Ikada, H. Tsuji, L. Cartier, T. Okihara and B. Lotz, “The frustrated structure of poly(l-lactide),” *Polymer,* vol. 41, no. 25, pp. 8921-8930, 2000.

[40] L. Cartier, T. Okihara, Y. Ikada, H. Tsuji, J. Puiggali and B. Lotz, “Epitaxial crystallization and crystalline polymorphism of polylactides,” *Polymer,* vol. 41, no. 25, pp. 8909-8919, 2000.

[41] B. Gupta, N. Revagade and J. Hilborn, “Poly(lactic acid) fiber: An overview,” *Progress in Polymer Science,* vol. 32, no. 4, pp. 455-482, 2007.

[42] J. Lunt, “Large-scale production, properties and commercial applications of polylactic acid polymers,” *Polymer Degradation and Stability,* vol. 59, no. 1-3, pp. 145-152, 1998.

[43] J. A. Cicero, J. R. Dorgan, J. Garrett, J. Runt and J. S. Lin, “Effects of molecular architecture on two-step, melt-spun poly(lactic acid) fibers,” *Journal of Applied Polymer Science,* vol. 86, no. 11, pp. 2839-2846, 2002.

[44] J. A. Cicero, J. R. Dorgan, J. Garrett, J. Runt and J. S. Lin, “Supramolecular morphology of two-step, melt-spun poly(lactic acid) fibers,” *Journal of Applied Polymer Science,* vol. 86, no. 11, pp. 2828-2838, 2002.

[45] K. S. Anderson and M. A. Hillmyer, “Melt preparation and nucleation efficiency of polylactide stereocomplex crystallites,” *Polymer,* vol. 47, no. 6, pp. 2030-2035, 2006.

[46] H. Urayama, S.-I. Moon and Y. Kimura, “Microstructure and Thermal Properties of Polylactides with Different L- and D-Unit Sequences: Importance of the Helical Nature of the L-Sequenced Segments,” *Macromolecular Materials and Engineering,* vol. 288, no. 2, pp. 137-143, 2003.

[47] H. Urayama, T. Kanamori and Y. Kimura, “Properties and Biodegradability of Polymer Blends of Poly(L-lactide)s with Different Optical Purity of the Lactate Units,” *Macromolecular Materials and Engineering,* vol. 287, no. 2, pp. 116-121, 2002.

[48] F. Carrasco, P. Pagès, J. Gámez-Pérez, O. Santana and M. Maspoch, “Processing of poly(lactic acid): Characterization of chemical structure, thermal stability and mechanical properties,” *Polymer Degradation and Stability,* vol. 95, no. 2, pp. 116-125, 2010.

[49] L. Petersson, I. Kvien and K. Oksman, “Structure and thermal properties of poly(lactic acid)/cellulose whiskers nanocomposite materials,” *Composites Science and Technology,* vol. 67, no. 11-12, pp. 2535-2544, 2007.

[50] P. Mróz, S. Białas, M. Mucha and H. Kaczmarek, “Thermogravimetric and DSC testing of poly(lactic acid) nanocomposites,” *Thermochimica Acta,* vol. 573, pp. 186-192, 2013.

[51] G. Ozkoc and S. Kemaloglu, “Morphology, biodegradability, mechanical, and thermal properties of nanocomposite films based on PLA and plasticized PLA,” *Journal of Applied Polymer Science,* vol. 114, no. 4, pp. 2481-2487, 2009.

[52] Z. Kulinski and E. Piorkowska, “Crystallization, structure and properties of plasticized poly(l-lactide),” *Polymer,* vol. 46, no. 23, pp. 10290-10300, 2005.

[53] Z. Liu, Y. Chen and W. Ding, “Preparation, dynamic rheological behavior, crystallization, and mechanical properties of inorganic whiskers reinforced polylactic acid/hydroxyapatite nanocomposites,” *Journal of Applied Polymer Science,* vol. 133, no. 18, 2016.

[54] D. Garlotta, “A Literature Review of Poly(Lactic Acid),” *Journal of Polymers and the Environment,* vol. 9, no. 2, pp. 63-84, 2001.

[55] C. Migliaresi, D. Cohn, A. De Lollis and L. Fambri, “Dynamic mechanical and calorimetric analysis of compression-molded PLLA of different molecular weights: Effect of thermal treatments,” *Journal of Applied Polymer Science,* vol. 43, no. 1, pp. 83-95, 1991.

[56] F. Signori, M.-B. Coltelli and S. Bronco, “Thermal degradation of poly(lactic acid) (PLA) and poly(butylene adipate-co-terephthalate) (PBAT) and their blends upon melt processing,” *Polymer Degradation and Stability,* vol. 94, no. 1, pp. 74-82, 2009.

[57] V. Taubner and R. Shishoo, “Influence of processing parameters on the degradation of poly(L-lactide) during extrusion,” *Journal of Applied Polymer Science,* vol. 79, no. 12, pp. 2128-2135, 2001.

[58] S.-H. Hyon, K. Jamshidi and Y. Ikada, “Effects of residual monomer on the degradation of DL-lactide polymer,” *Polymer International,* vol. 46, no. 3, pp. 196-202, 1998.

[59] H. Yu, N. Huang, C. Wang and Z. Tang, “Modeling of poly(L-lactide) thermal degradation: Theoretical prediction of molecular weight and polydispersity index,” *Journal of Applied Polymer Science,* vol. 88, no. 11, pp. 2557-2562, 2003.

[60] M. Vert, D. Yoshiharu, K.-H. Hellwich, M. Hess, P. Hodge, K. Przemyslaw, M. Rinaudo and F. Schué, “Terminology for biorelated polymers and applications (IUPAC Recommendations 2012),” *Pure and Applied Chemistry,* vol. 84, no. 2, pp. 377-410, 2012.

[61] S. Grima, V. Bellon-Maurel, P. Feuilloley and F. Silvestre, “Aerobic Biodegradation of Polymers in Solid-State Conditions: A Review of Environmental and Physicochemical Parameter Settings in Laboratory Simulations,” *Journal of Polymers and the Environment,* vol. 8, no. 4, pp. 183-195, 2000.

[62] L. Avérous and E. Pollet, Environmental Silicate Nano-Biocomposites, London: Springer London, 2012.

[63] R. Chandra and R. Rustgi, “Biodegradable Polymers,” *Progress in Polymer Science,* vol. 23, no. 7, pp. 1273-1335, 1998.

[64] G. E. Luckachan and C. K. S. Pillai, “Biodegradable Polymers- A Review on Recent Trends and Emerging Perspectives,” *Journal of Polymers and the Environment,* vol. 19, no. 3, pp. 637-676, 2011.

[65] T. Suyama, Y. Tokiwa, P. Ouichanpagdee, T. Kanagawa and Y. Kamagata, “Phylogenetic Affiliation of Soil Bacteria That Degrade Aliphatic Polyesters Available Commercially as Biodegradable Plastics,” *Applied and Environmental Microbiology,* vol. 64, no. 12, pp. 5008-5011, 1998.

[66] G. Kale, R. Auras, S. P. Singh and R. Narayan, “Biodegradability of polylactide bottles in real and simulated composting conditions,” *Polymer Testing,* vol. 26, no. 8, pp. 1049-1061, 2007.

[67] Y. Oda, A. Yonetsu, T. Urakami and K. Tonomura, “Degradation of polylactide by commercial proteases,” *Journal of Polymers and the Environment,* vol. 8, no. 1, pp. 29-32, 2000.

[68] H.-A. Lim, T. Raku and Y. Tokiwa, “Hydrolysis of polyesters by serine proteases,” *Biotechnology Letters,* vol. 27, no. 7, pp. 459-464, 2005.

[69] Y. Tokiwa and B. P. Calabia, “Biodegradability and biodegradation of poly(lactide),” *Applied Microbiology and Biotechnology,* vol. 72, no. 2, pp. 244-251, 2006.

[70] H. Tsuji, H. Daimon and K. Fujie, “A New Strategy for Recycling and Preparation of Poly(L-lacticacid): Hydrolysis in the Melt,” *Biomacromolecules,* vol. 4, no. 3, pp. 835-840, 2003.

[71] V. Piemonte and F. Gironi, “Kinetics of Hydrolytic Degradation of PLA,” *Journal of Polymers and the Environment,* vol. 21, no. 2, pp. 313-318, 2013.

[72] A. Carné Sánchez and S. R. Collinson, “The selective recycling of mixed plastic waste of polylactic acid and polyethylene terephthalate by control of process conditions,” *European Polymer Journal,* vol. 47, no. 10, pp. 1970-1976, 2011.

[73] J. W. Rink, “Apatite,” in *Encyclopedia of Scientific Dating Methods*, Dordrecht, Springer Netherlands, 2015, pp. 53-54.

[74] B. Cengiz, Y. Gokce, N. Yildiz, Z. Aktas and A. Calimli, “Synthesis and characterization of hydroxyapatite nanoparticles,” *Colloids and Surfaces A: Physicochemical and Engineering Aspects,* vol. 322, no. 1-3, pp. 29-33, 2008.

[75] F. Wang, M.-S. Li, Y.-P. Lu, Y.-X. Qi and Y.-X. Liu, “Synthesis and microstructure of hydroxyapatite nanofibers synthesized at 37°C,” *Materials Chemistry and Physics,* vol. 95, no. 1, pp. 145-149, 2006.

[76] C.-C. Chen, J.-Y. Chueh, H. Tseng, H.-M. Huang and S.-Y. Lee, “Preparation and characterization of biodegradable PLA polymeric blends,” *Biomaterials,* vol. 24, no. 7, pp. 1167-1173, 2003.

[77] X. Su, K. Sun, F. Z. Cui and W. J. Landis, “Organization of apatite crystals in human woven bone,” *Bone,* vol. 32, no. 2, pp. 150-162, 2003.

[78] M. Maas, U. Hess and K. Rezwan, “The contribution of rheology for designing hydroxyapatite biomaterials,” *Current Opinion in Colloid & Interface Science,* vol. 19, no. 6, pp. 585-593, 2014.

[79] M.-O. Montjovent, L. Mathieu, H. Schmoekel, S. Mark, P.-E. Bourban, P.-Y. Zambelli, L. A. Laurent-Applegate and D. P. Pioletti, “Repair of critical size defects in the rat cranium using ceramic-reinforced PLA scaffolds obtained by supercritical gas foaming,” *Journal of Biomedical Materials Research Part A,* vol. 83A, no. 1, pp. 41-51, 2007.

[80] S. Ramakrishna, J. Mayer, E. Wintermantel and K. W. Leong, “Biomedical applications of polymer-composite materials: a review,” *Composites Science and Technology,* vol. 61, no. 9, pp. 1189-1224, 2001.

[81] M. Figueiredo, A. Fernando, G. Martins, J. Freitas, F. Judas and H. Figueiredo, “Effect of the calcination temperature on the composition and microstructure of hydroxyapatite derived from human and animal bone,” *Ceramics International,* vol. 36, no. 8, pp. 2383-2393, 2010.

[82] M. Krzesińska and J. Majewska, “Physical properties of continuous matrix of porous natural hydroxyapatite related to the pyrolysis temperature of animal bones precursors,” *Journal of Analystical and Applied Pyrolysis,* vol. 116, pp. 202-214, 2015.

[83] Anonymous, “Apatite-(CaOH) Mineral Data,” [Online]. Available: http://webmineral.com/data/Apatite-(CaOH).shtml#.WPfgvfnyjtQ. [Accessed 20 April 2017].

[84] J. C. Knowles, S. Callcut and G. Georgiou, “Characterisation of the rheological properties and zeta potential of a range of hydroxyapatite powders,” *Biomaterials,* vol. 21, no. 13, pp. 1387-1392, 2000.

[85] C. Beer, R. Foldbjerg, Y. Hayashi, D. S. Sutherland and H. Autrup, “Toxicity of silver nanoparticles—Nanoparticle or silver ion?,” *Toxicology Letters,* vol. 208, no. 3, pp. 286-292, 2012.

[86] M. Alexandre and P. Dubois, “Polymer-layered silicate nanocomposites: preparation, properties and uses of a new class of materials,” *Materials Science and Engineering: R: Reports,* vol. 28, no. 1-2, pp. 1-63, 2000.

[87] A. Peigney, C. Laurent, E. Flahaut, R. R. Bacsa and A. Rousset, “Specific surface area of carbon nanotubes and bundles of carbon nanotubes,” *Carbon,* vol. 39, no. 4, pp. 507-514, 2001.

[88] R. Landsiedel, L. Ma-Hock, A. Kroll, D. Hahn, J. Schnekenburger, K. Wiench and W. Wohlleben, “Testing Metal-Oxide Nanomaterials for Human Safety,” *Advanced Materials,* vol. 22, no. 24, pp. 2601-2627, 2010.

[89] A. D. Maynard, D. B. Warheit and M. A. Philbert, “The New Toxicology of Sophisticated Materials: Nanotoxicology and Beyond,” *Toxicological Sciences,* vol. 120, no. Suppliment 1, pp. S109-S129, 2011.

[90] G. Oberdörster, E. Oberdörster and J. Oberdörster, “Nanotoxicology: An Emerging Discipline Evolving from Studies of Ultrafine Particles,” *Environmental Health Perspectives,* vol. 113, no. 7, pp. 823-839, 2005.

[91] SCENIHR, “Risk Assessment of Products of Nanotechnologies,” European Comission, 2009.

[92] S. K. Swain and D. Sarkar, “A comparative study: Hydroxyapatite spherical nanopowders and elongated nanorods,” *Ceramics International,* vol. 37, no. 7, pp. 2927-2930, 2011.

[93] J. M. Coelho, J. A. Moreira, A. Almeida and F. J. Monteiro, “Synthesis and characterization of HAp nanorods from a cationic surfactant template method,” *Journal of Materials Science: Materials in Medicine,* vol. 21, no. 9, pp. 2543-2549, 2010.

[94] C. R. Kothapalli, M. T. Shaw and M. Wei, “Biodegradable HA-PLA 3-D porous scaffolds: Effect of nano-sized filler content on scaffold properties,” *Acta Biomaterialia,* vol. 1, no. 6, pp. 653-662, 2005.

[95] S.-I. Roohani-Esfahani, S. Nouri-Khorasani, Z. Lu, R. Appleyard and H. Zreiqat, “The influence hydroxyapatite nanoparticle shape and size on the properties of biphasic calcium phosphate scaffolds coated with hydroxyapatite–PCL composites,” *Biomaterials,* vol. 31, no. 21, pp. 5498-5509, 2010.

[96] X. Zhao, S. Ng, B. C. Heng, J. Guo, L. Ma, T. T. Tan and S. C. Loo, “Cytotoxicity of hydroxyapatite nanoparticles is shape and cell dependent,” *Archives of Toxicology. Archiv für Toxikologie,* vol. 87, no. 6, pp. 1037-1052, 2013.

[97] S. I. J. Wilberforce, C. E. Finlayson, S. M. Best and R. E. Cameron, “The influence of hydroxyapatite (HA) microparticles (m) and nanoparticles (n) on the thermal and dynamic mechanical properties of poly-l-lactide,” *Polymer,* vol. 52, no. 13, pp. 2883-2890, 2011.

[98] C. Albano, G. González, J. Palacios, A. Karam and M. Covis, “PLLA-HA vs. PLGA-HA characterization and comparative analysis,” *Polymer Composites,* vol. 34, no. 9, pp. 1433-1442, 2013.

[99] C. Albano, G. González, J. Palacios, A. Karam, V. C. Reina and M. Covis, “Caracterización del compuesto poli (L-Lactida)/Hidroxiapatita: Propiedades químicas, térmicas y termomecánicas,” *Revista de la Facultad de Ingeniería,* vol. 28, no. 3, 2016.

[100] G. L. Converse, W. Yue and R. K. Roeder, “Processing and tensile properties of hydroxyapatite-whisker-reinforced polyetheretherketone,” *Biomaterials,* vol. 28, no. 6, pp. 927-935, 2007.

[101] K. Rezwan, Q. Chen, B. J.J. and A. R. Boccaccini, “Biodegradable and bioactive porous polymer/inorganic composite scaffolds for bone tissue engineering,” *Biomaterials,* vol. 27, no. 18, pp. 3413-3431, 2006.

[102] C. Y. Zhang, H. Lu, Z. Zhuang, X. P. Wang and Q. Fang, “Nano-hydroxyapatite/poly(l-lactic acid) composite synthesized by a modified in situ precipitation: preparation and properties,” *Journal of Materials Science: Materials in Medicine,* vol. 21, no. 12, pp. 3077-3083, 2010.

[103] N. K. Nga, T. T. Hoai and P. H. Viet, “Biomimetic scaffolds based on hydroxyapatite nanorod/poly(d,l) lactic acid with their corresponding apatite-forming capability and biocompatibility for bone-tissue engineering,” *Colloids and Surfaces B: Biointerfaces,* vol. 128, pp. 506-514, 2015.

[104] N. Le Bolay, V. Santran, G. Dechambe, C. Combes, C. Drouet, A. Lamure and C. Rey, “Production, by co-grinding in a media mill, of porous biodegradable polylactic acid–apatite composite materials for bone tissue engineering,” *Powder Technology,* vol. 190, no. 1-2, pp. 89-94, 2009.

[105] B. Duan, M. Wang, W. Y. Zhou, W. L. Cheung, Z. Y. Li and W. W. Lu, “Three-dimensional nanocomposite scaffolds fabricated via selective laser sintering for bone tissue engineering,” *Acta Biomaterialia,* vol. 6, no. 12, pp. 4495-4505, 2010.

[106] F. Peng, X. Yu and M. Wei, “In vitro cell performance on hydroxyapatite particles/poly(l-lactic acid) nanofibrous scaffolds with an excellent particle along nanofiber orientation,” *Acta Biomaterialia,* vol. 7, no. 6, pp. 2585-2592, 2011.

[107] A. Bianco, B. M. Bozzo, C. Del Gaudio, I. Cacciotti, I. Armentano, M. Dottori, F. D'Angelo, S. Martino, A. Orlacchio and J. M. Kenny, “Poly (L-lactic acid)/calcium-deficient nanohydroxyapatite electrospun mats for bone marrow stem cell cultures,” *Journal of Bioactive and Compatible Polymers,* vol. 26, no. 3, pp. 225-241, 2011.

[108] E. Seyedjafari, M. Soleimani, N. Ghaemi and I. Shabani, “Nanohydroxyapatite-Coated Electrospun Poly(l -lactide) Nanofibers Enhance Osteogenic Differentiation of Stem Cells and Induce Ectopic Bone Formation,” *Biomacromolecules,* vol. 11, no. 11, pp. 3118-3125, 2010.

[109] E. Aydin, J. A. Planell and V. Hasirci, “Hydroxyapatite nanorod-reinforced biodegradable poly(l-lactic acid) composites for bone plate applications,” *Journal of Materials Sciencee: Materials in Medicine,* vol. 22, no. 11, pp. 2413-2427, 2011.

[110] Y. C. W. D. Zhuo Liu, “Preparation, dynamic rheological behavior, crystallization, and mechanical properties of inorganic whiskers reinforced polylactic acid/hydroxyapatite nanocomposites,” *Journal of Applied Polymer Science,* 2016.

[111] G. G. J. P. A. K. M. C. Carmen Albano, “PLLA-HA vs. PLGA-HA Characterization and Comparative Analysis,” *Polymer Composites,* p. 1433–1442, 2013.

[112] A. Bandyopadhyay, S. Bose and S. Das, “3D printing of biomaterials,” *MRS Bulletin,* vol. 40, no. 2, pp. 108-115, 2015.

[113] D. L. Bourell, J. J. Beaman, M. C. Leu and D. W. Rosen, “A brief history of additive manufacturing and the 2009 roadmap for additive manufacturing: looking back and looking ahead,” *Proceedings of RapidTech,* pp. 24-25, 2009.

[114] F. P. W. Melchels, J. Feijen and D. W. Grijpma, “A review on stereolithography and its applications in biomedical engineering,” *Biomaterials,* vol. 31, no. 24, pp. 6121-6130, 2010.

[115] I. Gibson, D. Rosen and B. Stucker, Additive Manufacturing Technologies, Springer online: Springer, 2015.

[116] N. Guo and M. C. Leu, “Additive manufacturing: technology, applications and research needs,” *Frontiers of Mechanical Engineering,* vol. 8, no. 3, pp. 215-243, 2013.

[117] J.-P. Kruth, P. Mercelis, J. V. Vaerenbergh, L. Froyen and M. Rombouts, “Binding mechanisms in selective laser sintering and selective laser melting,” *Rapid Prototyping Journal; Bradford,* vol. 11, no. 1, pp. 26-36, 2005.

[118] H. N. Chia and B. M. Wu, “Recent advances in 3D printing of biomaterials,” *Journal of Biological Engineering,* vol. 9, no. 1, 2015.

[119] T. Billiet, M. Vandenhaute, J. Schelfhout, S. Van Vlierberghe and P. Dubruel, “A review of trends and limitations in hydrogel-rapid prototyping for tissue engineering,” *Biomaterials,* vol. 33, no. 26, pp. 6020-6041, 2012.

[120] G. D. Kim and Y. T. Oh, “A benchmark study on rapid prototyping processes and machines: quantitative comparisons of mechanical properties, accuracy, roughness, speed, and material cost,” *Proceedings of the Institution of Mechanical Engineers: Journal of Engineering Manufacture, Part B; London,* vol. 222, no. B2, pp. 201-215, 2008.

[121] K. Vimal, S. Vinodh, P. Brajesh and R. Muralidharan, “Rapid prototyping process selection using multi criteria decision making considering environmental criteria and its decision support system,” *Rapid Prototyping Journal,* vol. 22, no. 2, pp. 225-250, 2016.

[122] M. S. Hossain, J. Ramos, D. Espalin, M. Perez and R. Wicker, “Improving tensile mechanical properties of FDM-manufactured specimens via modifying build parameters,” in *International Solid Freeform Fabrication Symposium: An Additive Manufacturing Conference. Austin, TX*, Austin, TX, 2013.

[123] B. Wendel, D. Rietzel, F. Kühnlein, R. Feulner, G. Hülder and E. Schmachtenberg, “Additive Processing of Polymers,” *Macromolecular Materials and Engineering,* vol. 293, no. 10, pp. 799-809, 2008.

[124] D. Roberson, C. M. Shemelya, E. MacDonald and R. Wicker, “Expanding the applicability of FDM-type technologies through materials development,” *Rapid Prototyping Journal; Bradford,* vol. 21, no. 2, pp. 137-143, 2015.

[125] R. van Noort, “The future of dental devices is digital,” *Dental Materials,* vol. 28, no. 1, pp. 3-12, 2012.

[126] “ISO/ASTM52921-13”.

[127] L. Li, Q. Sun, C. Bellehumeur and P. Gu, “Composite modeling and analysis for fabrication of FDM prototypes with locally controlled properties,” *Journal of Manufacturing Processes; Dearborn,* vol. 4, no. 2, pp. 129-141, 2002.

[128] J. W. Comb, W. R. Priedeman and P. W. Turley, “FDM technology process improvements,” in *Proceedings of Solid Freeform Fabrication Symposium*, 1994.

[129] R. Van Weeren, M. Agarwala, V. R. Jamalabad, A. Bandyophadyay, R. Vaidyanathan, N. Langrana, A. Safari, P. Whalen, S. C. Danforth and C. Ballard, “Quality of parts processed by fused deposition,” in *Proceedings of the Solid Freeform Fabrication Symposium*, 1995.

[130] J. de Ciuarana, L. Sereóa and È. Vallès, “Selecting Process Parameters in RepRap Additive Manufacturing System for PLA Scaffolds Manufacture,” *Procedia CIRP,* vol. 5, pp. 152-157, 2013.

[131] “ASTM F2921-1”.

[132] C. Bellehumeur, L. Li, Q. Sun and P. Gu, “Modeling of bond formation between polymer filaments in the fused deposition modeling process,” *Journal of Manufacturing Processes,* vol. 6, no. 2, pp. 170-178, 2004.

[133] M. L. Shofner, K. Lozano, F. J. Rodríguez-Macías and E. V. Barrera, “Nanofiber-reinforced polymers prepared by fused deposition modeling,” *Journal of Applied Polymer Science,* vol. 89, no. 11, pp. 3081-3090, 2003.

[134] M. H. Too, K. F. Leong, C. K. Chua, Z. H. Du, S. F. Yang, C. M. Cheah and S. L. Ho, “Investigation of 3D Non-Random Porous Structures by Fused Deposition Modelling,” *The International Journal of Advanced Manufacturing Technologies,* vol. 19, no. 3, pp. 217-223, 2002.

[135] E. Ebel and T. Sinnemann, “Fabrication of FDM 3D objects with ABS and PLA and determination of their mechanical properties,” *RTejournal,* vol. 2014, no. 1, 2014.

[136] T. A. Campbell and O. S. Ivanova, “3D printing of multifunctional nanocomposites,” *Nano Today,* vol. 8, no. 2, pp. 119-120, 2013.

[137] A. Haq and R. Haq, “Characterization and development of polycaprolactone (PCL)/montmorillonite (MMT)/hydroxapaptite (HA) nanocomposites for fused deposition modelling (FDM) process,” Universiti Tun Hussein Onn Malaysia, 2015.

[138] Z. Weng, J. Wang, T. Senthil and L. Wu, “Mechanical and thermal properties of ABS/montmorillonite nanocomposites for fused deposition modeling 3D printing,” *Materials & Design,* vol. 102, pp. 276-283, 2016.

[139] D. Zhang, B. Chi, B. Li, Z. Gao, Y. Du, J. Guo and J. Wei, “Fabrication of highly conductive graphene flexible circuits by 3D printing,” *Synthetic Metals,* vol. 217, pp. 79-86, 2016.

[140] H. L. Tekinalp, V. Kunc, G. M. Velez-Garcia, C. E. Duty, L. J. Love, A. K. Naskar, C. A. Blue and S. Ozcan, “Highly oriented carbon fiber–polymer composites via additive manufacturing,” *Composites Science and Technology,* vol. 150, pp. 144-150, 2014.

[141] S. Kumar and J.-P. Kruth, “Composites by rapid prototyping technology,” *Materials & Design,* vol. 31, no. 2, pp. 850-856, 2010.

[142] M. M. Stevens, “Biomaterials for bone tissue engineering,” *Materials Today,* vol. 11, no. 5, pp. 18-25, 2008.

[143] S. Bose, M. Roy and A. Bandyopadhyay, “Recent advances in bone tissue engineering scaffolds,” *Trends in Biotechnology; Oxford,* vol. 30, no. 10, pp. 546-554, 2012.

[144] B. Stevens, Y. Yang, A. Mohandas, B. Stucker and K. T. Nguyen, “A review of materials, fabrication methods, and strategies used to enhance bone regeneration in engineered bone tissues,” *Journal of Biomedical Materials Research Part B: Applied Biomaterials,* vol. 85B, no. 2, pp. 573-582, 2008.

[145] A. A. Shendre, “Alloplastic Bone Grafting Materials,” *Indian Journal of Multidisciplinary Dentistry; Chennai,* vol. 2, no. 4, pp. 573-576, 2012.

[146] K. Leong, C. Cheah and C. Chua, “Solid freeform fabrication of three-dimensional scaffolds for engineering replacement tissues and organs,” *Biomaterials,* vol. 24, no. 13, pp. 2363-2378, 2003.

[147] D. Puppi, F. Chiellini, A. Piras and E. Chiellini, “Polymeric materials for bone and cartilage repair,” *Progress in Polymer Science,* vol. 35, no. 4, pp. 403-440, 2010.

[148] F. Cruz, Fabrication of HA/PLLA Composite Scaffolds for Bone Tissue Engineering Using Additive Manufacturing Technologies, INTECH, 2010.

[149] P. J. Bártolo, M. Domingos, T. Patrício, S. Cometa and V. Mironov, “Biofabrication Strategies for Tissue Engineering,” in *Advances on Modelling in Tissue Engineering*, Dordrecht, Springer Netherlands, 2011, pp. 137-176.

[150] L. S. Nair and C. T. Laurencin, “Biodegradable polymers as biomaterials,” *Progress in Polymer Science,* vol. 32, no. 8-9, pp. 762-798, 2007.

[151] S. Pertricca, K. Mara and P. Kumta, “Chemical synthesis of poly(lactic-co-glycolic acid)/hydroxyapatite composites for orthopaedic applications,” *Acta Biomaterialia,* vol. 2, no. 3, pp. 277-286, 2006.

[152] S.-S. Kim, M. Sun Park, O. Jeon, C. Yong Choi and B.-S. Kim, “Poly(lactide-co-glycolide)/hydroxyapatite composite scaffolds for bone tissue engineering,” *Biomaterials,* vol. 27, no. 8, pp. 1399-1409, 2006.

[153] N. Aboudzadeh, M. Imani, M. A. Shokrgozar, A. Khavandi, J. Javadpour, Y. Shafieyan and M. Farokhi, “Fabrication and characterization of poly(D,L-lactide-co-glycolide)/hydroxyapatite nanocomposite scaffolds for bone tissue regeneration,” *Journal of Biomedical Materials Research Part A,* vol. 94A, no. 1, pp. 137-145, 2010.

[154] L. K. Massey, Permeability Properties of Plastics and Elastomers, 2nd Ed., Elsevier Science, 2003.

[155] S. Zeman and L. Kubík, “Permeability of Polymeric Packaging Materials,” *Technical Sciences,* vol. 10, no. 1, pp. 33-34, 2007.

[156] M. R. Kamal, I. A. Jinnah and L. Utracki, “Permeability of oxygen and water vapor through polyethylene/polyamide films,” *Polymer Engineering & Science,* vol. 24, no. 17, pp. 1337-1347, 1984.

[157] H. L. Frisch, ““Diffusion in polymers” edited by J. Crank and G. S. Park, Academic Press, London and New York, 1968; 452 pg,” *Journal of Applied Polymer Science,* vol. 14, no. 6, pp. 1657-1657, 1970.

[158] A. Fick, “On liquid diffusion,” *Journal of Membrane Science,* vol. 100, no. 1, pp. 33-38, 1995.

[159] M. D. Sanchez-Garcia, E. Gimenez and J. M. Lagaron, “Morphology and barrier properties of nanobiocomposites of poly(3-hydroxybutyrate) and layered silicates,” *Journal of Applied Polymer Science,* vol. 108, no. 5, pp. 2787-2801, 2008.

[160] M. D. Sanchez-Garcia, A. Lopez-Rubio and J. M. Legaron, “Natural micro and nanobiocomposites with enhanced barrier properties and novel functionalities for food biopackaging applications,” *Trends in Food Science & Technology,* vol. 21, no. 11, pp. 528-536, 2010.

[161] R. Shogren, “Water vapor permeability of biodegradable polymers,” *Journal of Environmental Polymer Degradation; Dordrecht,* vol. 5, no. 2, pp. 91-95, 1997.

[162] L. H. Poley, M. G. d. Silva, H. Vargas, M. O. Siquera and R. Sánchez, “Water and vapor permeability at different temperatures of poly (3-Hydroxybutyrate) dense membranes,” *Polímeros,* vol. 15, no. 1, pp. 22-26, 2005.

[163] H. Tsuji, R. Okino, H. Daimon and K. Fujie, “Water vapor permeability of poly(lactide)s: Effects of molecular characteristics and crystallinity,” *Journal of Applied Polymer Science,* vol. 99, no. 5, pp. 2245-2252, 2006.

[164] Z. Song, H. Xiao and Y. Zhao, “Hydrophobic-modified nano-cellulose fiber/PLA biodegradable composites for lowering water vapor transmission rate (WVTR) of paper,” *Carbohydrate Polymers,* vol. 111, pp. 442-448, 2014.

[165] T. Dong, Z. Yu, J. Wu, Z. Zhao, X. Yun, Y. Wang, Y. Jin and J. Yang, “Thermal and barrier properties of stretched and annealed polylactide films,” *Polymer Science Series A,* vol. 57, no. 6, pp. 738-746, 2015.

[166] V. Ducruet, S. Domenek, A. Guinault, C. Courgneau, M. Bernasconi and C. Plessis, “Barrier Properties of Pla Towards Oxygen and Aroma Compounds,” *Italian Journal of Food Science: IJFS; Pinerolo,* vol. 23, pp. 59-62, 2011.

[167] G. Colomines, S. Domenek, V. Ducruet and A. Guinault, “Influences of the crystallisation rate on thermal and barrier properties of polylactide acid (PLA) food packaging films,” *International Journal of Material Forming,* vol. 1, no. 1, pp. 607-610, 2008.

[168] S. R. Chowdhury, “Some important aspects in designing high molecular weight poly(L-lactic acid)–clay nanocomposites with desired properties,” *Polymer International,* vol. 57, no. 12, pp. 1326-1332, 2008.

[169] G. Gorrasi, R. Pantani, M. Murariu and P. Dubois, “PLA/Halloysite Nanocomposite Films: Water Vapor Barrier Properties and Specific Key Characteristics,” *Macromolecular Materials and Engineering,* vol. 299, no. 1, pp. 104-115, 2014.

[170] R. Pantani, G. Gorrasi, G. Vigliotta, M. Murariu and P. Dubois, “PLA-ZnO nanocomposite films: Water vapor barrier properties and specific end-use characteristics,” *European Polymer Journal,* vol. 49, no. 11, pp. 3471-3482, 2013.

[171] M. Żenkiewicz and J. Richert, “Permeability of polylactide nanocomposite films for water vapour, oxygen and carbon dioxide,” *Polymer Testing,* vol. 27, no. 7, pp. 835-840, 2008.

[172] A. Abdellatief and B. A. Welt, “Comparison of New Dynamic Accumulation Method for Measuring Oxygen Transmission Rate of Packaging against the Steady-State Method Described by ASTM D3985,” *Packaging Technology and Science,* vol. 26, no. 5, pp. 281-288, 2013.

[173] I. Siró, D. Plackett and P. Sommer-Larsen, “A comparative study of oxygen transmission rates through polymer films based on fluorescence quenching,” *Packaging Technology and Science,* vol. 23, no. 6, pp. 301-315, 2010.

[174] Anonymous, “Water Vapor Permeability Tester, Water Vapor Transmission Rate (WVTR) Tester - Labthink,” Labthink, [Online]. Available: http://en.labthink.com/en-us/products/test-property/water-vapor-permeability-tester.html?gclid=Cj0KEQjww7zHBRCToPSj_c_WjZIBEiQAj8il5CdMiNxB1TacpZlij_YiYpbXJGXlvBPz_ZMj8y6HQioaAuoe8P8HAQ. [Accessed 14 April 2017].

[175] “ISO/FDIS 2528”.

[176] “ASTM E96/E96M-16”.

[177] “ASTM D1653-13”.

[178] “ISO 15106-3:2003”.

[179] “ISO 15106-2:2003”.

[180] “ASTM F1249-13”.

[181] “TAPPI T557”.

[182] “ISO 15106-1:2003”.

[183] “ASTM E398-13”.

[184] “TAPPI T523”.

[185] “ASTM D3985- 05(2010)e1”.

[186] “ASTM F1307-14”.

[187] “ASTM F2622-8”.

[188] “ASTM F1927-14”.

[189] M. Öner and B. İlhan, “Fabrication of poly(3-hydroxybutyrate-co-3-hydroxyvalerate) biocomposites with reinforcement by hydroxyapatite using extrusion processing,” *Materials Science and Engineering: C,* vol. 65, pp. 19-26, 2016.

[190] K. Y. Yasuda, R. C. Armstrong and R. E. Cohen, “Shear flow properties of concentrated solutions of linear and star branched polystyrenes,” *Rheologica Acta,* vol. 20, no. 2, pp. 163-178, 1981.

[191] “NF EN 13432:2000”.

[192] “ISO 527-2”.

[193] D. H. Doehlert, “Uniform Shell Designs,” *Applied Statistics,* vol. 19, no. 3, pp. 231-239, 1970.

[194] J. Goupy and L. Creighton, Introduction aux plans d'expériences, Paris: Dunod, 2006.

[195] A. C. Fowlks and R. Narayan, “The effect of maleated polylactic acid (PLA) as an interfacial modifier in PLA-talc composites,” *Journal of Applied Polymer Science,* vol. 118, no. 5, pp. 2810-2820, 2010.

[196] T. Gerard and T. Budtova., “Morphology and Molten-State Rheology of Polylactide and Polyhydroxyalkanoate Blends,” *European Polymer Journal,* vol. 48, p. 1110–1117, 2012.

[197] W. P. Cox and E. H. Merz, “Correlation of Dynamic and Steady Flow Viscosities,” *Journal of Polymer Science,* vol. XXVIII, no. 118, p. n/a, 1958.

[198] P. E. Le Marec, J.-C. Quantin, L. Ferry, J.-C. Bénézet, S. Guilbert and A. Bergeret, “Modelling of PLA Melt Rheology and Batch Mixing Energy Balance,” *European Polymer Journal,* vol. 60, pp. 273-285, 2014.

[199] H. Borchert, E. V. Shevchenko, A. Robert, I. Mekis, A. Kornowski, G. Grübel and H. Weller, "Determination of Nanocrystal Sizes: A Comparison of TEM, SAXS, and XRD Studies of Highly Monodisperse CoPt ₃ Particles," *Langmuir,* vol. 21, no. 5, pp. 1931-1936, 2005.

[200] A. Doublier, D. Farlay, X. Jaurand, R. Vera and G. Boivin, "Effects of strontium on the quality of bone apatite crystals: a paired biopsy study in postmenopausal osteoporotic women," *Osteoporosis International,* vol. 24, no. 3, pp. 1079-1087, 2013.

[201] L. Feng, G. Li, X. Bian, Z. Chen, Y. Liu, Y. Cui and X. Chen, "Rapid determination of residual monomer in polylactide using thermogravimetric analysis," *Polymer Testing,* vol. 31, no. 5, pp. 660-662, 2012.

[202] X. Cao, A. Mohamed, S. H. Gordon, J. Willett and D. J. Sessa, "DSC study of biodegradable poly(lactic acid) and poly(hydroxy ester ether) blends," *Thermochimica Acta,* vol. 406, no. 1-2, pp. 115-127, 2003.

[203] J. Zhang, K. Tashiro, H. Tsuji and A. J. Domb, "Disorder-to-order phase transition and multiple melting behavior of poly (L-lactide) investigated by simultaneous measurements of WAXD and DSC," *Macromolecules,* vol. 41, no. 4, pp. 1352-1357, 2008.

[204] I. Pillin, N. Montrelay, A. Bourmaud and Y. Grohens, "Effect of thermo-mechanical cycles on the physico-chemical properties of poly(lactic acid)," *Polymer Degradation and Stability,* vol. 93, no. 2, pp. 321-328, 2008.

[205] M. Pavlovic, Bioengineering: A Conceptual Approach, Springer, 2014.

[206] A. Jabbar, J. Militký, J. Wiener and M. Karahan, "Static and dynamic mechanical properties of novel treated jute/green epoxy composites," *Textile Research Journal,* vol. 86, no. 9, pp. 960-974, 2016.

[207] D. Z. Chen, C. Y. Tang, K. C. Chan, C. P. Tsui, P. H. F. Yu, M. C. P. Leung and P. S. Uskovic, "Dynamic mechanical properties and in vitro bioactivity of PHBHV/HA nanocomposite," *Composites Science and Technology,* vol. 67, no. 7-8, pp. 1617-1626, 2007.

[208] A. K. Mohapatra, S. Mohanty and S. K. Nayak, "Poly(lactic acid) and layered silicate nanocomposites prepared by melt mixing: Thermomechanical and morphological properties," *Polymer Composites,* vol. 33, no. 12, pp. 2095-2104, 2012.

[209] A. K. Mohapatra, S. Mohanty and S. K. Nayak, "Study of Thermo-Mechanical and Morphological Behaviour of Biodegradable PLA/PBAT/Layered Silicate Blend Nanocomposites," *Journal of Polymers and the Environment,* vol. 22, no. 3, pp. 398-408, 2014.

[210] M. F. S. Khalid and A. H. Abdullah, "Storage Modulus Capacity of Untreated Aged Arenga pinnata Fibre-Reinforced Epoxy Composite," *Applied Mechanics and Materials; Zurich,* vol. 393, p. 171, 2013.

[211] J. Adam, B. A. Korneliusz and M. Agnieszka, "Dynamic mechanical thermal analysis of biocomposites based on PLA and PHBV—A comparative study to PP counterparts," *Journal of Applied Polymer Science,* vol. 130, no. 5, pp. 3175-3183, 2013.

[212] R. M. Taib, Z. A. Ghaleb and Z. A. Mohd Ishak, “Thermal, mechanical, and morphological properties of polylactic acid toughened with an impact modifier,” *Journal of Applied Polymer Science,* vol. 123, no. 5, pp. 2715-2725, 2012.

[213] M. Pluta, J. K. Jezka and G. Boiteux, “Polylactide/montmorillonite nanocomposites: Structure, dielectric, viscoelastic and thermal properties,” *European Polymer Journal,* vol. 43, no. 7, pp. 2819-2835, 2007.

[214] M. Pluta, “Morphology and properties of polylactide modified by thermal treatment, filling with layered silicates and plasticization,” *Polymer,* vol. 45, no. 24, pp. 8239-8251, 2004.

[215] M. Pluta, M. Murariu, M. Alexandre, A. Galeski and P. Duboi, “Polylactide compositions. The influence of ageing on the structure, thermal and viscoelastic properties of PLA/calcium sulfate composites,” *Polymer Degradation and Stability,* vol. 93, no. 5, pp. 925-931, 2008.

[216] M. Pluta, M. Murariu, A. Da Silva Ferreira, M. Alexandre, A. Galeski and P. Dubois, “Polylactide compositions. II. Correlation between morphology and main properties of PLA/calcium sulfate composites,” *Journal of Polymer Science Part B: Polymer Physics,* vol. 45, no. 19, pp. 2770-2780, 2007.

[217] M. Pluta and A. Galeski, “Crystalline and supermolecular structure of polylactide in relation to the crystallization method,” *Journal of Applied Polymer Science,* vol. 86, no. 6, pp. 1386-1395, 2002.

[218] M. Huda, L. Drzal, A. Mohanty and M. Misra, “Chopped glass and recycled newspaper as reinforcement fibers in injection molded poly(lactic acid) (PLA) composites: A comparative study,” *Composites Science and Technology,* vol. 66, no. 11-12, pp. 1813-1824, 2006.

[219] S. K. Saw, G. Sarkhel and A. Choudhury, “Dynamic mechanical analysis of randomly oriented short bagasse/coir hybrid fibre-reinforced epoxy novolac composites,” *Fibers and Polymers,* vol. 12, no. 4, p. 506, 2011.

[220] A. K. Rana, B. C. Mitra and A. N. Banerjee, “Short jute fiber-reinforced polypropylene composites: Dynamic mechanical study,” *Journal of Applied Polymer Science,* vol. 71, no. 4, p. 531, 1999.

[221] T. L. Nguyen, F. Bédoui, P.-E. Mazeran and M. Guigon, “Mechanical investigation of confined amorphous phase in semicrystalline polymers: Case of PET and PLA,” *Polymer Engineering & Science,* vol. 55, no. 2, pp. 397-405, 2015.

[222] L. Famá, P. G. Rojo, C. Berbak and S. Goyanes, “Biodegradable starch based nanocomposites with low water vapor permeability and high storage modulus,” *Carbohydrate Polymers,* vol. 87, no. 3, pp. 1989-1993, 2012.

[223] W. Zhang, D. Chen, Q. Zhao and Y. Fang, “Effects of different kinds of clay and different vinyl acetate content on the morphology and properties of EVA/clay nanocomposites,” *Polymer,* vol. 44, no. 26, pp. 7953-7961, 2003.

[224] E. C. Vouvoudi and I. D. Sideridou, “Dynamic mechanical properties of dental nanofilled light-cured resin composites: Effect of food-simulating liquids,” *Journal of the Mechanical Behavior of Biomedical Materials,* vol. 10, pp. 87-96, 2012.

[225] Gabriel, “Product - HAp Pastes,” The nano-hydroxyapatite specialist | FLUIDINOVA, [Online]. Available: http://www.fluidinova.com/nano-hydroxyapatite-pastes-for-injectable-bone-substitute-biomaterial. [Accessed 2 June 2017].

[226] Anonymous, “NATUREPLAST - Presentation,” Natureplast, [Online]. Available: http://www.natureplast.eu/en/. [Accessed 2 June 2017].

Annexes

Annexe A Technical Data Sheet Hydroxyapatite paste [225].

Technical Data Sheet

PRODUCT INFORMATION

nanoXIM•HAp100 is a series of synthetic nano-hydroxyapatite aqueous pastes, manufactured and supplied in 2 different concentrations by FLUIDINOVA S.A.

General specifications

Phase purity, $Ca_{10}(PO_4)_6(OH)_2$, % (1)	100
Specific surface area BET, m^2/g	≥ 80
Heavy metals, as Pb, ppm	≤ 20

Product specifications

	Hydroxyapatite content, % wt
nanoXIM•HAp102	15.0 ± 1.0
nanoXIM•HAp103	30.0 ± 3.0

Product properties

	Specific gravity, g/cm^3	Physical appearance
nanoXIM•HAp102	1.1 ± 0.1	white paste
nanoXIM•HAp103	1.2 ± 0.1	white paste (mouldable paste)

(1) A minimum of 95% hydroxyapatite phase purity is assured when the material is sintered for 15h at 1000ºC, in accordance with ISO13779.

nanoXIM HAp100

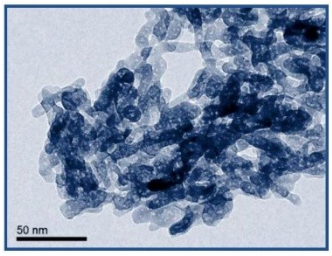

Figure 1. TEM image - General overview.

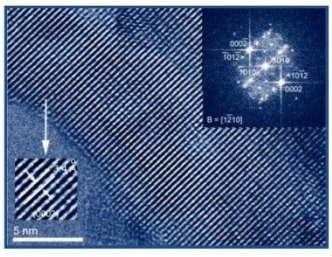

Figure 2. TEM image - Crystal orientation.

GENERAL INFORMATION

nanoXIM•HAp100 are synthetic nano-hydroxyapatite water based pastes suitable for the manufacture of bone grafts such as injectable bone substitutes.

Due to their high surface area and similarity with the bone mineral, nanoXIM•HAp100 pastes are highly osteostimulative, promoting the adhesion of bone cells and fast formation of new bone. The medical devices manufactured with nanoXIM•HAp100 pastes allow fast and safe bone regeneration and are highly biocompatible. No adverse reactions have ever been reported by the use of these materials.

Package

Available in PE food grade containers at different sizes.

Storage, Safety & Handling

To ensure the quality of the product, keep it in a closed container at room temperature in a clean and dry place. Do not freeze.

For more details about product safety and handling information, please refer to the FLUIDINOVA Safety Data Sheet (SDS).

Mod.108.0

FLUIDINOVA

FLUIDINOVA, S.A.
Tecmaia - Rua Engº Frederico Ulrich, nº 2650 | 4470-605 Moreira da Maia | Portugal
www.fluidinova.com | nanoxim@fluidinova.com | T: +351 220 119 746 | F: +351 220 119 748

Annexe B Technical Data Sheet PLE 005 (1) [226].

NaturePlast
L'évolution naturelle du plastique

Date de révision : 19/03/2015

FICHE TECHNIQUE — NATUREPLAST PLE 005

Poly (Acide Lactique) — Extrusion / Calandrage / Thermoformage

Propriétés générales

La référence **PLE 005** est une résine thermoplastique de **PLA** (Polylactide) issue de ressources végétales annuellement renouvelables certifiées d'origine non génétiquement modifiées.

Le **PLE 005** est **recyclable**, **compostable** industriellement selon la norme **NF EN 13432:2000** et spécifiquement élaboré pour les applications d'extrusion (film, thermoformage, etc.).

	Méthode	Unité	Valeur*
Propriétés Générales			
Densité	ISO 1183	/	**1,26**
MFI (190°C ; 2,16 kg)	ISO 1133	g/10min	**5 – 9**
Dureté (15s)	ISO 868	Shore D	**80**
Propriétés optiques	/	/	**Transparent**
Propriétés Thermiques			
Température de fusion	/	°C	**170 - 180**
HDT Méthode B120	ISO 75-2	°C	**57,3**
Vicat Méthode A50	ISO 306	°C	**60,7**
Propriétés Mécaniques			
Contrainte de traction au seuil élastique	ISO 527	MPa	**20**
Allongement en traction au seuil élastique	ISO 527	%	**1,1**
Contrainte de traction maximale	ISO 527	MPa	**71,2**
Allongement en traction à contrainte maximale	ISO 527	%	**4,5**
Contrainte de traction à rupture	ISO 527	MPa	**62,3**
Allongement en traction à rupture	ISO 527	%	**6,6**
Module d'Young	ISO 527	MPa	**3820**
Module en flexion	ISO 178	MPa	**3310**
Choc Charpy (non entaillé)	ISO 179	kJ/m²	**19,6**

**Valeurs typiques données à titre indicatif ne devant pas être considérées comme des spécifications*

NaturePlast
11 rue Arago ; 14123 IFS ; France / Tel : (+33)2 31 83 50 87 / Fax : (+33)2 31 84 70 98 / www.natureplast.eu
SAS au capital de 174 666 € APE : 4690Z / SIRET : 493 442 891 00047 / TVA : FR 45 49 344 2891

NaturePlast
L'évolution naturelle du plastique

Date de révision : 19/03/2015

Stockage et Transformation

Les conditions de séchage et de stockage du **PLE 005**, afin d'obtenir une transformation et des propriétés optimales (i.e. taux d'humidité inférieur à 250 ppm) sont les suivantes :

Séchage des granules :

- Trois (3) heures à 60°C en étuve ou dessiccateur.

Stockage des granules :

- Stockage à l'abri de l'air et de la lumière directe ainsi que de toute source de chaleur.
- Garder l'emballage scellé jusqu'à ce qu'il soit prêt à l'emploi et le refermer rapidement s'il n'est pas utilisé entièrement pour éviter toute contamination ou reprise d'humidité.

Recommandations lors de la transformation :

- Le **PLE 005** est incompatible avec une grande variété de résines : une purge prolongée peut donc être nécessaire afin d'éviter toute pollution.
- Une bonne régulation de la première zone de chauffe (alimentation) **inférieure à 30°C** est indispensable afin d'éviter la création d'un phénomène de bouchage pouvant entraîner des problèmes de stabilité du cycle de production.
- Eviter une stagnation trop longue de la matière dans le fourreau afin d'éviter une dégradation thermique pouvant entrainer une diminution des propriétés et des instabilités de production.

Profil de température de mise en œuvre ***(à titre indicatif)***	
Zone d'alimentation	**25°C**
Zone 2	**160°C**
Zone 3	**170°C**
Zone 4	**175°C**
Zone 5	**175°C**
Filière	**180°C**
Vitesse de vis	**100 rpm**

NaturePlast
11 rue Arago ; 14123 IFS ; France / Tel : (+33)2 31 83 50 87 / Fax : (+33)2 31 84 70 98 / www.natureplast.eu
SAS au capital de 174 666 € APE : 4690Z / SIRET : 493 442 891 00047 / TVA : FR 45 49 344 2891

Auteursrechtelijke overeenkomst

Ik/wij verlenen het wereldwijde auteursrecht voor de ingediende eindverhandeling:
Optimisation and characterisation of nano-hydroxyapatite/polylactide composites using Fused Deposition Modelling technology

Richting: **master in de industriële wetenschappen: verpakkingstechnologie**
Jaar: **2017**

in alle mogelijke mediaformaten, - bestaande en in de toekomst te ontwikkelen - , aan de Universiteit Hasselt.

Niet tegenstaand deze toekenning van het auteursrecht aan de Universiteit Hasselt behoud ik als auteur het recht om de eindverhandeling, - in zijn geheel of gedeeltelijk -, vrij te reproduceren, (her)publiceren of distribueren zonder de toelating te moeten verkrijgen van de Universiteit Hasselt.

Ik bevestig dat de eindverhandeling mijn origineel werk is, en dat ik het recht heb om de rechten te verlenen die in deze overeenkomst worden beschreven. Ik verklaar tevens dat de eindverhandeling, naar mijn weten, het auteursrecht van anderen niet overtreedt.

Ik verklaar tevens dat ik voor het materiaal in de eindverhandeling dat beschermd wordt door het auteursrecht, de nodige toelatingen heb verkregen zodat ik deze ook aan de Universiteit Hasselt kan overdragen en dat dit duidelijk in de tekst en inhoud van de eindverhandeling werd genotificeerd.

Universiteit Hasselt zal mij als auteur(s) van de eindverhandeling identificeren en zal geen wijzigingen aanbrengen aan de eindverhandeling, uitgezonderd deze toegelaten door deze overeenkomst.

Voor akkoord,

Oris, Erwin

Datum: **6/06/2017**